

On the Flows Developed Within the Gap of Two Parallel Discs

Panagiota Tsifourdaris

A Thesis

In

The Department

Of

Mechanical and Industrial Engineering

Presented in Partial Fulfillment of the Requirements

For the Degree of Doctor of Philosophy at

Concordia University

Montreal, Quebec, Canada

April 2003

© Panagiota Tsifourdaris, 2003



**National Library
of Canada**

**Acquisitions and
Bibliographic Services**

**395 Wellington Street
Ottawa ON K1A 0N4
Canada**

**Bibliothèque nationale
du Canada**

**Acquisitions et
services bibliographiques**

**395, rue Wellington
Ottawa ON K1A 0N4
Canada**

Your file Votre référence

Our file Notre référence

The author has granted a non-exclusive licence allowing the National Library of Canada to reproduce, loan, distribute or sell copies of this thesis in microform, paper or electronic formats.

L'auteur a accordé une licence non exclusive permettant à la Bibliothèque nationale du Canada de reproduire, prêter, distribuer ou vendre des copies de cette thèse sous la forme de microfiche/film, de reproduction sur papier ou sur format électronique.

The author retains ownership of the copyright in this thesis. Neither the thesis nor substantial extracts from it may be printed or otherwise reproduced without the author's permission.

L'auteur conserve la propriété du droit d'auteur qui protège cette thèse. Ni la thèse ni des extraits substantiels de celle-ci ne doivent être imprimés ou autrement reproduits sans son autorisation.

0-612-77909-2

Canada

ABSTRACT

On the Flows Developed Within the Gap of Two Parallel Discs

Panagiota Tsifourdaris, Ph.D

Concordia University, 2003

Flow development within disc-like domains, is of significant practical importance since it is often found in a number of technological applications, such as radial diffusers, centrifugal compressors, air bearings, and VTOL aircrafts with centrally located pointing jets. The radial flow between two stationary closely spaced discs can be classified into inflow and outflow.

The inflow, or accelerating, or sink flow, is realized when fluid enters the space between two flat discs via the periphery and drains through a centrally located outlet. The flow that is characterized by a monotonically decreasing pressure gradient is known to remain laminar even at very high Reynolds numbers, or to laminarize if the entering fluid is initially turbulent. The outflow, or decelerating, or source flow, is the type of flow where the fluid is admitted through a centrally located inlet and discharged through the periphery. As a result of the area increase, the velocity decreases, and an adverse pressure gradient develops.

Analytical and experimental analyses were performed for the inflow and outflow between two discs both with and without swirl. In the analytical study (with and without swirl), it was shown that the radial velocity is expressed only as a function of the radial location and Reynolds number, whereas the static pressure for the swirling flows depends on the Reynolds number, radial position and swirl strength. The analytical model was

also validated with present and previously obtained experimental findings and showed good agreement.

An experimental investigation was also carried out to explore the flow between two narrowly spaced discs over the range of low and moderate Reynolds numbers. Radial velocity and static pressure measurements were obtained for the non-swirling inflow and outflow, whereas for the swirling cases only static pressures were acquired. The experimental results were then compared with the present theory and showed good agreement. For the inflow case, the results displayed the characteristics of the accelerating flow, whereas for the outflow case without swirl, the *vena contracta* effects, as well as the phenomenon of the reverse flow at the inlet region were demonstrated.

ACKNOWLEDGEMENTS

The author would like to express her greatest gratitude and appreciation to her supervisors Dr. Georgios Vatistas and Dr. Wahid Ghaly, for their continuous encouragement and support. Extended thanks to Dr. Ghaly for his helpful suggestions and advice, and for always prompting me to think further.

I would like to thank Dr. Vatistas, my mentor, for broadening my vision and always encouraging me to do better. Most importantly, he always exposed me to new ideas, views and concepts that go beyond the present thesis. He not only prepared me to enter the professional engineering community, but also gave me valuable lessons to become a better person and a valuable member of our society. It was a real challenge working with him, and I consider myself very lucky to have been under his supervision. I thank him from the bottom of my heart for all the encouragement he and his family offered me during my studies.

The author would like to thank the technicians, Brian Cooper and Juan Alfara, for their assistance with the construction and setting up of the experimental apparatus. I also offer my extensive thanks to John Elliott for always responding when I needed assistance.

I would like to express my deepest indebtedness to my incredible parents, Vaso and Vageli Tsifourdaris, and my dear sister Anastasia, who stood by my side all these years. They always kept on encouraging me, offering me their moral support and love all the way from Greece. I also want to thank my godmother, Angeliki Bartzakos, for the support she gave me during my studies.

I would like to thank my very dearest friends, Vicky Karahontziti and Eleni Vassiliou, for the unconditional friendship and encouragement they gave me and continue to give me. I cannot imagine having better friends.

Last, but certainly not least, I would especially like to thank Beryl Bedard for always being by my side. He offered me strength, encouragement and assistance when I really needed it. I offer him my deepest gratitude for his valuable suggestions for improving my work. Without him, I wouldn't have been able to complete my thesis on time. Thank you!

This thesis is dedicated to my parents Vaso and Vageli Tsifourdaris, and to my professor

Dr. Georgios Vatistas.

Panagiota Tsifourdaris

TABLE OF CONTENTS

LIST OF FIGURES	IX
NOMENCLATURE	XII
CHAPTER I	1
INTRODUCTION.....	1
1.1 THE PROBLEM.....	1
1.2 LITERATURE SURVEY.....	2
<i>1.2.1 Inflow</i>	<i>3</i>
<i>1.2.2 Outflow.....</i>	<i>11</i>
1.3 THE CONTRIBUTION	21
CHAPTER II.....	23
THE EXPERIMENTAL APPARATUS AND PROCEDURE	23
2.1 EXPERIMENTAL PLANNING AND PROCEDURE.....	24
2.2 INSTRUMENTATION AND APPARATUS	26
<i>2.2.1 Experimental set-up</i>	<i>26</i>
<i>2.2.2 Plexiglas Discs.....</i>	<i>28</i>
<i>2.2.3 Spacers.....</i>	<i>30</i>
<i>2.2.4 Vortex rings.....</i>	<i>30</i>
<i>2.2.5 Flow Measurement.....</i>	<i>32</i>
<i>2.2.6 Pitot – Static tube.....</i>	<i>34</i>
<i>2.2.7 Inclined Manometers</i>	<i>35</i>

2.3 CONSIDERATIONS ON EXPERIMENTAL ANALYSIS, DATA TREATMENT AND ERRORS ..	35
CHAPTER III	37
ANALYTICAL DEVELOPMENT OF THE PROBLEM	37
3.1 DIMENSIONAL ANALYSIS	37
3.2 STATEMENT OF THE THEORETICAL PROBLEM	38
3.3 FLOW WITH SWIRL	40
3.3.1 <i>Inflow and Swirl</i>	43
3.3.2 <i>Outflow and Swirl</i>	57
3.4 SOME SIMPLER FLOW CASES	68
3.4.1 <i>Inflow without swirl</i>	68
3.4.2 <i>Outflow without swirl</i>	69
CHAPTER IV	70
DISCUSSION OF THE RESULTS	70
4.1 SINK FLOW	70
4.2 SOURCE FLOW	104
CONCLUSIONS	127
FUTURE WORK	131
REFERENCES	132
APPENDIX A - DERIVATION OF THE EQUATIONS	136
APPENDIX B – TWAITES METHOD	162

LIST OF FIGURES

FIGURE 2.1 – EXPERIMENTAL APPARATUS.....	24
FIGURE 2.2 – SCHEMATIC OF THE DISCS	25
FIGURE 2.3 – SCHEMATIC OF INFLOW WITH SWIRL	27
FIGURE 2.4 SCHEMATIC OF OUTFLOW WITH SWIRL.....	28
FIGURE 2.5 – SCHEMATIC OF THE TOP DISC	29
FIGURE 2.6 – SCHEMATIC OF THE BOTTOM DISC.....	30
FIGURE 2.7 – VORTEX RING FOR OUTFLOW (SOURCE).....	31
FIGURE 2.8 – VORTEX RING FOR INFLOW (SINK).....	32
FIGURE 2.9 – SCHEMATIC OF A ROTAMETER.....	33
FIGURE 2.10 – MICROMETER ASSEMBLY	34
FIGURE 3. 1 – SCHEMATIC OF INFLOW BETWEEN TWO DISCS	39
FIGURE 3.2 – SCHEMATIC OF COORDINATE SYSTEM FOR INFLOW WITH SWIRL	43
FIGURE 3.3 – SCHEMATIC OF OUTFLOW BETWEEN TWO DISCS.....	57
FIGURE 4.1- SCHEMATIC OF FLOW ZONES	71
FIGURE 4.2 – VARIATION OF B.L DISPLACEMENT THICKNESS VERSUS RADIAL POSITION.....	72
FIGURE 4.3 – VARIATION OF EXIT ZONE III VERSUS RADIAL POSITION η_e	73
FIGURE 4.4 – RADIAL VELOCITY PROFILES FOR VARIOUS λ	76
FIGURE 4.5 – RADIAL VELOCITY PROFILES FOR VARIOUS REDUCED REYNOLDS NUMBERS	76
FIGURE 4.6 (A) – PRESENT RADIAL VELOCITY PROFILES FOR $Re=328.74$	77
FIGURE 4.6 (B) – PRESENT RADIAL VELOCITY PROFILES FOR $Re=493.12$	78
FIGURE 4.6 (C) – PRESENT RADIAL VELOCITY PROFILES FOR $Re=657.49$	79
FIGURE 4.7 (A) –RADIAL VELOCITY PROFILES OF PRESENT THEORY WITH EXPERIMENTS [8]	80

FIGURE 4.7 (B) – RADIAL VELOCITY PROFILES OF PRESENT THEORY WITH EXPERIMENTS [2]	81
FIGURE 4.8 (A) – PRESENT EXPERIMENTAL MAXIMUM RADIAL VELOCITY VERSUS λ	82
FIGURE 4.8 (B) MAXIMUM RADIAL VELOCITY OF PRESENT THEORY WITH EXPERIMENTS [2]	82
FIGURE 4.9 – APPROXIMATION OF MAXIMUM RADIAL VELOCITY	83
FIGURE 4.10 (A) – STATIC PRESSURE PROFILES FROM THEORY [6] AND EXPERIMENTS [32]	84
FIGURE 4.10 (B) – STATIC PRESSURE PROFILES FOR NON-SWIRLING INFLOW AND FOR $\xi = 0.0278$, 0.01389	86
FIGURE 4.10 (C) – STATIC PRESSURE PROFILES FOR NON-SWIRLING INFLOW AND $\xi = 0.01042$, 0.00694	87
FIGURE 4.10 (D) – STATIC PRESSURE APPROXIMATION OF PRESENT THEORY WITH [8]	88
FIGURE 4.11 (A) – RADIAL VELOCITY PROFILES OF PRESENT THEORY WITH EXPERIMENTS [2] FOR	90
$s = 0.07$	90
FIGURE 4.11 (B) – RADIAL VELOCITY PROFILES OF PRESENT THEORY WITH EXPERIMENTS [2] FOR	91
$s = 0.05$	91
FIGURE 4.12 – THEORETICAL TANGENTIAL VELOCITY PROFILES FOR TWO STATIONARY DISCS ..	92
FIGURE 4. 13 – THEORETICAL TANGENTIAL VELOCITY PROFILES FOR TWO ROTATING DISCS	93
FIGURE 4.14 - MAXIMUM TANGENTIAL VELOCITY	95
VERSUS η FOR STATIONARY DISCS	95
FIGURE 4.15 – MAXIMUM TANGENTIAL VELOCITY	95
VERSUS η FOR ROTATING DISCS	95
FIGURE 4.16 (A) - MAXIMUM TANGENTIAL VELOCITY FOR $Re_r = 197$ AND $s = 15$	96
FIGURE 4.16 (B) – MAXIMUM TANGENTIAL VELOCITY FOR $Re_r = 9.0$ AND $s = 0.07$	97
FIGURE 4.17 – TANGENTIAL VELOCITY PROFILES FROM [13]	98

FIGURE 4.18 – PRESSURE $\Delta\Pi$ VERSUS DIMENSIONLESS PARAMETER λ	99
FIGURE 4.19 (A) – STATIC PRESSURE PROFILES FOR SWIRLING INFLOW AND FOR $\xi = 0.0278$, 0.01389	101
FIGURE 4.19 (B) – STATIC PRESSURE PROFILES FOR SWIRLING INFLOW AND FOR $\xi = 0.01042$, 0.00694	102
FIGURE 4.20 –PRESENT STATIC PRESSURE PROFILES FOR SWIRLING AND NON-SWIRLING INFLOW	103
FIGURE 4.21 – SCHEMATIC OF FLOW REGIONS IN THE SOURCE FLOW.....	105
FIGURE 4.22 (A) – RADIAL VELOCITY PROFILES FOR $H = 0.25$ IN AND $Q = 20$ CFM	107
FIGURE 4.22 (B) – RADIAL VELOCITY PROFILES FOR $H = 0.5$ IN AND $Q = 20$ CFM.....	109
FIGURE 4.22 (C) – RADIAL VELOCITY PROFILES FOR $H = 0.5$ IN AND $Q = 30$ CFM.....	111
FIGURE 4.22 (D) – RADIAL VELOCITY PROFILES FOR $H = 0.5$ IN AND $Q = 50$ CFM	113
FIGURE 4.22 (E) – RADIAL VELOCITY PROFILES FOR $H = 0.5$ IN AND $Q = 60$ CFM.....	115
FIGURE 4.23 (A) – STATIC PRESSURE PROFILES FOR NON-SWIRLING OUTFLOW AND FOR $\xi = 0.1$, 0.15	117
FIGURE 4.23 (B) – – STATIC PRESSURE PROFILES FOR NON-SWIRLING OUTFLOW AND FOR $\xi = 0.2$, 0.4	118
FIGURE 4.24 TEST RESULTS FOR THE SEPARATION POINT VERSUS REYNOLDS NUMBER [28].....	120
FIGURE 4.25 (A) – STATIC PRESSURE PROFILES FOR SWIRLING OUTFLOW AND $\xi = 0.1, 0.15$	122
FIGURE 4.25 (B) – STATIC PRESSURE PROFILES FOR SWIRLING OUTFLOW AND $\xi = 0.2, 0.4$	123
FIGURE 4.26 - COMPARISON OF STATIC PRESSURE FOR SWIRLING AND NON-SWIRLING OUTFLOW	125

NOMENCLATURE

A, B	arbitrary constants
A', B'	arbitrary constants
h	half gap size, m
r	radial distance
m, n	dummy variable
p	static pressure, Pa
R_{in}	disc radius, m
V_{rin}	Inlet average radial velocity, m/sec
$V_{\theta in}$	Inlet average tangential velocity, rad/sec
Re	Reynolds number, $V_{rin} h / \nu$,
Re_r	reduced Reynolds number, $Re \cdot \xi$
Re_c	critical Reynolds number
Re_t	transition Reynolds number
r, θ, z	polar coordinates, m, rad, m
s	swirl ratio, $V_{\theta in} / V_{rin}$
V_r	dimensional radial velocity
V_{θ}	dimensional tangential velocity
u	dimensionless radial velocity
v	dimensionless tangential velocity, m/s
V	ave dimensional tangential velocity
x, y, z	Cartesian coordinates, m
g, k	arbitrary constants
E_n, B_n	Fourier function
x_j, x_k	dummy variables

Greek Symbols

δ	variable, $\delta = \eta^2$
β_n	eigenvalues
$\Delta\Pi$	dimensionless static pressure, $\Delta\Pi = 2 \eta^2 (\eta^2 - 1) \Delta p$
Δp	dimensionless static pressure, $[p(r) - p_{in}] / \rho v_{rin}^2$
ζ	dimensionless axial coordinate
η	dimensionless radial coordinate
μ	dynamic viscosity, $N \cdot \text{sec}/m^2$
ν	kinematic viscosity, m^2/s
Ξ	general dimensionless pressure function
ρ	density, kg/m^3
$\phi(\eta), \psi(\zeta)$	dimensionless velocity functions
β	separation constant
Φ	general dimensionless velocity function
ω	rotational speed, rads/s
λ	dimensionless parameter, $\sqrt{\frac{(\eta^2 - 1)Re_r}{2\eta^2 \ln(\eta)}}$
α	constant, $\alpha = \frac{\beta_n^2 + \beta_m}{2}$
Δ	parameter that signifies change

Subscripts and Superscripts

in	properties at the inlet
max	maximum value of the quantity
r, θ , z	radial, tangential, and axial component

Ἐν πρώτοις τελεῖται παρατήρησις, διὰ τῶν αἰσθήσεων καί
εἶτα ἔπεται ἡ περί τῶν παρατηρηθέντων σκέψις καί ἡ
ἐρμηνεία αὐτῶν διὰ τῆς ἀποκαλύψεως τοῦ λόγου τοῦ
διέποντος ταῦτα. Ἡράκλειτος

*First an observation is made through the senses,
and after the thought about the things observed,
followed by the explanation uncovering the
reason that governs their behavior.*

Heracletos, 500 B.C.

Chapter I

Introduction

1.1 The Problem

The flow between two closely - spaced parallel stationary discs is of both educational and practical importance. Two types of fluid motion can be generated in the disc-like domain and relaminarization may occur in both flows. [1] Outflow or source, is one type of flow where the fluid is admitted through a centrally located hole and is discharged through the periphery. In this case, the streamlines diverge and the static pressure increases from the center towards the periphery. As a result of the area increase, the velocity decreases and an adverse pressure gradient develops. Moreover, if the local Reynolds number decreases sufficiently, the phenomenon of relaminarization takes place as the laminar sub layer thickens and reverse transition from turbulent to laminar flow occurs.

Inflow or sink is the second type of motion, where the fluid is admitted via the periphery and is discharged through a centrally located outlet. In this case, the streamlines converge streamwise, causing an area decrease. As the velocity increases, a

favorable pressure gradient develops. The accelerating flow is characterized by its stabilizing effects (flow is moving in the direction of a monotonically decreasing pressure gradient), which tend to laminarize the flow even at very high Reynolds numbers and a flow that was originally turbulent.

The radial flow between two closely spaced stationary discs has many practical applications in industry. Outflow can be found in radial diffusers, centrifugal compressors, air bearings, squeeze film dampers, VTOL aircrafts with centrally located pointing jets, and in air cushion vehicles. The applications of the inflow can be found in double disc valves, thrust bearings, face seals and in flows near the exit of a geothermal reservoir.

Swirling flow can also be generated between the two stationary parallel discs for both inflow and outflow. The study of swirling motion is very important due to its presence in a variety of industrial applications such as gas turbines, nuclear reactors, and in other fields, such as heat exchangers.

1.2 Literature Survey

Previous studies on radial flow under investigation have been conducted experimentally, analytically and numerically. The literature survey is classified according to the aforementioned areas for the inflow and outflow.

1.2.1 Inflow

DeSantis and Rakowsky [2] investigated the problem of the sink flow between two discs with and without swirl. Their experimental analysis using hot-wire anemometry, was confirmed partially by several analytical studies. For the non-swirling sink, they found that the flow-field for all cases tested ($300 < Re < 1600$) was mainly laminar. The integral momentum method on a flat disc was modified for the accelerating flow, and resulted in boundary layer displacement and momentum thickness distributions. These distributions agreed well with the experimental data, assuming that the radial velocity follows the $1/r$ law, the flow is primarily inviscid, and that the boundary layer development is very thin (accounts for $< 10\%$ of the flow field). Also, fully developed velocity profiles occurred at sufficiently small gaps (disc spacing of 0.060 in) while the entrance length was well approximated by the analytical solution. The shear stress was found to increase sharply with decreasing radius, and that was due to the accelerating flow. For the swirling sink, radial and tangential velocity profiles were obtained, where the former ones increased monotonically and the latter ones displayed some scatter. The boundary layer displacement thickness showed that it is not zero at the periphery (due to the porous coupler), while the momentum thickness displayed similar shape as the one for the non-swirling case with its maximum occurring at a slightly larger radius. Moreover, the vortex strength was found to decrease in a linear manner with a decreasing radius, and with almost the same rate for Reynolds numbers of 300 and 1500, while the shear stress increased abruptly with a decreasing radius.

Murphy, Coxon and McEligot [3] investigated numerically the laminar sink flow between two parallel discs taking into account both the inertia and viscous effects. The results revealed that at large radii, the viscous effects are dominant, thus causing the velocity profiles to shift from a uniform profile at the entry to a parabolic shape. In addition, the boundary layer thickness became equal to half the spacing, and the pressure varied logarithmically with the radius. As the radius decreased, the acceleration effects grew stronger, the velocity profiles were tending toward flat profiles and the boundary layer became thinner. Conversely, the pressure distribution was well predicted by the inviscid Bernoulli equation. The numerical results showed a high friction factor at entrance due to the assumed uniform velocity profile, which shortly merged with the value obtained from the creeping flow solution at larger entry radii. In general, the results revealed that the velocity profiles and the friction factor tend to approach downstream, the values obtained at larger entry radii.

Murphy, Chambers and McEligot [4] studied experimentally and numerically the inflow between two stationary parallel surfaces. A circular test section was employed to examine the laminar flow and a segment of a circle was utilized to test turbulent flow. For the first case, the experiment agreed well with the laminar analysis for local Reynolds numbers from 210 to 21000. Beyond that range, there was a change in the flow regime to a turbulent one. The former findings were also confirmed by employing smoke – flow visualization techniques.

Lee and Lin [5] attempted to solve numerically a differential equation derived for the pressure without assuming or developing any velocity profile for the *inflow* of two narrowly spaced discs. The Runge – Kutta method was employed to solve the linearized

r-momentum equation. Their results predicted a pressure distribution which agreed with previous experimental work, indicating the two limiting positions that corresponded to creeping and potential flow respectively.

Vatistas [6] solved analytically the problem between two narrowly spaced stationary discs, by deriving equations for the radial pressure distribution, the radial velocity and the global friction coefficient. He obtained simple closed-form solutions by considering only the average changes of the radial momentum in the radial direction. Comparing his results with previous theories, it was concluded that the pressure drop along the radius must be partly due to inertia and partly due to viscous effects. Moreover, it became apparent that the maximum velocity in every radial position is 1.5 the local average. The closed-form solution was found to be in very good agreement with previous experimental data and the theoretical results of Lee and Lin. [5]

Vatistas [7] also focused on the radial inflow between two discs, and obtained closed - form solutions of the linearized momentum equations of Lee and Lin. [5] The creeping and inviscid flows were found to be the asymptotes of the general problem. From the analysis, it became evident that for high Reynolds numbers ($Re_r \cong 100$), the velocity acquired a flat profile, except near the surface of the discs where it revealed the presence of a boundary layer. For low Reynolds numbers, the flow exhibited the Poiseuille flow parabolic profile. By comparison with the author's previous work, it was found that the difference between the equations for moderate values of Reynolds numbers is no larger than 12.5% ($Re_r \cong 0.27$). Moreover, the present equations of the pressure drop were in accordance with his previous equations, as well as with earlier experimental findings for low Reynolds numbers ($0.081 < Re_r < 0.0084$).

Singh [8] investigated experimentally and theoretically the inflow between two discs. For the turbulent flow between two stationary discs with full peripheral admission, the experimental results revealed that, with increasing inlet local Reynolds number, and a decreasing gap and diameter ratio the pressure drop increased. Moreover, the Laser Doppler Anemometry measurements revealed that the velocity profiles were not symmetric near the exit, and the maximum radial velocity was shifted towards the disc with the exit outlet. The turbulence intensity was also measured and was found to decrease in the direction of flow despite the increasing local Reynolds number.

Zitouni and Vatisas [9] developed solutions for the radial flow between two parallel discs using infinite power series. The power series was then solved numerically to obtain results for the radial velocity and the static pressure distribution for the steady, laminar and radial flow. These results were presented as functions of the non-dimensional parameter λ that combined the dimensionless radial distance and the Reynolds number. The results were then compared with previous theories and experimental data and were found to be in close agreement. Also, the two flows, inflow and outflow, were found to be dramatically different except for λ close to zero, where in both cases the velocity exhibits the parabolic Poiseuille profile. For the inflow, as λ increases, the velocity profile flattens and the boundary layer thickness decreases. As λ tends to infinity, the velocity becomes flat (mid-plane), and the boundary layer thickness tends to zero and a discontinuity is emerged at the wall. For the outflow, the maximum velocity occurs at the mid-channel, thus indicating that the bulk of the flow occurs near the center of the channel. Two critical values of λ were obtained for this case. The first one indicates the point where the pressure changes sign due to the forces interaction, and the second one,

where the derivative of the axial velocity becomes zero. Beyond that value purely decelerating flows cease to exist.

Ghaly and Vatistas [10] solved numerically the inflow and outflow between two stationary discs, and obtained the velocity and pressure distributions by solving a 3^d-order non-linear differential equation using a shooting method. The equation was written as a system of a 3 non-linear first order differential equations, which was then solved as an initial value problem using the shooting method. The Runge-Kutta was used to integrate the resulting set of equations. The solutions were then compared with previous experimental work and were found to be in fair agreement. The results were found to be very similar to the ones by Zitouni and Vatistas [9]. The present solution provided a simpler method in obtaining results, without the inconveniences encountered by the power series solution.

Singh, Vyas and Powle [11] examined the inward flow between two discs from an experimental and a numerical point of view. Both studies revealed that the phenomenon of relaminarization for the accelerating flow occurs, and that the responsible governing parameters were the acceleration parameter and the gap ratio. Laser Doppler Anemometry was used to measure the velocity distributions as well as the turbulent intensities. The velocity distributions revealed increasing symmetrical profiles as the fluid approaches the exit. Furthermore, the profiles exhibited an asymmetry towards the disc that has the exit hole. The turbulent intensities were shown to be maximum near the disc walls and displayed a decreasing trend towards the core flow region. This indicated that the accelerating flow has suppressed the turbulent fluctuations. It was also observed that the presented turbulent κ - ϵ model predicts well the experimental findings. Moreover,

numerical predictions showed that the turbulent kinetic energy decays faster for smaller gaps. These findings led to the conclusion that a decreasing gap ratio has a stabilizing effect on the flow, as does the acceleration parameter.

Wormley [12] developed a momentum integral analysis to investigate the swirling inflow in a short vortex chamber, by taking into account the interaction between the core vortex flow and the end wall boundary layers. To determine flow characteristics, he employed the visualization techniques of air bubbles and the injection of powdered milk. Wormley defined the swirl strength as the ratio of the ideal peripheral tangential velocity to the radial velocity at r_0 defined positive in the $-r$ direction. It was observed that at low swirl strengths, radial flow exists at almost all axial positions in the chamber. A further increase of the swirl caused the radial flow to penetrate the mid-plane of the chamber. At very high swirl strengths, the “milky donut” preserved its stable pattern for a long period, indicating a lack of radial flow through the area in the chamber, and revealing that the radial flow must be enclosed at the end wall boundary layers. Conversely, the analytical model considered two flow regions: the developing region, and the developed one, where all radial flow is contained in the end wall boundary layers. The momentum integral analysis predicted a trend of the static pressure distribution that was in accordance with the experimental data. The momentum integral analysis also showed that the non-dimensional circulation, as well as the pressure in a short vortex chamber, is depended on a dimensionless parameter boundary layer coefficient.

Savino and Keshock [13] performed an experimental study on swirling inflow between a flat cylindrical chamber of a medium aspect ratio (aspect ratio $\xi=0.107$). It was observed that the radial velocity profiles displayed uniform profiles from the inlet to

halfway through the cylindrical chamber and then they were disturbed. Moreover, it was shown that most of the inflow is directed (or swallowed) along the discs, with the maximum radial velocity occurring close to the discs' surface. This explains the spikes in the profiles, which increased with decreasing radius. In addition, the velocities at mid-channel were very small and were directed in the outward direction. On the other hand, the tangential velocities displayed uniform profiles and showed some asymmetry at the surface discs accompanied by a small depression in the center, as they approached the exit. That could be due to the interaction of the swirl, radial and tangential flow components and the no-slip conditions at the walls, forcing the tangential velocities to behave like an inviscid vortex. As air entered the chamber through the vanes, the centrifugal force field was stronger than its inward momentum, diverted the air axially towards the walls. The centrifugal effects were smaller close to the walls, and the radial momentum increased with decreasing radius. It was also found that the degree of swirl imparted to the flow determines the amount of mass flow that will flow inwards within the end wall boundaries. Lastly, the measured static pressure distribution matched well with the calculated pressure, based on the centrifugal and pressure forces, as well as the tangential velocities.

Kwok et al [14] conducted an analytical investigation on the swirling inflow within the annular region of a short cylindrical chamber using Wormley's technique [12], which was then solved numerically. The aim of this analysis was to study the behaviour of the apparent viscosity and to determine its magnitude. An empirical expression was found for the apparent viscosity (sum of laminar and eddy viscosity), and its magnitude was shown to vary from 7000μ at the chamber's periphery, to 4500μ at the exit plane. It

was also found that the apparent viscosity seriously affects the velocity profiles in the vortex chamber. Specifically, the comparison of the experimental results with the corresponding analytical ones revealed a very good agreement for the tangential velocity distributions. However, for the radial velocities, there is a discrepancy in the boundary layer region, as well as and in the core region. That can be explained by the fact that the exit axial velocity distribution and the compressibility effects of the flow affect the flow in the vicinity of the exit plane. On the other hand, the pressure was found to decrease slowly from the periphery up to halfway along the chamber and then decreased quickly as the flow approached the exit. This indicates that the flow moved towards a more favorable pressure gradient vicinity near the exit, hence the vortex flow accelerated according to the angular momentum conservation. For the same reasons, it was shown that the analytical boundary layer distribution increases as the flow moves inward, reaches a maximum and then decreases towards the exit plane.

1.2.2 Outflow

McGinn [15] used dye filament techniques to visualize the flow of water between two stationary parallel discs. He also obtained the static pressure distribution for both converging and diverging flow. At the diverging or source flow, as the flow rate increased, axially symmetric vortex sheets were formed between the plates. At high flow rates, sinusoidal waves were observed propagating downstream over the discs' surfaces, generating eddies. Both steady state and transient cavitation was present. The converging flow displayed a laminar character even at very high flow rates. A stability criterion was established analytically, revealing that for the converging flow there is a discrepancy between the experimental and the theoretical data over the entire flow region. Consequently, the theoretical model is not realized by the converging flow, since it assumes a parabolic velocity profile and ignores the developing region. For the diverging case, this effect is less prominent, and for the stability factor (or criterion) less than one, no boundary layer separation occurs and the experimental pressure data is also in agreement with the data predicted by theory.

Livesey [16] probed on the effects of inertia on the steady, incompressible, viscous flow between two parallel stationary discs. The effects of inertia were estimated by solving the equation of motion in its integral form, as was suggested by von Karman. He considered the r-momentum equation by including the inertia term and assuming zero velocities in the y and θ directions. He then assumed a two-dimensional parabolic velocity profile, which in turn substituted in the r-momentum equation. After integrating the resulting equation across the film thickness and at any radial distance, the

contribution to the pressure changes due to inertia was estimated. It was concluded that for moderate velocities and consequently for low Reynolds numbers, the inertia effects may be more significant than the viscous effects that could change the sign of the radial pressure gradient.

Morgan and Saunders [17] performed an experimental study to investigate the importance of the inertia effects for radial flows between two discs and for low Reynolds numbers. Previous analysis by Livesey [16] supported that for the same type of flow, the inertia effects could be considerable even for low velocities. Their experimental results clearly showed that pressure is better represented by a solution that includes both the viscous and inertia terms for low flow rates. The results however were insufficient to confirm Livesey's theory [16].

Moller [18] investigated the outflow between two parallel, stationary, narrowly - spaced discs with no swirl. He conducted an experimental and theoretical analysis, from which he obtained approximate solutions for the radial pressure distributions for both laminar and turbulent flow, using the integral momentum method. His experimental results were in agreement with theory for both flows as the radial distance decreased, especially when the inlet corner was shaped. Reverse transition was detected at a critical Reynolds number of 2,000, which complies with the flow in circular pipes and 2-dimensional channels. He also claimed that the phenomenon of relaminarization occurs because of the thickening of the always-present laminar sub-layer up to half the channel width. In some instances, separation and reattachment of the flow were observed near the entry corner. The reattachment distance and minimum bubble pressure were found to depend only on the channel gap, provided that the diameter ratio is sufficiently large to

accommodate the reattachment, and that the local Reynolds number at the reattachment point is larger than 15,000.

Savage [19] investigated the laminar viscous outflow between two stationary parallel discs. He obtained a solution by perturbing the creeping flow solution and carried out an expansion in terms of the downstream coordinate. His solution for the pressure distribution was in very good agreement with Moller's experimental data [18], except near the inlet where it decreased below the experimental results, due to the entrance effects. Since the inlet pipe diameter is much larger than the disc spacing, the inlet pipe operates as a plenum chamber, therefore resulting in an almost uniform velocity profile at the entrance. Savage estimated the inertia contribution to be approximately 30% higher than the one predicted by Livesey [16]. Livesey's solution [16] was above the experimental data due to the assumed parabolic velocity profile, which results in a higher wall shear stress compared to the one if the inertia terms were considered.

The phenomenon of the reverse transition of radial outflow at low speeds by direct hot-wire measurements was studied experimentally by Kreith [20] who confirmed earlier analyses that the point where reverse transition occurs is independent of the turbulence level at the entry duct. He also concluded that, the necessary condition for reverse transition to take place is the existence of a laminar velocity profile that does not have an inflection point.

Jackson and Symmons [21] carried out the experimental study of the pressure distribution for the radial laminar source flow between two stationary closed spaced discs with a very small centrally located inlet. The experimental results revealed that for gaps of 0.01 and 0.02 inches of clearance at all flow rates, and for low flow rates at 0.03 and

0.04 inches of gap, the pressure distribution implies the presence of a symmetrical flow through the discs. As flow rates and gap increase, asymmetry and instability emerged in the flow, thus indicating the presence of flow separation. Moreover, any disturbance at the entry flow will be carried on as the fluid as it progresses, and will cause non-uniformity in the pressure distribution. In comparison with theory, it was shown that the experimental inertia effects are significantly larger than the theoretical ones when the Reynolds number and radial distance increase. Jackson's and Symmons' experimental investigation indicated the limitations of the existing theory in the presence of substantial adverse pressure gradients in the central area of the discs where the flow is unstable and asymmetrical.

Moller [22] following his previous studies on source flow, investigated experimentally and theoretically the geometrical and flow parameters of a radial, non-swirling, incompressible flow diffuser, and proposed the development of an efficient inlet bend from the supply pipe outlet to the radial channel. His experimental results showed that the pressure recovery of a radial diffuser agree with theory for Reynolds numbers (inlet pipe Reynolds number - Re_d) $> 2 \times 10^5$ and fairly thin boundary layer at the pipe exit. Moreover, the pressure recovery of the radial diffuser was comparable with a 7° conical diffuser at high Reynolds numbers, which are likely in internal flow systems. For $Re < 2 \times 10^5$, the pressure recovery decreased rapidly and deviated significantly from theoretical predictions. Moller also observed that the pressure recovery decreases, with decreasing Reynolds number, and with a fully developed boundary layer thickness at the inlet, for both radial and conical diffusers.

Boyack and Rice [23] studied the case of steady, incompressible, axially symmetric, laminar and Newtonian fluid for the radial outflow between two parallel, narrowly - spaced, stationary discs. They obtained an integral solution in order to investigate the ranges of Reynolds numbers and radii for which Savage's expressions for the velocity and pressure distributions are valid. An 8th order polynomial was derived that describes the radial and axial velocities, including the velocity profiles that exhibit inflection points. To compare the integral method and Savage's solution, the inlet velocity profiles derived from Savage were used in the integral method since the method itself cannot generate velocity profiles. The comparison between the two approaches showed that, as the Re increases, the radius, where there is agreement within 1%, also increases. For $Re > 1.75$, the discrepancy is greater than 1% throughout the entire flow regime, while for $Re < 0.075$, the difference between the two solutions is less than 1%. The integral method has also been used for the radial inflow between two parallel co-rotating discs in a more complicated form.

Kawaguchi [24] investigates experimentally the entrance loss in the turbulent radial source flow between two stationary parallel discs. He examined the range of the inlet region, minimum pressure, hydraulic loss in the vicinity of the entrance, and the entrance form to influence upon inlet loss. He derived an empirical equation using the Navier-Stokes equations, the velocity profile for turbulent flow, and the dimensionless quantities related to the spacing between the two discs and the radius of the rounded inlet corner. The parameters that influence the entrance loss are the following: the irregular velocity distribution just before the inlet, the contracted flow, back flow on the disc surfaces and separation. The experimental results showed that the smaller the roundness

of the inlet corner, the larger the local maximum velocity in the center of the gap becomes near the entrance. It was also found that the transition from laminar to turbulent flow takes place near the inlet when the Reynolds is $200 \sim 500$, and that the turbulence expands outward in the downstream direction. Moreover, as the gap gets smaller, the coefficient of the entrance losses ξ increases, and if the gap gets larger even with a small roundness at the entry, the separation and contraction causes an increase of the ξ . Also, the pressure difference at the entrance and outlet can be estimated only by the viscous term without taking into account the inlet boundary shape.

Bakke, Kreider and Kreith [25] conducted an experimental analysis on the turbulent source flow between two parallel stationary and co-rotating discs. For the stationary discs, as the fluid flows radially outwards and the Reynolds number decreases, the velocity profiles obtained a quasi-parabolic distribution with increasing radius. The flow has not yet become laminar since the turbulent intensity remains quite high at large radii. Since the flow is decelerating, an adverse pressure is developed, which in turn produces inflection points in the velocity profiles close to the discs' surfaces. For the case of co-rotating discs, the centrifugal forces become larger as the radius decreases, and the radial velocity profile develops a maximum near the disc for large angular velocities. The velocity profiles develop an inflection point at the same radial distance as in the case of the stationary discs. This point later disappears along with the turbulence intensity, due to the stabilizing effects of the centrifugal force, which increase with increasing speed. A further increase in the velocity causes an increase of the turbulence intensity. This is due to the increasing shearing force between the discs and the fluid. The static pressure distribution increases smoothly for the stationary discs towards the disc rim, whereas for

the co-rotating discs, the centrifugal effects cause a fast raise in the static pressure near the disc rim and with increasing rotational speed an inflexion point is being created in the pressure profile.

Raal [26] solved the Navier Stokes equations for the stream function and vorticity formulations using Allen and Southwell's discretization procedure. The following inlet conditions were considered: a) where the flow is uniform at the entrance assuming no vorticity, and b) a uniform irrotational flow at a plane r upstream from the entrance, where vorticity diffusion is allowable. For the first case, it appeared that separation occurred for $Re \geq 60$. For the second case, separation occurred at $Re = 64$ and as Reynolds increased, the vorticity diffusion increased in the upstream direction, the size of the recirculation zone increased, and the separation point moved upstream. For $Re \geq 75$, a small concavity was observed in the radial velocity profiles, thus making evident the presence of a reverse flow. Near the entrance the centerline velocities revealed the presence of inflexion points for $Re > 1$, thus departing from the creeping flow profile. The findings of the second case proved that the assumption in the first case is not a pragmatic one, thus it should be discarded.

Wark and Foss [27] attempted to develop a lifting device by performing an experimental analysis that would determine the force acted on the impact disc for the radial outflow between two parallel discs. For moderate Reynolds numbers, a repelling force exists for small and large disc spacing, whereas an attracting force will be present for the intermediate ones. The parameters that influence the presence or absence of the reattachment location will also affect the force exerted on the plate. The flow regime of interest can be identified in the following categories: a) where no reattachment occurs if

the ratio of the impact disc diameter to the jet nozzle diameter $D_2/D_1 \rightarrow 1$ and/or the non-dimensional disc spacing $h^* \rightarrow \infty$, b) where reattachment always occurs if $h^* \rightarrow 1$ and/or $D_2/D_1 \rightarrow \infty$, and c) where Reynolds number plays a qualitative role in the flow field for intermediate values of the non-dimensional disc spacing and D_2/D_1 . From the experiments, it was observed that, for small non-dimensional disc gap ($h^* \leq 0.2$), and diameter ratio of $D_2/D_1 \geq 5.33$, the pressure and the force on the impact disc decrease, as the Reynolds number increases while the flow pattern remains qualitatively unaffected. At D_2/D_1 equal to 4, and because of the interaction amongst the geometrical parameters, the separation stream surface reattaches to the source plate. Consequently, at the path of the separation stream surface, the intermediate pressures will have a minimum value. In the regime where $h^* \geq 0.2$ and $5.33 \leq D_2/D_1 \leq 8$, the impact force was found to be independent of the Reynolds number. It was also concluded that there is an optimum diameter ratio for a given non-dimensional gap height between the discs and Reynolds number, where the attraction force is maximum.

Mochizuki and Yang [28] studied the problem of instability for the radial source flow between two parallel discs. They also solved numerically the unsteady vorticity transport equation, and provided predictions on the vortex formation and separation, which were confirmed partly by experiments. The following different flow patterns were observed for Reynolds numbers between 1.5 and 50: a) for $Re < Re_c$ ($27.5 < Re_c < 30$) steady flow with no separation or re-attachment, b) for $Re_c \leq Re < Re_t$ self-controlled oscillation which decays downstream, and c) for $Re > Re_t$ ($31.4 < Re_t < 45.5$), a self-controlled flow oscillation followed by a reverse transition. In the experimental approach, the flow visualization methods of dye-injection, Hydrogen bubble generation, and paraffin mist,

were employed to both liquid and gas flow systems. For the liquid flow system, hydrogen bubble and dye injection were used to visualize the flow. The hydrogen bubbles showed that as the Reynolds number increases up to, or beyond a critical number, flow separation occurs at the same radial position alternately on both discs, thus creating a vortex sheet. At further increase of the Reynolds number the flow becomes turbulent due to flow oscillations. However, when the velocity, which decreases with increasing radius, reduces adequately, the phenomenon of relaminarization occurs. The dye injection method (for the liquid flow system) and hot wire measurements using air stream, indicated the presence of vortices as well as their axisymmetrical periodic formation. The development of vortices was also realized in the air stream by means of paraffin mists. It was proved that the vortices develop in an unsteady manner and separate periodically and alternately from both discs.

Tabatabai and Pollard [29] performed an experimental study on the radial outflow between two discs emphasizing the turbulent flow regime. Their analysis showed that for large Reynolds numbers, the flow is similar to the two-dimensional fully developed channel flow. As the Reynolds number decreases, the velocity profiles transform to parabolic ones, and the viscous sub-layer thickens. That indicates that it is being transformed into a laminar-like boundary layer. Moreover, the magnitude of the turbulent intensity decreases and the point of its maximum value moves away from the wall, thus making the turbulent decaying process more complicated when compared to the one observed in the channel flow. Even though the Reynolds number is low, turbulent characteristics still exist in the flow, thus indicating that relaminarization occurs slowly.

Ervin, Suryanarayana, and Hon Chai [30], analyzed experimentally the aspects and characteristics of the turbulent outflow between two stationary discs, using split film anemometry (split film probe attached to a micrometer traversing mechanism). Their results showed that the flow is unsteady near the entrance, and for low Reynolds numbers, the velocity distribution at the exit approaches a parabolic profile thus resembling a laminar flow. Also, the universal velocity profile is not applicable at small radii, but there is an agreement with the experimental data away from the inlet. At high Reynolds numbers, and for $r > 0.5$, the results seem to follow the velocity defect law, except close to the exit ($r = 0.93$). That might be due to the fact that the phenomenon of relaminarization has been initiated. This is supported by the fact that, at $0.93 < r < 1$, the velocity profiles were almost parabolic, turbulent stresses in that region were small, and lower energies at higher frequencies were observed. Simultaneously, high levels of turbulence were also present in the flow, which indicates that the turbulence in the flow is persistent. The criterion for relaminarization of the flow by Kreith [20] was examined, and a smaller constant in his equation provides satisfactory agreement. Finally, it was noted that uncertainties related with the employment of the split film anemometer probe had not been established.

1.3 The Contribution

The intention of the present thesis was to investigate the study of the radial flow between two discs. Specifically, the contributions to the subject are the following:

- (i) Development of analytical expressions for the radial and tangential velocities as well as static pressure distribution for swirling inflow and outflow between two closely - spaced discs.(such that the axial velocity component to be considered negligible)
- (ii) Experimental analysis for the non-swirling inflow for small and intermediate heights and Reynolds numbers. Present data include gap ratios of 0.0278, 0.01389, 0.01042, and 0.00694 versus 0.03, 0.05, 0.0394, and 0.0197 reported by previous researchers. The Reynolds numbers presented herein are in the intermediate range ($328.74 < Re < 657.49$) compared to others. Radial velocity and static pressure measurements were obtained.
- (iii) Static pressure measurements for the swirling inflow and low swirl strength of $s \cong 2$, and for the range of heights and Reynolds numbers reported above. Previous evidence pertains to a high gap and very high swirl number [13], or a low swirl, intermediate gap, but high Reynolds number [2].
- (iv) Experimental investigation in the outward flow without swirl. The present analysis is restricted in terms of intermediate gaps of 0.4, 0.2, 0.15 and 0.1 and moderate Reynolds numbers in the range of $3154.36 < Re < 9463.08$.

- (v) Experimental study on the swirling outflow for four different gaps of 0.4, 0.2, 0.15 and 0.1 and low to intermediate Reynolds numbers $3469.79 < Re < 6624.15$. Previous experimental data on this particular case have not been reported.

Chapter II

The Experimental Apparatus and Procedure

Physical experimentation ought to be the central component of every scientific investigation. This is the foundation of research and development. Tests on actual models should be carried out in order to explain, predict, and/or validate analytical results that have been deduced from physical laws and principles. It also serves as a measure of comparison with experimental outcomes that have been previously obtained. It is therefore essential that findings of analytical models be supported by experimental evidence.

The objectives of the present experiments were to obtain static pressure and velocity distributions between two stationary parallel discs, while the fluid is admitted from the extreme periphery or through a centrally located exit. The details of the experimental apparatus, measurement techniques, data analysis and treatment, are discussed in the following sections.

2.1 Experimental Planning and Procedure

The current experiments were thus made to fulfill the previously mentioned purpose with respect to the radial flow between two stationary, narrowly - spaced, parallel discs. The experimental objective was to measure the static pressure and the radial velocities for both inflow and outflow, with and without the presence of swirl, and for the gap sizes of 0.125, 0.1875, 0.25, and 0.5 inches between the discs.

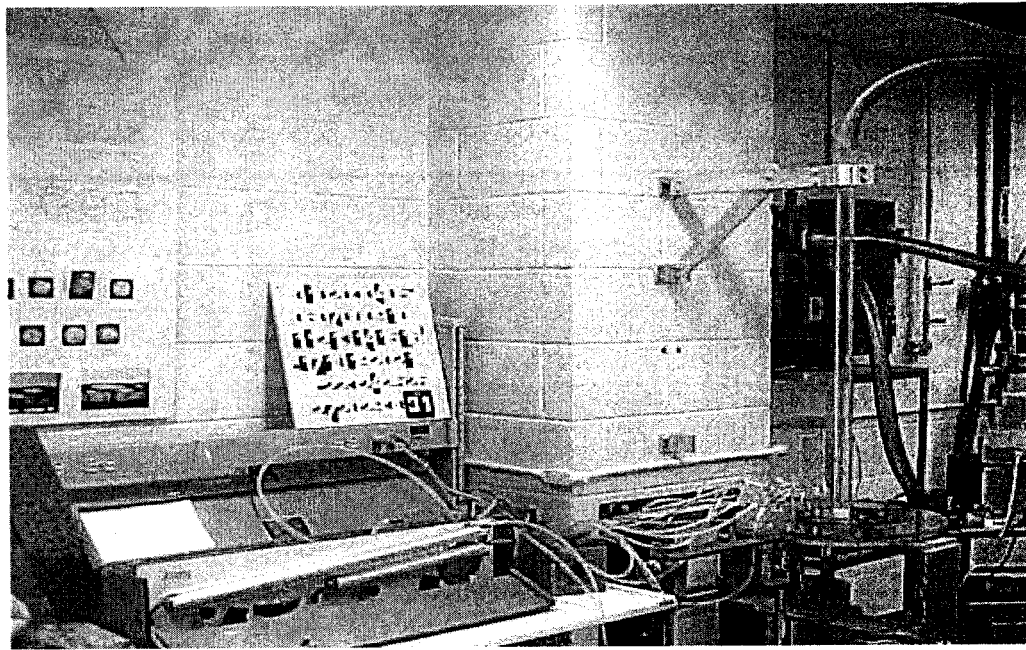


Figure 2.1 -- Experimental apparatus

In all cases, air at 1 atm and 25 °C was used as the working fluid. The range of the flow rate values varied from 20 to 60 cfm. The four heights of 0.125 in, 0.1875 in, 0.25

in, and 0.5in, corresponded to gap ratios ($\xi = 2h/D$ or $\xi = h/R$) of 0.0069, 0.01042, 0.0139, and 0.0278 respectively. (Figure 2.2)

In order to obtain accurate measurements, a set of sensitive inclined manometers, an accurate rotameter, and a thin Pitot-static tube were used to measure the static and dynamic pressures, as well as the flow rate of air. The above equipment was available commercially, and the reasons for selecting them will be discussed in the next sections. Three flow rates were selected for each of the four heights, and 10 measurements of static pressure along the radius were obtained.

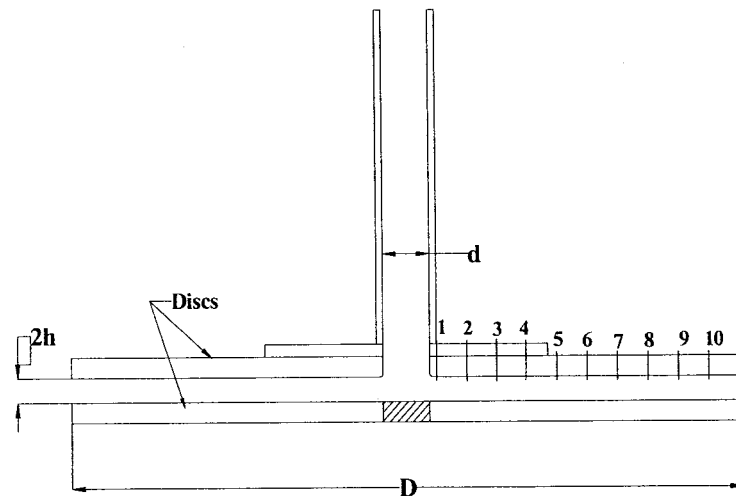


Figure 2.2 – Schematic of the discs

Exploratory tests, having theory as a guide, were conducted to identify possible experimental errors. Prior to the recording of data, we were able to ascertain the time needed for the system to stabilize. Moreover, while measuring static pressures through the control panel, it was observed that the manometer liquid took some time to return to

zero scale. Therefore, it was decided that after each pressure measurement, the manometer should be zeroed before proceeding to the next reading.

2.2 Instrumentation and Apparatus

2.2.1 Experimental set-up

The experimental apparatus consisted of the following: (i) two parallel discs (one of which was mounted on a vertical support which controlled the gap between the two discs, while the other was attached to a tube that was supported by a stationary mechanism on the wall), (ii) a blower, (iii) a pitot-static tube, (iv) a rotameter, (v) an assembly of inclined manometers, and (vi) vortex rings for both inflow and outflow. The schematics of the swirling flow for both inflow and outflow are shown in figures 2.3 and 2.4.

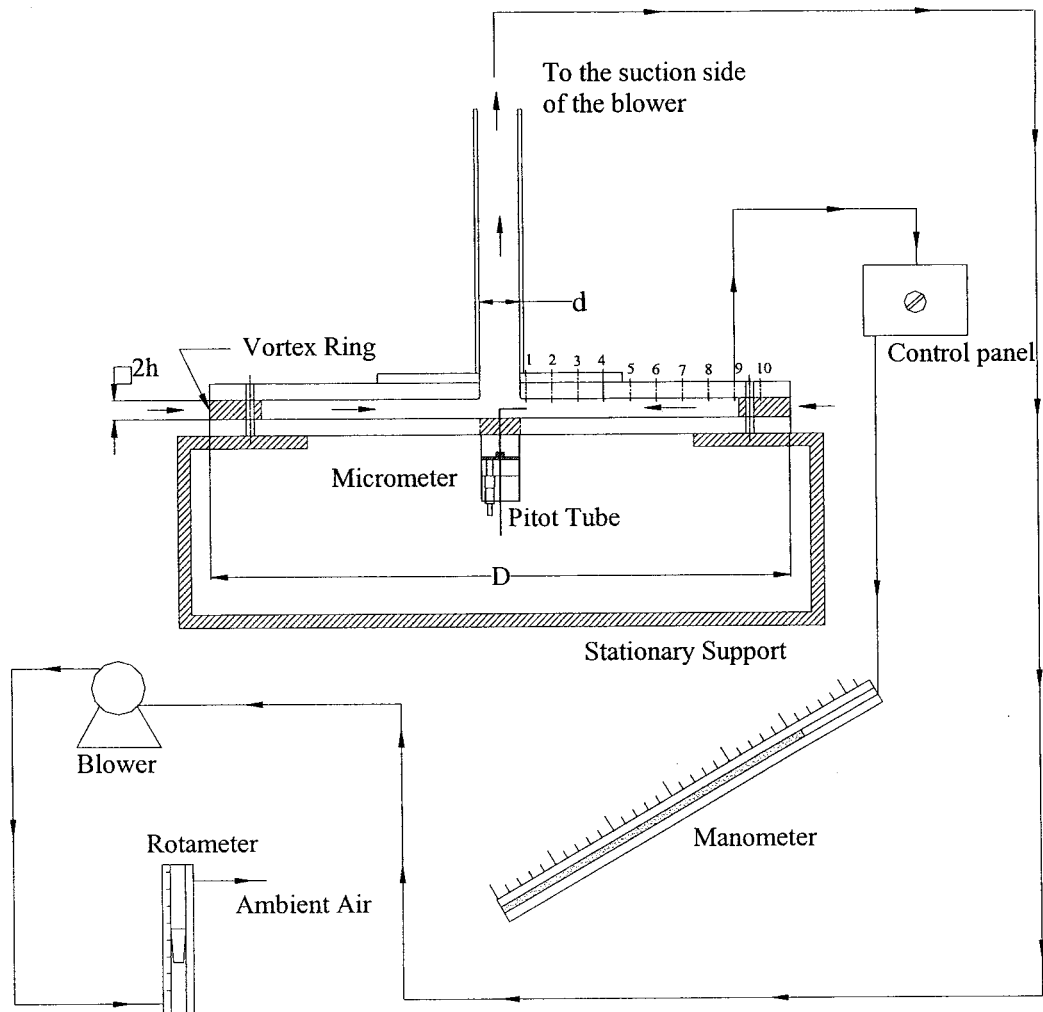


Figure 2.3 – Schematic of Inflow with Swirl

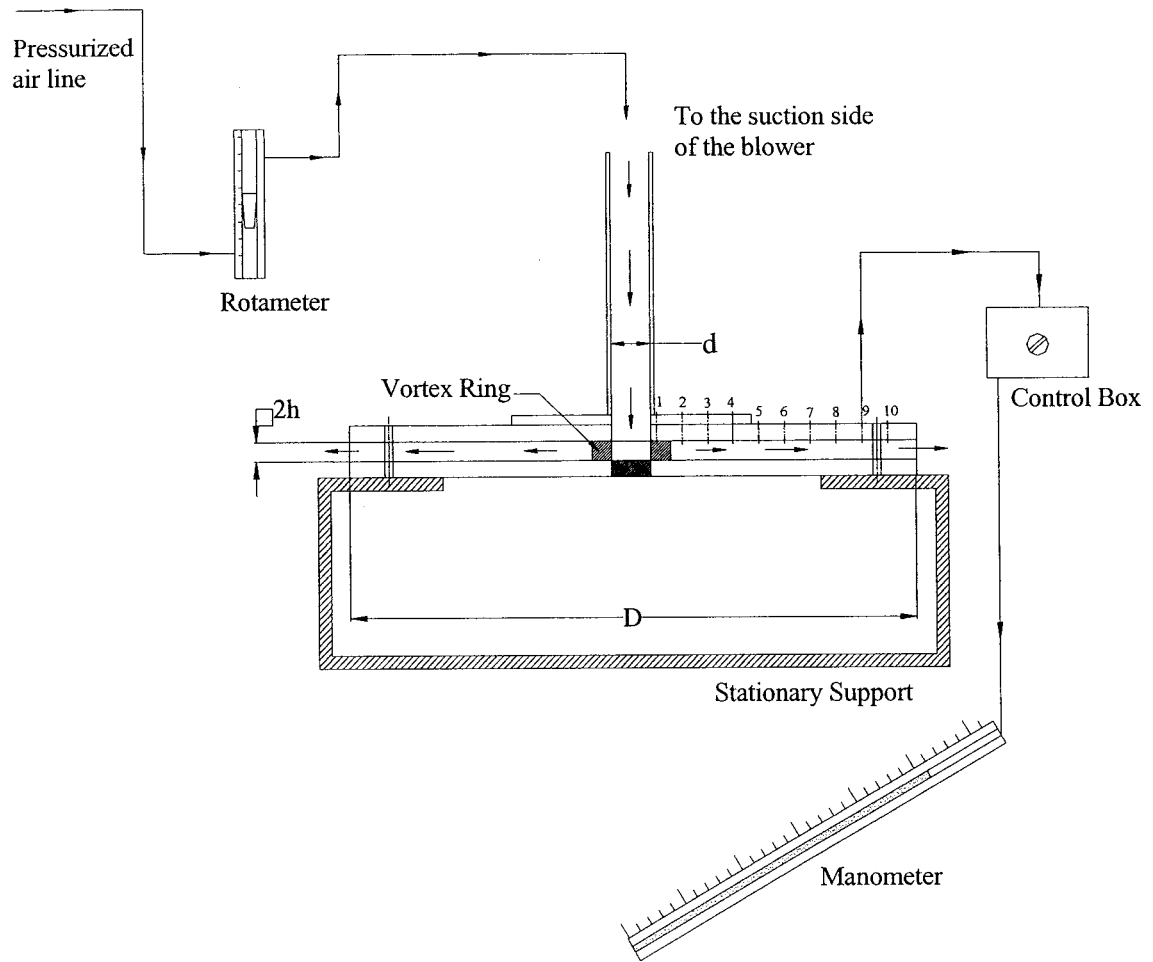


Figure 2.4 Schematic of Outflow with Swirl

2.2.2 Plexiglas Discs

The top disc was fabricated from Plexiglas. It had a diameter of 18 inches and a thickness of 0.5 inches. Eight holes of 0.25 inches diameter were drilled in the disc in order for it to be attached to the flange of the Plexiglas tube. The bottom disc was made

from two Plexiglas semi-discs with a thickness 0.5 inches and a radius of 8.625 inches. In the gap formed by the two semi-discs, an aluminum slider was fitted.

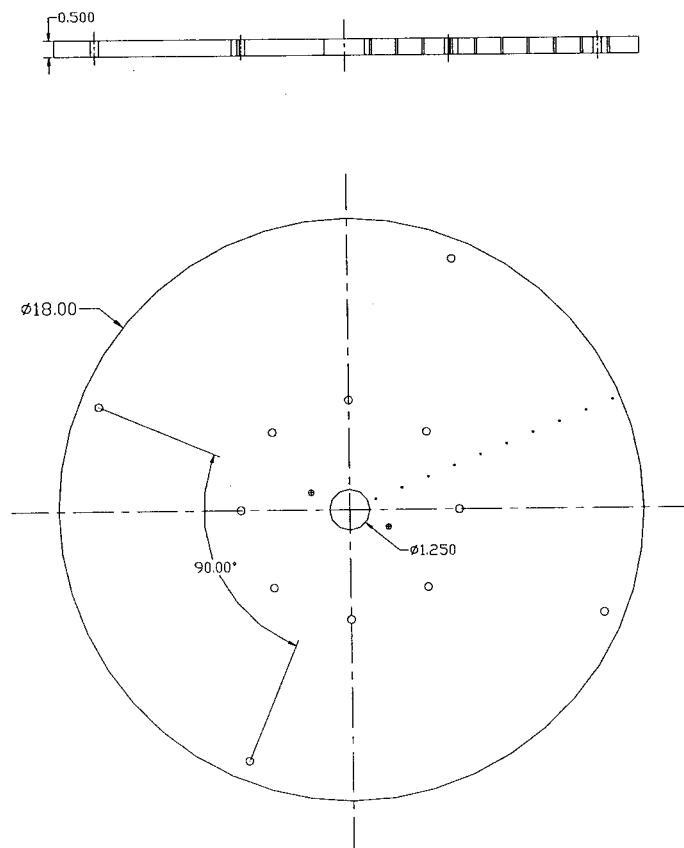


Figure 2.5 – Schematic of the top disc

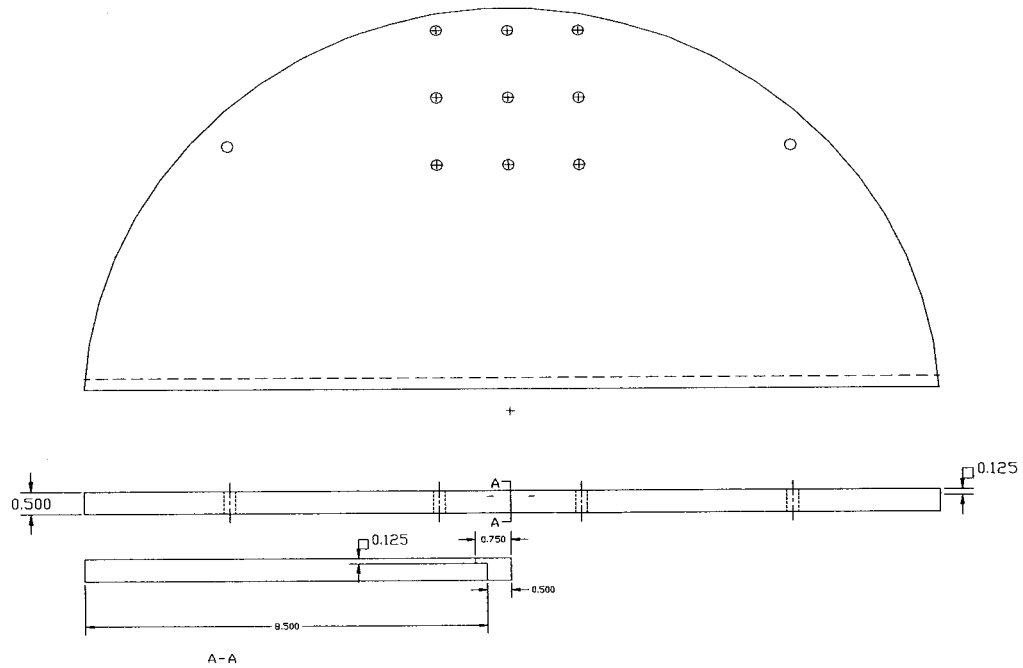


Figure 2.6 – Schematic of the bottom disc

2.2.3 Spacers

Four sets of cylindrical spacers having heights of 0.125 in, 0.1875 in, 0.25 and 0.5 in, and an inner diameter of 0.5 in were used to fix the gap between the two discs. The spacers were placed at the outer periphery in four diametrically opposite locations.

2.2.4 Vortex rings

Two sets of four aluminum vortex rings were used to introduce swirl for both outflow and inflow conditions. For the outflow (figure 2.7), four rings with a thickness of

0.125in, 0.1875in, 0.25 and 0.5 in, an inner diameter of 1.25 in, and an outer diameter of 2.99 in have been designed. A series of 18 flow guide vanes for the first three heights and 10 flow guide vanes for the ring with a thickness of 0.5 in, introduced high swirl to the flow of approximate strength of 2.

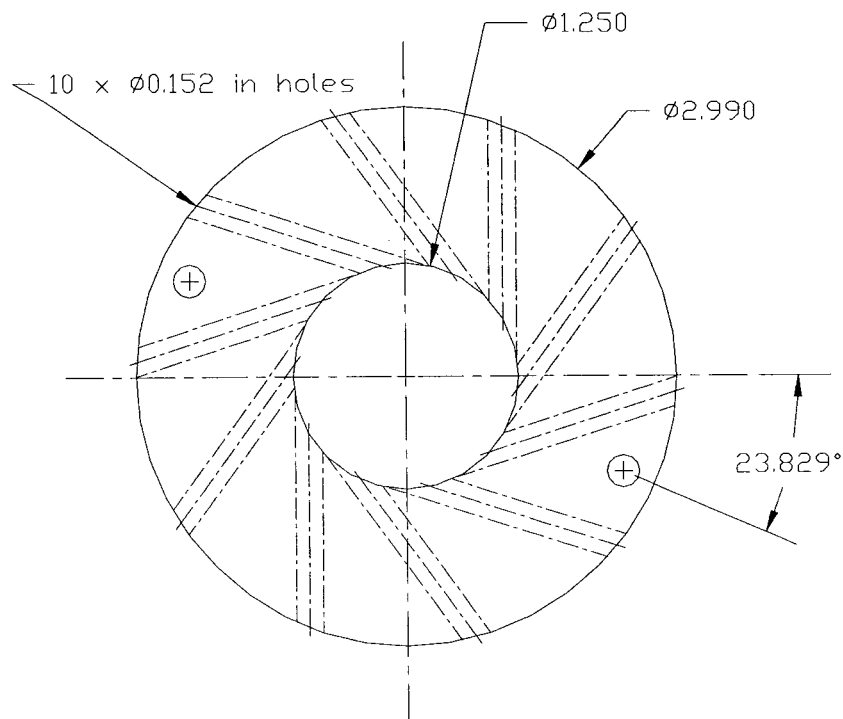


Figure 2.7 – Vortex Ring for Outflow (Source)

For the sink flow (figure 2.8), four sets of rings with a thickness of 0.125in, 0.1875in, 0.25 in, and 0.5 in, an inner diameter of 16.250 in and an outer diameter of 18.00 in, as well as 50 guide vanes, imparted swirl to the air while entering via the extreme periphery. The magnitude of the swirl was fixed and was controlled by the vane

angle of the vortex ring. In both cases, the angle between the radius and the tangent to the centerline of the vane was equal to 30 degrees.

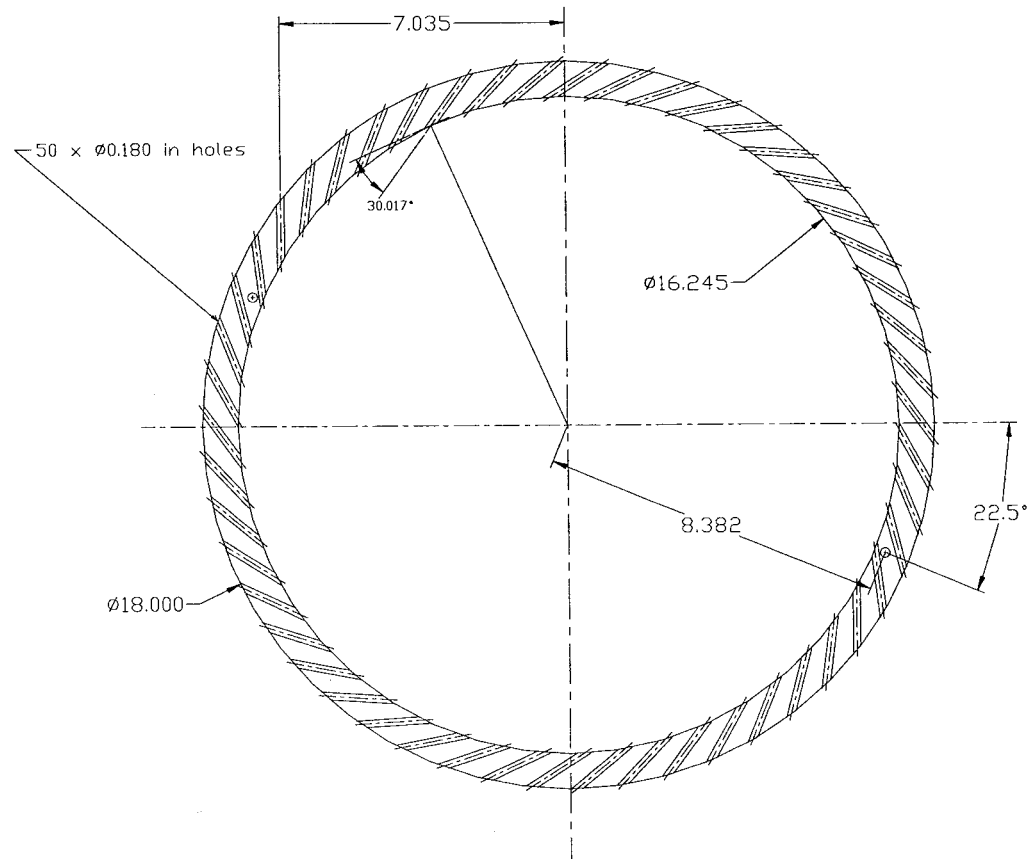


Figure 2.8 – Vortex Ring for Inflow (Sink)

2.2.5 Flow Measurement

A schematic of the rotameter used is shown in figure 2.9. It consists of a float and a tapered tube, in which the float is free to move. As the fluid (air) enters at the bottom of the vertical tube, the float (or bob) rises, and the area between the float and the tube

increases. The float then assumes a position in the tube where the weight and drag forces are balanced, and its position points to the indication of the flow rate.

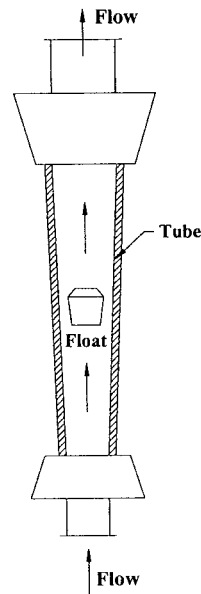


Figure 2.9 – Schematic of a Rotameter

There are a couple of advantages for using a rotameter as opposed to other devices. Firstly, the uniform flow scale over the range of the instrument is ensured, and secondly, the pressure losses are fixed for all flow rates. A pre-operational check and calibration had already been made on the instrument therefore no calibration techniques were applied to the device. The rotameter used was mounted on a wooden support. This ensured a proper position in order for its accuracy and sensitivity to remain unaffected. A calibration scale was attached to the glass tube that reads the volume flow rate in CFM units, with a maximum range of 70 cubic feet per minute.

To prevent damage to the device, the inlet line was initially purged with a high flow rate of air in order to prevent the float from bouncing up and down in the metering tube. Eventually the float was adjusted to the desired flow rate.

2.2.6 Pitot – Static tube

In order to measure the radial velocity, a thin pitot-static tube was inserted into the flowfield. The probe combined both static and stagnation pressure measurements in a single unit. Therefore, the values of the dynamic pressure $P_{\text{Total}} - P_{\text{Static}}$ were obtained directly, and the local velocities were calculated. The pitot-static tube was attached to the aluminum bar through a micrometer mechanism (figure 2.10) that controlled its vertical movement.

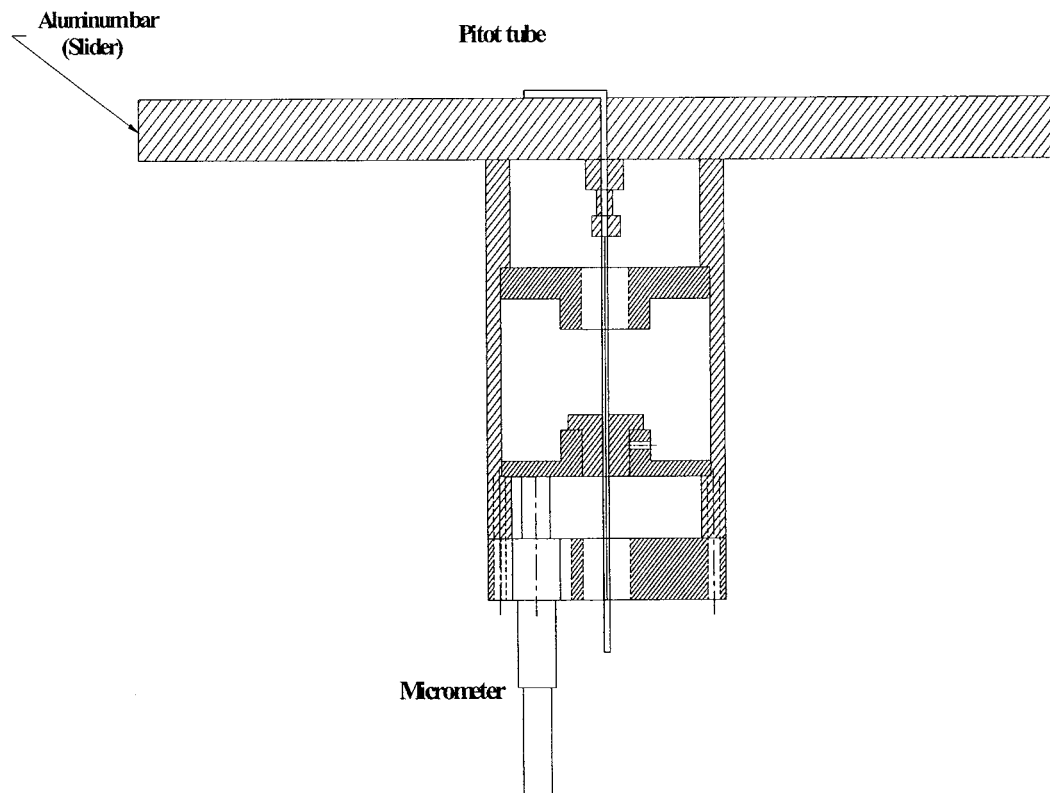


Figure 2.10 – Micrometer assembly

A factor that could have affected the accuracy of the pressure measurements was the misalignment of the pitot-static probe with the flow direction. The angle formed between the probe axis and the local streamline (yaw-angle) had to be zero, otherwise the pitot-static tube being sensitive to the yaw would have produced significant errors.

2.2.7 Inclined Manometers

A precise assembly of inclined manometers that consists of two adjustable manometers of different scale length was used to measure the static pressure as well as the dynamic head measurements. To acquire the static pressures, 10 holes with a diameter of 0.0625 inches, equally spaced, were drilled on the top disc and were arranged at a distance of 0.875 inches across the radius of the disc. The pressure taps were attached with flexible tubes in a control panel, and the outlet was connected to the manometer. The manometer was adjusted and zeroed before any measurement was taken.

2.3 Considerations on experimental analysis, data treatment and errors

For the experimental data to have maximum significance, the measurements should be performed with the utmost degree of accuracy. To achieve that, the limitations of the apparatus should be fully known and understood, and the various types and sources of errors that may occur during the experimentation should be anticipated and dealt with.

[31]

Once the data was collected, a thorough examination followed to establish any inconsistencies. The observations that did not follow the general trend of the overall results were completely eliminated. Subsequently, we examined the results from the existing theory. That way, we ensured that the trend of the results we got was in general consistent with the theory. The latter also provided an idea of how to present the results, and a dimensional analysis was performed (to be discussed later). The assumption concerning the flow axisymmetry was also examined by taking static pressure measurements at the angles of 0 and 180 degrees (with respect to the discs' centreline). This check revealed that flow is axisymmetric, within 8-10 % of uncertainty.

Types and sources of errors that may be the source of experimental uncertainties can be of equipment, human, or methodology nature. Equipment errors can result from inaccuracies in the design, maintenance, and manufacturing, as well as calibration, and sensitivity changes. During the experimentation, the positioning of a pitot-static probe in the flow might have caused some disturbance in the flow conditions. Also, because its inner diameter was so small, it could have been blocked or the yaw angle could have been different from zero, therefore affecting the results. Care was taken to ensure that the yaw angle was zero, and that the pitot - tube was aligned with the flow. A preliminary check was performed to ensure that the probe was not blocked. Some errors could have been imposed due to instabilities in the flow from the pressurized air, or the blower that caused the float in the rotameter to slightly oscillate. In these cases, care was taken to adjust the flow at a constant rate, and the measurements were interrupted when it was not feasible to do so.

Chapter III

Analytical Development Of The Problem

3.1 Dimensional Analysis

In order to reduce the experimental effort, and to present our results in a generalized form, we performed dimensional analysis. The flow is assumed to take place within the small gap ($h/R_{in} \ll 1$), formed by two discs placed one on top of the other. The region of our focus is sufficiently far from the inlet for the source flow and from the outlet for the sink flow. The theoretical analysis applies for negligible tangential and axial velocity components, thus only the radial velocity is considered. Furthermore, for the case of the source flow the analytical model does not apply in the vicinity where the phenomena of the *vena contracta* and flow separation might take place. Under these restrictions, the expected functional relationships for the velocity and pressure are:

$$V_r = fn\{V_{rin}, \rho, \mu, r, z, R_{in}, h\}$$

and

$$\Delta p = fn\{V_{rin}, \rho, \mu, r, R_{in}, h\}$$

where r , z , R_{in} , p_{in} , p , V_{rin} , h , μ , ρ , are the radius, height, inlet radius, inlet static pressure, static pressure at radius r , inlet average radial velocity, half the gap size, viscosity, and the density, respectively. Since we are dealing with small gaps, the axial velocity component is zero, and the pressure is not a function of the height z . Buckingham's π -theorem furnishes the expected functional relations among the main dimensionless parameter:

$$V_r = f\{r, z, \xi, Re\} \quad \text{and} \quad \Delta p = \{r, \xi, Re\}$$

where,

$$\Delta p = \frac{p(r) - p_{in}}{\rho V_{rin}^2}, \quad \xi = \frac{h}{R_{in}}, \quad \eta = \frac{r}{R_{in}}, \quad \zeta = \frac{z}{h}, \quad u = \frac{V_r}{V_{rin}}, \quad Re = \frac{V_{rin} h}{\nu}$$

In the case of small gaps, the Reynolds number can be combined with ξ , thus transforming it into the reduced Reynolds number $Re_r = Re \xi$.

3.2 Statement of the theoretical problem

One case of the problem is represented in the schematic of figure 3.1. For the case of the inflow, the fluid (air) enters from the extreme periphery of the discs and exits through the centrally located exit. The equations will be solved for steady and incompressible flow (both inflow and outflow), and under the assumption that the gap between the discs is very small. Therefore, the ratio $\frac{h}{R_{in}}$ will be $\ll 1$, and the axial

velocity component V_z is also zero since it does not have the space and adequate time to develop.

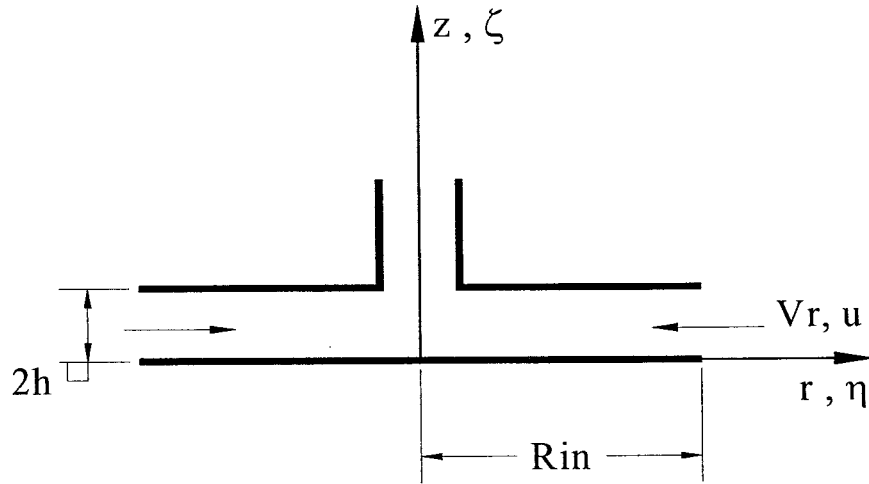


Figure 3. 1 – Schematic of inflow between two discs

Since the discs are closely spaced the flow is assumed to be laminar. In case the flow is turbulent at the entrance, this assumption is still valid, because the flow will accelerate towards a monotonically decreasing pressure therefore it will eventually laminarize. Moreover, since the geometry is symmetric, we assume that the flow is axisymmetric, therefore all changes with respect to θ will be zero ($\frac{\partial}{\partial \theta} = 0$).

3.3 Flow with Swirl

The equations of continuity and momentum are first considered:

Continuity:

$$\frac{1}{r} \frac{\partial}{\partial r}(rV_r) + \underbrace{\frac{1}{r} \frac{\partial}{\partial \theta}(V_\theta)}_{=0, \text{ axisymmetric}} + \underbrace{\frac{\partial}{\partial z}(V_z)}_{=0; V_z=0} = 0 \Rightarrow \frac{1}{r} \frac{\partial}{\partial r}(rV_r) = 0$$

r-momentum:

$$V_r \frac{\partial V_r}{\partial r} - \frac{V_\theta^2}{r} = -\frac{1}{\rho} \frac{\partial p}{\partial r} + \nu \left\{ \underbrace{\frac{\partial}{\partial r} \left[\frac{1}{r} \frac{\partial}{\partial r}(V_r r) \right]}_{=0; \text{ continuity}} + \frac{1}{r} \frac{\partial^2 (V_r r)}{\partial z^2} \right\} \Rightarrow$$

$$V_r \frac{\partial V_r}{\partial r} - \frac{V_\theta^2}{r} = -\frac{1}{\rho} \frac{\partial p}{\partial r} + \nu \left[\frac{1}{r} \frac{\partial^2 (V_r r)}{\partial z^2} \right]$$

θ -momentum:

$$V_r \frac{\partial V_\theta}{\partial r} + \frac{V_r V_\theta}{r} = \nu \left\{ \frac{\partial}{\partial r} \left(\frac{1}{r} \frac{\partial}{\partial r}(rV_\theta) \right) + \frac{\partial^2 V_\theta}{\partial z^2} \right\} \Rightarrow$$

$$V_r \frac{\partial (rV_\theta)}{\partial r} = \nu \left\{ r \frac{\partial}{\partial r} \left[\frac{1}{r} \frac{\partial}{\partial r}(rV_\theta) \right] + r \frac{\partial^2 V_\theta}{\partial z^2} \right\} \Rightarrow$$

$$V_r \frac{\partial(V_\theta r)}{\partial r} = v \left\{ r \frac{\partial}{\partial r} \left[\frac{1}{r} \frac{\partial(V_\theta r)}{\partial r} \right] + \frac{\partial^2(V_\theta r)}{\partial z^2} \right\}$$

z-momentum:

$$\frac{\partial p}{\partial z} = 0 \Rightarrow p \neq fn(z) \Rightarrow p = fn(r) \text{ , only.}$$

The non-dimensional parameters are defined as follows:

$$u = \frac{V_r}{V_{r_{in}}}, \quad v = \frac{V_\theta}{V_{\theta_{in}}}, \quad \eta = \frac{r}{R_{in}}, \quad \zeta = \frac{z}{h}$$

$$\xi = \frac{h}{R_{in}}, \quad s = \frac{V_{\theta_{in}}}{V_{r_{in}}}, \quad \text{Re} = \frac{V_{r_{in}} h}{\nu}$$

$$\text{Re}_r = \xi \text{Re}, \quad \Delta p = \frac{P(r) - P_{in}}{\rho V_{r_{in}}^2}$$

Introducing the above parameters into the continuity, r and θ -momentum equations yield:

Continuity:

$$\Rightarrow \underbrace{\frac{V_{r_{in}}}{R_{in}}}_{\text{constant}} \frac{1}{\eta} \frac{\partial(\eta u)}{\partial \eta} = 0 \Rightarrow \frac{1}{\eta} \frac{\partial(\eta u)}{\partial \eta} = 0 \quad (1)$$

r-momentum:

$$u V_{r_{in}} \frac{\partial(u V_{r_{in}})}{\partial(\eta R_{in})} - \frac{(v V_{\theta_{in}})^2}{\eta R_{in}} = -\frac{1}{\rho} \frac{\partial(p(r) - p_{in})}{\partial(\eta R_{in})} + v \left\{ \frac{1}{\eta R_{in}} \frac{\partial^2(u V_{r_{in}} \eta R_{in})}{\partial(\zeta h)^2} \right\} \Rightarrow$$

$$u \frac{\partial u}{\partial \eta} - s^2 \frac{v^2}{\eta} = -\frac{d(\Delta p)}{d\eta} + \frac{1}{\text{Re}_r} \left\{ \frac{1}{\eta} \frac{\partial^2(u \eta)}{\partial \zeta^2} \right\} \quad (2)$$

θ -momentum:

$$uV_{r_{in}} \frac{\partial(\eta R_{in} v V_{\theta_{in}})}{\partial(\eta R_{in})} = v \left\{ \eta R_{in} \frac{\partial}{\partial(\eta R_{in})} \left[\frac{1}{\eta R_{in}} \frac{\partial(\eta R_{in} v V_{\theta_{in}})}{\partial(\eta R_{in})} \right] + \frac{\partial^2(\eta R_{in} v V_{\theta_{in}})}{\partial(\zeta h)^2} \right\} \Rightarrow$$

$$\frac{u \partial(\eta v)}{\partial \eta} = \frac{1}{\text{Re}_r} \frac{\partial^2(\eta v)}{\partial \zeta^2} \quad (3)$$

Summarize the non-dimensional equations of continuity and r & θ momentum:

$$\frac{1}{\eta} \frac{\partial(\eta u)}{\partial \eta} = 0 \quad (1)$$

$$u \frac{\partial u}{\partial \eta} - s^2 \frac{v^2}{\eta} = - \frac{d(\Delta p)}{d\eta} + \frac{1}{\text{Re}_r} \left\{ \frac{1}{\eta} \frac{\partial^2(u\eta)}{\partial \zeta^2} \right\} \quad (2)$$

$$\frac{u \partial(v\eta)}{\partial \eta} = \frac{1}{\text{Re}_r} \frac{\partial^2(v\eta)}{\partial \zeta^2} \quad (3)$$

3.3.1 Inflow and Swirl

A schematic of the coordinate system for the case of inflow and swirl is shown in figure 3.2.

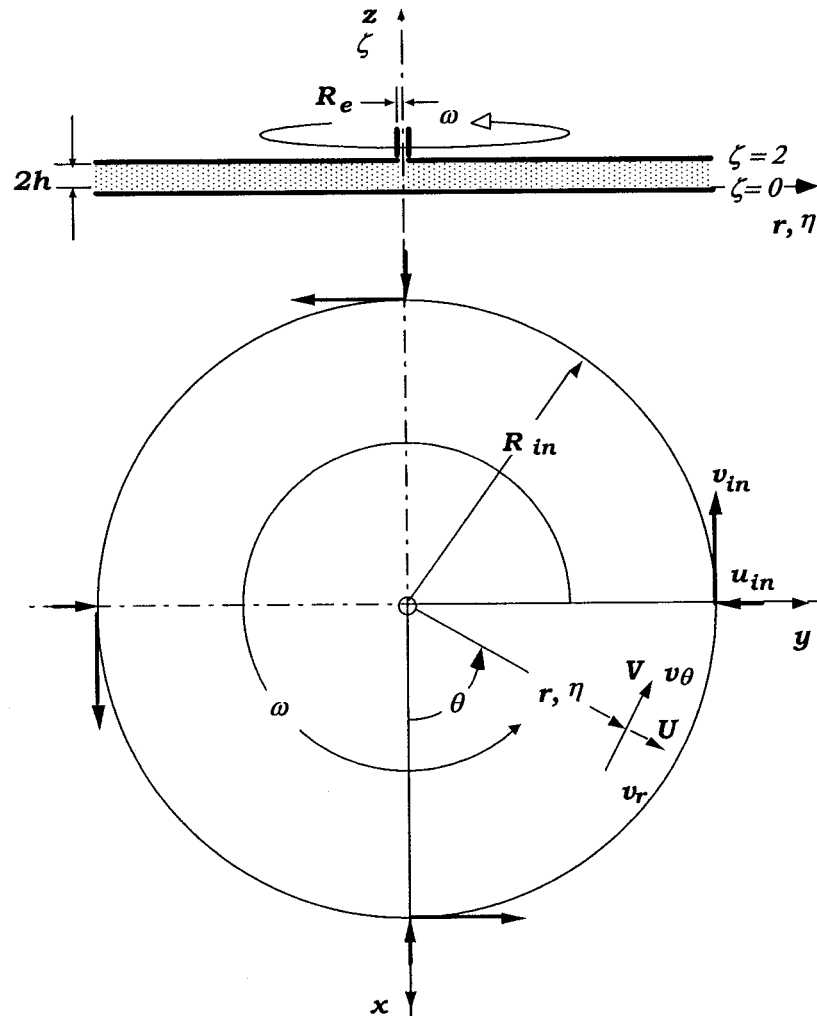


Figure 3.2 – Schematic of coordinate system for inflow with swirl

To solve for the radial velocity, first consider the continuity equation (eq.1).

$$\frac{1}{\eta} \frac{\partial(u\eta)}{\partial\eta} = 0 \Rightarrow \frac{\partial(u\eta)}{\partial\eta} = 0. \text{ Therefore } u\eta \text{ will only be a function of } \zeta.$$

$$\text{Thus: } u = \frac{\Phi(\zeta)}{\eta} \quad (4)$$

To linearize the r-momentum (eq.2)

$$u \frac{\partial u}{\partial \eta} - s^2 \frac{v^2}{\eta} = -\frac{d(\Delta p)}{d\eta} + \frac{1}{\text{Re}_r} \left\{ \frac{1}{\eta} \frac{\partial^2(u\eta)}{\partial \zeta^2} \right\}$$

$$\text{we use } u \cong -\frac{1}{\eta} \text{ and } \frac{\partial u}{\partial \eta} = -\frac{1}{\eta^2} \Phi(\zeta)$$

Inserting the above into the r - momentum it yields :

$$\left(-\frac{1}{\eta} \right) \left(-\frac{1}{\eta^2} \right) \Phi(\zeta) - s^2 \frac{v^2}{\eta} = -\frac{d(\Delta p)}{d\eta} + \frac{1}{\eta \text{Re}_r} \frac{\partial^2 \Phi(\zeta)}{\partial \zeta^2} \quad (5)$$

The maximum value of the centrifugal force occurs at the mid-channel location, therefore

$v^2 \rightarrow v_{\max}^2$. Then the above equation transforms into:

$$\left(-\frac{1}{\eta} \right) \left(-\frac{1}{\eta^2} \right) \Phi(\zeta) - s^2 \frac{v_{\max}^2(\eta)}{\eta} = -\frac{d(\Delta p)}{d\eta} + \frac{1}{\eta \text{Re}_r} \frac{d^2 \Phi(\zeta)}{d\zeta^2} \Rightarrow$$

If we integrate with respect to η , from $\eta = 1$ to η , we obtain from eq.(6):

$$\left(\int_1^\eta \frac{1}{\eta^3} d\eta \right) \Phi(\zeta) - s^2 \int_1^\eta \frac{v_{\max}^2(\eta)}{\eta} d\eta = - \int_1^\eta \frac{d(\Delta p)}{d\eta} d\eta + \frac{1}{\text{Re}_r} \frac{d^2 \Phi(\zeta)}{d\zeta^2} \int_1^\eta \frac{1}{\eta} d\eta \Rightarrow$$

$$\frac{d^2\Phi(\zeta)}{d\zeta^2} - \underbrace{\frac{\text{Re}_r}{\ln(\eta)} \frac{(\eta^2 - 1)}{2\eta^2}}_{=\lambda^2} \Phi(\zeta) = \frac{\text{Re}_r}{\ln(\eta)} \Delta p(\eta) - s^2 \frac{\text{Re}_r}{\ln(\eta)} \int_1^\eta \frac{v_{\max}^2(\eta)}{\eta} d\eta \Rightarrow$$

$$\frac{d^2\Phi(\zeta)}{d\zeta^2} - \lambda^2 \Phi(\zeta) = \lambda^2 \left\{ \underbrace{\left(\frac{2\eta^2}{(\eta^2 - 1)} \right) \Delta p(\eta)}_{=\Delta\Pi(\eta)} - \underbrace{\frac{2s^2\eta^2}{(\eta^2 - 1)} \int_1^\eta \frac{v_{\max}^2(\eta)}{\eta} d\eta}_{=\Delta\Xi(\eta)} \right\} \Rightarrow$$

$$\frac{d^2\Phi(\zeta)}{d\zeta^2} - \lambda^2 \Phi(\zeta) = \lambda^2 \Delta\Xi(\eta) \quad (7)$$

Equation (7) is a second order non-homogeneous ordinary differential equation, where the parameters λ^2 , $\Delta\Pi(\eta)$ and $\Delta\Xi(\eta)$ are represented by the following equations:

$$\lambda^2 = \frac{(\eta^2 - 1)\text{Re}_r}{2\eta^2 \ln(\eta)}, \quad \Delta\Pi(\eta) = \frac{2\eta^2}{(\eta^2 - 1)} \Delta p(\eta), \quad \Delta\Xi(\eta) = \Delta\Pi(\eta) - \frac{2s^2\eta^2}{(\eta^2 - 1)} \int_1^\eta \frac{v_{\max}^2(\eta)}{\eta} d\eta \quad (8)$$

To solve the differential equation (eq.7), the homogeneous and particular solutions must be considered. Therefore: $\Phi(\zeta) = \Phi(\zeta)_h + \Phi(\zeta)_p$

If $\Phi(\zeta)_p = g\lambda^2 \Delta\Xi(\eta)$ and $\Phi(\zeta)_h = Ae^{\lambda\zeta} + Be^{-\lambda\zeta}$, where g, A, and B are constants

then $\Phi(\zeta)$ becomes :

$$\Phi(\zeta) = Ae^{\lambda\zeta} + Be^{-\lambda\zeta} - \Delta\Xi(\eta) = u\eta \quad (9)$$

The evaluation of A and B general constants is achieved via the two boundary conditions:

$$(i) \ z = 0 \ , \ V_r = 0 \quad \Rightarrow \quad \zeta = 0 \quad \text{then} \quad u = 0$$

$$(ii) \ z = 2h \ , \ V_r = 0 \quad \Rightarrow \quad \zeta = 2 \quad \text{then} \quad u = 0$$

If we insert the boundary conditions into equation (9) we obtain the following expressions:

$$(i) \ \zeta = 0 \quad u = 0 \quad \stackrel{(9)}{\Rightarrow} \quad A = \Delta\Xi(\eta) - B \quad (10 \ a)$$

$$(ii) \ \zeta = 2 \quad u = 0 \quad \stackrel{(9)}{\Rightarrow} \quad Ae^{2\lambda} + Be^{-2\lambda} - \Delta\Xi(\eta) = 0 \quad (10 \ b)$$

By substitution of eq.(10 a) into eq.(10 b) constant A is eliminated

therefore B is found to be :

$$B = \Delta\Xi(\eta) \frac{1 - e^{2\lambda}}{e^{-2\lambda} - e^{2\lambda}} \quad (11 \ a)$$

therefore the constant A is given by :

$$A = \Delta\Xi(\eta) \left[1 - \frac{1 - e^{2\lambda}}{e^{-2\lambda} - e^{2\lambda}} \right] \quad (11 \ b)$$

Back substitution of A and B into equation (9) yields:

$$\begin{aligned}
\Phi(\zeta) &= Ae^{\lambda\zeta} + Be^{-\lambda\zeta} - \Delta\Xi(\eta) = \Delta\Xi(\eta) \left[1 - \frac{1 - e^{2\lambda}}{e^{-2\lambda} - e^{2\lambda}} \right] e^{\lambda\zeta} + \Delta\Xi(\eta) \left[\frac{1 - e^{2\lambda}}{e^{-2\lambda} - e^{2\lambda}} \right] e^{-\lambda\zeta} - \Delta\Xi(\eta) \\
&= \Delta\Xi(\eta) \left\{ \frac{e^{\lambda(\zeta-2)} - e^{-\lambda(\zeta-2)}}{2 \frac{e^{-2\lambda} - e^{2\lambda}}{2}} + \frac{e^{\lambda\zeta} - e^{-\lambda\zeta}}{2 \frac{e^{2\lambda} - e^{-2\lambda}}{2}} - 1 \right\} = \Delta\Xi(\eta) \left\{ -\frac{\sinh[\lambda(\zeta-2)]}{\sinh[2\lambda]} + \frac{\sinh[\lambda\zeta]}{\sinh[2\lambda]} - 1 \right\} \\
\Phi(\zeta) &= \Delta\Xi(\eta) \left\{ \frac{\sinh[\lambda(2-\zeta)] + \sinh[\lambda\zeta]}{\sinh[2\lambda]} - 1 \right\} \tag{12}
\end{aligned}$$

From global continuity, we have:

$$\int_0^{2h} V_r(2\pi r) dz = \underbrace{-}_{Inflow} V_{rin}(2\pi r R_{in})(2h) \Rightarrow \int_0^2 \Phi(\zeta) d\zeta = -2 \Rightarrow$$

$$\int_0^2 \Delta\Xi(\eta) \left\{ \frac{\sinh[\lambda(2-\zeta)] + \sinh[\lambda\zeta]}{\sinh[2\lambda]} - 1 \right\} d\zeta = -2 \Rightarrow$$

$$\Delta\Xi(\eta) = \frac{-2}{\int_0^2 \left\{ \frac{\sinh[\lambda(2-\zeta)] + \sinh[\lambda\zeta]}{\sinh[2\lambda]} - 1 \right\} d\zeta}$$

$$\Delta\Xi(\eta) = \frac{-2}{\int_0^2 \frac{\sinh[\lambda(2-\zeta)]}{\sinh(2\lambda)} d\zeta + \int_0^2 \frac{\sinh(\lambda\zeta)}{\sinh(2\lambda)} d\zeta - \int_0^2 d\zeta} \Rightarrow$$

$$\Delta\Xi(\eta) = \frac{\lambda \sinh(2\lambda)}{\lambda \sinh(2\lambda) - \cosh(2\lambda) + 1} \quad (13)$$

Introducing $\Delta\Xi(\eta)$ from eq.(13) into eq. (12), $\Phi(\zeta)$ transforms to :

$$\Phi(\zeta) = \frac{\lambda \sinh(2\lambda)}{\lambda \sinh(2\lambda) - \cosh(2\lambda) + 1} \left\{ \frac{\sinh[\lambda(2-\zeta)] + \sinh(\lambda\zeta)}{\sinh(2\lambda)} - 1 \right\} \quad (14)$$

where $u = \frac{\Phi(\zeta)}{\eta}$

The radial velocity for Inflow and Swirl is given by :

$$u = \frac{1}{\eta} \frac{\lambda \sinh(2\lambda)}{\lambda \sinh(2\lambda) - \cosh(2\lambda) + 1} \left\{ \frac{\sinh[\lambda(2-\zeta)] + \sinh(\lambda\zeta)}{\sinh(2\lambda)} - 1 \right\} \quad (15)$$

In order to determine the tangential velocity component, the θ - momentum must be considered (eq.3). Linearizing the inertia terms and applying separation of variables, by letting $v\eta = \phi(\eta)\psi(\zeta)$ the θ - momentum becomes:

$$\frac{1}{\eta} \frac{1}{\phi(\eta)} \frac{d\phi(\eta)}{d\eta} = -\frac{1}{\text{Re}_r} \frac{1}{\psi(\zeta)} \frac{d^2\psi(\zeta)}{d\zeta^2} = \beta^2 \quad (16)$$

where β is the separation constant

The resulting differential equations from (16) will be solved to give :

$$\begin{aligned} \frac{1}{\eta} \frac{1}{\phi(\eta)} \frac{d\phi(\eta)}{d\eta} = \beta^2 &\Rightarrow \int \frac{d\phi(\eta)}{\phi(\eta)} = \int \beta^2 \eta d\eta \\ \phi(\eta) &= k e^{\frac{\beta^2 \eta^2}{2}}, \quad k \text{ is a constant} \end{aligned} \quad (17 \text{ a})$$

$$-\frac{1}{\text{Re}_r} \frac{1}{\psi(\zeta)} \frac{d^2\psi(\zeta)}{d\zeta^2} = \beta^2 \Rightarrow \frac{d^2\psi(\zeta)}{d\zeta^2} + \beta^2 \text{Re}_r \psi(\zeta) = 0 \quad (17 \text{ b})$$

The differential equation described in (17 b) has complex solutions :

$$\psi(\zeta) = A \cos(\beta \sqrt{\text{Re}_r} \zeta) + B \sin(\beta \sqrt{\text{Re}_r} \zeta) \quad (18)$$

where A, B are constants

Since $v\eta = \phi(\eta)\psi(\zeta)$, then :

$$\begin{aligned} \stackrel{(17a), (18)}{\Rightarrow} v\eta &= k e^{\frac{\beta^2 \eta^2}{2}} \left[A \cos(\beta \sqrt{\text{Re}_r} \zeta) + B \sin(\beta \sqrt{\text{Re}_r} \zeta) \right] \\ &= e^{\frac{\beta^2 \eta^2}{2}} \left[A' \cos(\beta \sqrt{\text{Re}_r} \zeta) + B' \sin(\beta \sqrt{\text{Re}_r} \zeta) \right] \end{aligned}$$

where $A' = kA$ and $B' = kB$

$$v\eta = \left\{ A' \cos(\beta \sqrt{\text{Re}_r} \zeta) + B' \sin(\beta \sqrt{\text{Re}_r} \zeta) \right\} e^{\frac{\beta^2 \eta^2}{2}} \quad (19)$$

In order to determine the constants in equation (19), we apply the boundary conditions:

(i) $z = 0$ or $\zeta = 0$ then $v = 0$

(ii) $z = h$ or $\zeta = 1$ then $\frac{dv}{d\zeta} = 0$ (maximum velocity at the centerline)

Applying (i) and (ii) into eq.(19) the following is obtained:

$$(i) \text{ at } \zeta = 0 \quad v = 0 \xrightarrow{(19)} v\eta = 0 \Rightarrow A' = 0 \quad (20 a)$$

$$(ii) \text{ at } \zeta = 1 \quad \frac{dv}{d\zeta} = 0 \xrightarrow{(19)} \frac{d}{d\zeta} \left[B' \sin(\beta \sqrt{\text{Re}_r} \zeta) \right]_{\zeta=1} = 0 \quad [\text{Since } A' = 0 \text{ and } e^{\frac{\beta^2 \eta^2}{2}} \text{ are constants}]$$

$$\Rightarrow B' \beta \sqrt{\text{Re}_r} \cos(\beta \sqrt{\text{Re}_r}) = 0 \quad (20 b)$$

Since $\beta \sqrt{\text{Re}_r}$ is a constant and B' must be different from zero in order for equation (19) to be valid,

it must be: $\cos(\beta \sqrt{\text{Re}_r}) = 0$. Cosine becomes zero at $\frac{2n+1}{2} \pi$, so:

$$\cos(\beta \sqrt{\text{Re}_r}) = \cos\left(\frac{2n+1}{2} \pi\right) = 0 \Rightarrow \beta \sqrt{\text{Re}_r} = \frac{2n+1}{2} \pi \Rightarrow \beta = \frac{2n+1}{2\sqrt{\text{Re}_r}} \pi \quad (21 a)$$

Let $\beta = \beta_n$ (β varies with n)

$$\text{So,} \quad \beta_n = \frac{2n+1}{2\sqrt{\text{Re}_r}} \pi \quad (21 b)$$

Substitution of β_n back to equation (19), $v\eta$ becomes :

$$v\eta = \sum_{n=0}^{\infty} B_n e^{\frac{\beta_n^2 \eta^2}{2}} \sin\left(\frac{2n+1}{2} \pi \zeta\right) = \varphi \psi \quad (22)$$

where B' is being replaced by B_n since B' will vary with n . Therefore, eq.(22)

transforms into :

$$v = \frac{\varphi \psi}{\eta} = \sum_{n=0}^{\infty} B_n \frac{e^{\frac{\beta_n^2 \eta^2}{2}}}{\eta} \sin\left(\frac{2n+1}{2} \pi \zeta\right) \quad (23)$$

Application of the initial condition ($\eta = 1 \Rightarrow v = 1.0$) in equation (23) provides:

$$1 = \sum_{n=0}^{\infty} B_n e^{\frac{\beta_n^2}{2}} \sin\left(\frac{2n+1}{2} \pi \zeta\right) \quad (24 \text{ a})$$

$$\text{Letting } E_n = B_n e^{\frac{\beta_n^2}{2}} \quad (24 \text{ b})$$

then eq.(24 a) becomes :

$$1 = \sum_{n=0}^{\infty} E_n \sin\left(\frac{2n+1}{2} \pi\right) \quad (24 \text{ c})$$

E_n must be expressed so that it becomes the Fourier sine series of v .

$$E_n = \frac{2}{L} \int_0^L v(\zeta) \sin\left(\frac{n\pi}{L} \zeta\right) d\zeta = -\frac{1}{\frac{(2n+1)}{2} \pi} \left[\cos\left(\frac{(2n+1)}{2} \pi\right) \right]_0^2 = \frac{4}{(2n+1)\pi} \quad (24 \text{ d})$$

$$E_n = B_n e^{\frac{\beta_n^2}{2}} = \frac{4}{(2n+1)\pi} \Rightarrow B_n = \frac{4}{(2n+1)\pi} e^{-\frac{\beta_n^2}{2}} \quad (24 \text{ e})$$

Since : $\beta_n = \frac{2n+1}{2\sqrt{\text{Re}_r}} \pi$ (eq.21 b), thus B_n becomes :

$$B_n = \frac{4}{(2n+1)\pi} e^{\frac{-\left(\frac{2n+1}{2\sqrt{\text{Re}_r}} \pi\right)^2}{2}} \Rightarrow B_n = \frac{4}{(2n+1)\pi} e^{-\left\{\frac{(2n+1)^2 \pi^2}{8 \text{Re}_r}\right\}} \quad (25)$$

Once B_n has been determined, substitute back to eq.(23) in order to obtain the tangential velocity v :

$$v = \sum_{n=0}^{\infty} \frac{4}{(2n+1)\pi} e^{-\frac{\beta_n^2}{2}} e^{\frac{\beta_n^2 \eta^2}{2}} \frac{1}{\eta} \sin\left(\frac{2n+1}{2} \pi \zeta\right) \Rightarrow$$

$$v = \sum_{n=0}^{\infty} \frac{4}{(2n+1)\pi} e^{\left\{\frac{(2n+1)^2 \pi^2}{8 \text{Re}_r} (\eta^2 - 1)\right\}} \frac{1}{\eta} \sin\left(\frac{2n+1}{2} \pi \zeta\right) \quad (26)$$

The maximum v occurs at the centerline where $\zeta = 1$. Therefore from equation (26) we have :

$$v_{\max} = \sum_{n=0}^{\infty} \frac{4(-1)^n}{(2n+1)\pi} \frac{1}{\eta} e^{\left\{\frac{(2n+1)^2 \pi^2}{8 \text{Re}_r} (\eta^2 - 1)\right\}} \quad (27)$$

Since v_{\max} was defined, $\Delta\Xi(\eta)$ can be calculated.

It was found previously (eq.13) that the pressure $\Delta\Xi(\eta)$ is equal to :

$$\Delta\Xi(\eta) \stackrel{(13)}{=} \frac{\lambda \sinh(2\lambda)}{\lambda \sinh(2\lambda) - \cosh(2\lambda) + 1} \stackrel{(8)}{=} \Delta\Pi(\eta) - \frac{2s^2 \eta^2}{(\eta^2 - 1)} \int_1^{\eta} \frac{v_{\max}^2(\eta)}{\eta} d\eta \Rightarrow$$

$$\Delta\Pi(\eta) = \frac{\lambda \sinh(2\lambda)}{\lambda \sinh(2\lambda) - \cosh(2\lambda) + 1} + \frac{2s^2 \eta^2}{(\eta^2 - 1)} \int_1^{\eta} \frac{v_{\max}^2(\eta)}{\eta} d\eta \quad (28)$$

from equation (27) the maximum tangential velocity was expressed as :

$$v_{\max} = \sum_{n=0}^{\infty} \frac{4(-1)^n}{(2n+1)\pi} \frac{1}{\eta} e^{\left\{\frac{(2n+1)^2 \pi^2}{8 \text{Re}_r} (\eta^2 - 1)\right\}} = \sum_{n=0}^{\infty} \frac{4(-1)^n}{(2n+1)\pi} \frac{1}{\eta} e^{\left\{-\frac{\beta_n^2}{2} (1 - \eta^2)\right\}}$$

In order to evaluate $\Delta\Pi(\eta)$, the integral $\int_1^{\eta} \frac{v_{\max}^2(\eta)}{\eta} d\eta$ must be solved first.

Using the property $\left(\sum_{i=0}^n x_i\right)^2 = \sum_{j=0}^n \sum_{k=0}^n x_j x_k$, v_{\max}^2 becomes:

$$v_{\max}^2 = \sum_{n=0}^{\infty} \sum_{m=0}^{\infty} \frac{16(-1)^n (-1)^m}{(2n+1)(2m+1)\pi^2} \frac{1}{\eta^2} \exp\left\{-\frac{\beta_n^2}{2}(1-\eta^2) - \frac{\beta_m^2}{2}(1-\eta^2)\right\} \quad (29 \text{ a})$$

Therefore the $\int_1^{\eta} \frac{v_{\max}^2(\eta)}{\eta} d\eta$ becomes :

$$\int_1^{\eta} \frac{v_{\max}^2(\eta)}{\eta} d\eta = \sum_{n=0}^{\infty} \sum_{m=0}^{\infty} \frac{16(-1)^{n+m}}{(2n+1)(2m+1)\pi^2} \underbrace{\int_1^{\eta} \frac{1}{\eta^3} \exp\left\{-\frac{(\beta_n^2 + \beta_m^2)}{2}(1-\eta^2)\right\} d\eta}_{(29 \text{ b})}$$

If $\alpha = \frac{(\beta_n^2 + \beta_m^2)}{2}$, then the integral becomes :

$$\int_1^{\eta} \frac{1}{\eta^3} e^{-\alpha(1-\eta^2)} d\eta = e^{-\alpha} \int_1^{\eta} \frac{1}{\eta^3} e^{\alpha\eta^2} d\eta \quad (29 \text{ c})$$

By changing the variables from η^2 to δ and by letting $\eta^2 = \delta$ then $d\delta = 2\eta d\eta \Leftrightarrow d\eta = \frac{d\delta}{2\eta}$

$$\text{From eq.(29 c): } \int_1^{\eta} \frac{1}{\eta^3} e^{-\alpha(1-\eta^2)} d\eta = \frac{e^{-\alpha}}{2} \int_1^{\eta} \frac{e^{\alpha\delta}}{\delta^2} d\delta \quad (29 \text{ d})$$

Finally by solving $\frac{e^{-\alpha}}{2} \int_1^{\eta} \frac{e^{\alpha\delta}}{\delta^2} d\delta$ we obtain:

$$\frac{e^{-\alpha}}{2} \int_1^\eta \frac{e^{\alpha\delta}}{\delta^2} d\delta = \frac{1}{2} \left\{ 1 - \frac{e^{-\alpha(1-\eta^2)}}{\eta^2} + \alpha e^{-\alpha} \left[\ln(\eta^2) + \sum_{k=1}^{\infty} \frac{\alpha^k}{k \cdot k!} (\eta^{2k} - 1) \right] \right\} \quad (29 \text{ e})$$

Substitute the above expression into the integral $\int \frac{v_{\max}^2(\eta)}{\eta}$, to obtain the final equation for the

pressure $\Delta\Pi(\eta)$. Therefore from equation (29 b) we have that :

$$\begin{aligned} \text{eq. (29 b)} \Rightarrow \int \frac{v_{\max}^2(\eta)}{\eta} d\eta &= \sum_{n=0}^{\infty} \sum_{m=0}^{\infty} \frac{16(-1)^{n+m}}{(2n+1)(2m+1)\pi^2} \int \frac{1}{\eta^3} \exp\left\{-\frac{(\beta_n^2 + \beta_m^2)}{2} (1-\eta^2)\right\} d\eta \Rightarrow \\ \int \frac{v_{\max}^2(\eta)}{\eta} d\eta &= \sum_{n=0}^{\infty} \sum_{m=0}^{\infty} \frac{16(-1)^{n+m}}{(2n+1)(2m+1)\pi^2} \frac{1}{2} \left\{ 1 - \frac{e^{-\alpha(1-\eta^2)}}{\eta^2} + \alpha e^{-\alpha} \left[\ln(\eta^2) + \sum_{k=1}^{\infty} \frac{\alpha^k}{k \cdot k!} (\eta^{2k} - 1) \right] \right\} \end{aligned}$$

Therefore the pressure $\Delta\Pi(\eta)$ (eq.28) becomes :

$$\begin{aligned} \Delta\Pi(\eta) &= \frac{\lambda \sinh(2\lambda)}{\lambda \sinh(2\lambda) - \cosh(2\lambda) + 1} + \\ &+ \frac{16s^2\eta^2}{(\eta^2 - 1)\pi^2} \sum_{n=0}^{\infty} \sum_{m=0}^{\infty} \frac{(-1)^{n+m}}{(2n+1)(2m+1)} \left\{ 1 - \frac{e^{-\alpha(1-\eta^2)}}{\eta^2} + \right. \\ &\left. \alpha e^{-\alpha} \left[\ln(\eta^2) + \sum_{k=1}^{\infty} \frac{\alpha^k}{k \cdot k!} (\eta^{2k} - 1) \right] \right\} \end{aligned} \quad (30)$$

$$\text{where, } \alpha = \frac{(\beta_n^2 + \beta_m^2)}{2} = \frac{1}{2} \left[\frac{(2n+1)\pi}{2\sqrt{\text{Re}_r}} \right]^2 + \frac{1}{2} \left[\frac{(2m+1)\pi}{2\sqrt{\text{Re}_r}} \right]^2 \Rightarrow \alpha = \frac{\pi^2}{8\text{Re}_r} \left[(2n+1)^2 + (2m+1)^2 \right]$$

$$\beta_n = \frac{2n+1}{2\sqrt{\text{Re}_r}} \pi, \quad \lambda = \sqrt{\frac{(\eta^2 - 1)\text{Re}_r}{2\eta^2 \ln(\eta)}}$$

SUMMARY OF EQUATIONS FOUND IN INFLOW AND SWIRL:

Radial Velocity u :

$$u = \frac{1}{\eta} \frac{\lambda \sinh(2\lambda)}{\lambda \sinh(2\lambda) - \cosh(2\lambda) + 1} \left\{ \frac{\sinh[\lambda(2 - \zeta)] + \sinh(\lambda \zeta)}{\sinh(2\lambda)} - 1 \right\}$$

Tangential Velocity v :

$$v = \sum_{n=0}^{\infty} \frac{4}{(2n+1)\pi} e^{\left\{ \frac{(2n+1)^2 \pi^2}{8 \text{Re}_r} (\eta^2 - 1) \right\}} \frac{1}{\eta} \sin\left(\frac{2n+1}{2} \pi \zeta\right)$$

Pressure $\Delta\Pi$:

$$\Delta\Pi(\eta) = \frac{\lambda \sinh(2\lambda)}{\lambda \sinh(2\lambda) - \cosh(2\lambda) + 1} + \frac{16s^2 \eta^2}{(\eta^2 - 1)\pi^2} \sum_{n=0}^{\infty} \sum_{m=0}^{\infty} \frac{(-1)^{n+m}}{(2n+1)(2m+1)} \left\{ 1 - \frac{e^{-\alpha(1-\eta^2)}}{\eta^2} + \alpha e^{-\alpha} \left[\ln(\eta^2) + \sum_{k=1}^{\infty} \frac{\alpha^k}{k \cdot k!} (\eta^{2k} - 1) \right] \right\}$$

Other parameters:

$$\alpha = \frac{\pi^2}{8 \text{Re}_r} \left[(2n+1)^2 + (2m+1)^2 \right]$$

$$\beta_n = \frac{2n+1}{2\sqrt{\text{Re}_r}} \pi$$

$$\lambda = \sqrt{\frac{(\eta^2 - 1)\text{Re}_r}{2\eta^2 \ln(\eta)}}$$

$$\Delta\Pi(\eta) = \left(\frac{2\eta^2}{\eta^2 - 1} \right) \Delta p(\eta)$$

3.3.2 Outflow and Swirl

The same procedure as in paragraph 3.2.1 is followed in order to solve for the case of outflow and swirl. The diagram of the problem for outflow and swirl is shown below. The assumptions are the same as in the previous case.

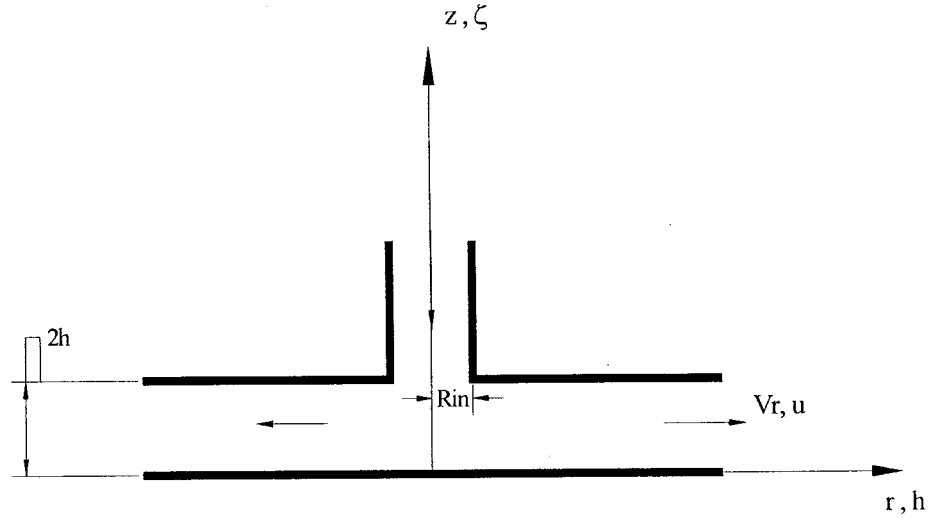


Figure 3.3 – Schematic of Outflow between two discs

For the case of the radial velocity, the equation of continuity was solved and we obtained

that: $u = \frac{\Phi(\zeta)}{\eta}$. Linearizing the r-momentum and letting $\frac{\partial u}{\partial \eta} = -\frac{1}{\eta^2} \Phi(\zeta)$ yields:

$$\stackrel{(2)}{\Rightarrow} u \frac{\partial u}{\partial \eta} - s^2 \frac{v^2}{\eta} = -\frac{d(\Delta p)}{d\eta} + \frac{1}{\text{Re}_r} \left\{ \frac{1}{\eta} \frac{\partial^2 (u\eta)}{\partial \zeta^2} \right\} \Rightarrow$$

$$\left(\frac{1}{\eta} \right) \left(-\frac{1}{\eta^2} \right) \Phi(\zeta) - s^2 \frac{v^2}{\eta} = -\frac{d(\Delta p)}{d\eta} + \frac{1}{\eta \text{Re}_r} \frac{d^2 \Phi(\zeta)}{d\zeta^2} \quad (31)$$

Similarly, as indicated in the previous section, the maximum centrifugal effects are considered. Therefore, at the mid-plane, by letting v^2 with v_{\max}^2 equation (31) results in:

$$\begin{aligned}
\left(\frac{1}{\eta}\right)\left(-\frac{1}{\eta^2}\right)\Phi(\zeta) - s^2 \frac{v_{\max}^2(\eta)}{\eta} &= -\frac{d(\Delta p)}{d\eta} + \frac{1}{\eta \text{Re}_r} \frac{d^2\Phi(\zeta)}{d\zeta^2} \Rightarrow \\
\frac{d^2\Phi(\zeta)}{d\zeta^2} + \underbrace{\frac{\text{Re}_r}{\ln(\eta)} \frac{(\eta^2 - 1)}{2\eta^2}}_{=\lambda^2} \Phi(\zeta) &= \frac{\text{Re}_r}{\ln(\eta)} \Delta p(\eta) - s^2 \frac{\text{Re}_r}{\ln(\eta)} \int_1^\eta \frac{v_{\max}^2(\eta)}{\eta} d\eta \Rightarrow \\
\frac{d^2\Phi(\zeta)}{d\zeta^2} + \lambda^2 \Phi(\zeta) &= \lambda^2 \left\{ \underbrace{\left(\frac{2\eta^2}{(\eta^2 - 1)}\right) \Delta p(\eta)}_{=\Delta\Pi(\eta)} - \frac{2s^2\eta^2}{(\eta^2 - 1)} \int_1^\eta \frac{v_{\max}^2(\eta)}{\eta} d\eta \right\} \Rightarrow \\
\frac{d^2\Phi(\zeta)}{d\zeta^2} + \lambda^2 \Phi(\zeta) &= \lambda^2 \underbrace{\left\{ \Delta\Pi(\eta) - \frac{2s^2\eta^2}{(\eta^2 - 1)} \int_1^\eta \frac{v_{\max}^2(\eta)}{\eta} d\eta \right\}}_{=\Delta\Xi(\eta)} \quad (32)
\end{aligned}$$

$$\frac{d^2\Phi(\zeta)}{d\zeta^2} + \lambda^2 \Phi(\zeta) = \lambda^2 \Delta\Xi(\eta) - \text{second order non-homogeneous differential equation.} \quad (33)$$

where λ^2 , $\Delta\Pi(\eta)$ and $\Delta\Xi(\eta)$ were defined in the previous case (inflow and swirl)

Following the same procedure as in section 3.2.1 for the case of inflow and swirl, the 2nd O.D.E is solved. By combining the particular and the homogeneous solutions, eq.(33) can be written as follows:

$$\begin{aligned}
\Phi(\zeta) &= A \cos(\lambda\zeta) + B \sin(\lambda\zeta) + \Delta\Xi(\eta) = u\eta \Rightarrow \\
A \cos(\lambda\zeta) + B \sin(\lambda\zeta) + \Delta\Xi(\eta) &= u\eta \quad (34)
\end{aligned}$$

Applying the boundary conditions

$$(i) \quad \zeta = 0 \quad \Rightarrow \quad u = 0$$

$$(ii) \quad \zeta = 2 \quad \Rightarrow \quad u = 0$$

equation (34) yields:

$$(i) \quad \zeta = 0 \quad u = 0$$

$$\stackrel{(34)}{\Rightarrow} A \cos(0) + B \sin(0) + \Delta \Xi(\eta) = 0 \Rightarrow A = -\Delta \Xi(\eta) \quad (35 \text{ a})$$

$$(ii) \quad \zeta = 2 \quad u = 0$$

$$\stackrel{(34)}{\Rightarrow} A \cos(2\lambda) + B \sin(2\lambda) + \Delta \Xi(\eta) = 0 \stackrel{(35a)}{\Rightarrow} \\ B = \Delta \Xi(\eta) \frac{\cos(2\lambda) - 1}{\sin(2\lambda)} \quad (35 \text{ b})$$

Substitute the constants A and B from eq.(35 a) and eq.(35 b) back to eq.(34) to get :

$$\stackrel{(34)}{\Rightarrow} \Phi(\zeta) = -\Delta \Xi(\eta) \cos(\lambda \zeta) + \Delta \Xi(\eta) \frac{[\cos(2\lambda) - 1]}{\sin(2\lambda)} \sin(\lambda \zeta) + \Delta \Xi(\eta) \Rightarrow$$

$$= -\Delta \Xi(\eta) \left[\frac{\sin(2\lambda - \lambda \zeta) + \sin(\lambda \zeta)}{\sin(2\lambda)} - 1 \right]$$

$$= \Delta \Xi(\eta) \left[\frac{2\sin(\lambda) \cos[\lambda(1 - \zeta)]}{\sin(2\lambda)} + 1 \right]$$

Therefore,

$$\Phi(\zeta) = \Delta\Xi(\eta) \left[\frac{2\sin(\lambda)\cos[\lambda(1-\zeta)]}{\sin(2\lambda)} + 1 \right] \quad (36)$$

From global continuity (as for the inflow case), we have :

$$\int_0^2 \Phi(\zeta) d\zeta = +2 \Rightarrow$$

$$\int_0^2 \Delta\Xi(\eta) \left\{ \frac{2\sin(\lambda)\cos[\lambda(1-\zeta)]}{\sin(2\lambda)} + 1 \right\} d\zeta = 2 \Rightarrow$$

$$\Delta\Xi(\eta) = \frac{2}{\int_0^2 \left\{ \frac{2\sin(\lambda)\cos[\lambda(1-\zeta)]}{\sin(2\lambda)} + 1 \right\} d\zeta} \quad (37)$$

Solve the integral $\int_0^2 \cos[\lambda(1-\zeta)] d\zeta$ from eqn.(37) by changing variables:

$$\text{Let } \psi = \lambda(1-\zeta)$$

$$\text{Therefore: } \int_0^2 \cos(\psi) \left(\frac{-d\psi}{\lambda} \right) = \frac{-2\sin(\lambda)}{\lambda} \quad (38a)$$

Substituting eqn.(38a) into equation (37), we get the following expression for $\Delta\Xi(\eta)$:

$$\Delta\Xi(\eta) = \frac{2}{\frac{2\sin(\lambda)}{\sin(2\lambda)} \int_0^2 \cos[\lambda(1-\zeta)] d\zeta + \int_0^2 d\zeta} = \frac{2}{\frac{2\sin(\lambda)}{\sin(2\lambda)} \left[\frac{-2\sin(\lambda)}{\lambda} \right] + 2}$$

$$\Delta\Xi(\eta) = \frac{\lambda \sin(2\lambda)}{\lambda \sin(2\lambda) - 2\sin^2(\lambda)} \quad (39)$$

To obtain $\Phi(\zeta)$, substitute equation (39) into equation (36):

$$\Phi(\zeta) = \Delta \Xi(\eta) \left[\frac{2\sin(\lambda)\cos[\lambda(1-\zeta)]}{\sin(2\lambda)} + 1 \right] = \frac{\lambda \sin(2\lambda)}{\lambda \sin(2\lambda) - 2\sin^2(\lambda)} \left[\frac{2\sin(\lambda)\cos[\lambda(1-\zeta)]}{\sin(2\lambda)} + 1 \right]$$

and since $u = \frac{\Phi(\zeta)}{\eta}$ from eqn.(1),

the radial velocity for outflow and swirl is given by :

$$u = \frac{1}{\eta} \frac{\lambda \sin(2\lambda)}{\lambda \sin(2\lambda) - 2\sin^2(\lambda)} \left[\frac{2\sin(\lambda)\cos[\lambda(1-\zeta)]}{\sin(2\lambda)} + 1 \right] \quad (40)$$

The tangential velocity is solved (as in section 3.2.1), when the θ - momentum was considered (eq.3).

Since $v\eta = \varphi(\eta)\psi(\zeta)$ the θ - momentum becomes :

$$\frac{1}{\eta} \frac{1}{\varphi(\eta)} \frac{d\varphi(\eta)}{d\eta} = \frac{1}{\text{Re}_r} \frac{1}{\psi(\zeta)} \frac{d^2\psi(\zeta)}{d\zeta^2} = -\beta^2 = \text{constant} \quad (41)$$

From the two differential equations we get the following:

$$(a) \quad \frac{1}{\eta} \frac{1}{\varphi(\eta)} \frac{d\varphi(\eta)}{d\eta} = -\beta^2 \Rightarrow$$

$$\varphi(\eta) = k e^{\frac{-\beta^2 \eta^2}{2}}, \quad k \text{ is a constant} \quad (42 \text{ a})$$

$$(b) \quad \frac{1}{\text{Re}_r} \frac{1}{\psi(\zeta)} \frac{d^2 \psi(\zeta)}{d\zeta^2} = -\beta^2 \Rightarrow \frac{d^2 \psi(\zeta)}{d\zeta^2} + \beta^2 \text{Re}_r \psi(\zeta) = 0 \quad (42 \text{ b})$$

The solution to the differential eqn.(42 b) is :

$$\psi(\zeta) = A \cos(\beta \sqrt{\text{Re}_r} \zeta) + B \sin(\beta \sqrt{\text{Re}_r} \zeta) \quad (43)$$

where A , B are constants

Since $v\eta = \varphi(\eta)\psi(\zeta)$ then from eq.(43) we get :

$$\left[A' \cos(\beta \sqrt{\text{Re}_r} \zeta) + B' \sin(\beta \sqrt{\text{Re}_r} \zeta) \right] e^{\frac{-\beta^2 \eta^2}{2}} = v\eta \quad (44)$$

where $A' = kA$ and $B' = kB$

Applying the boundary conditions,

$$(i) \quad \zeta = 0 \quad \rightarrow \quad v = 0$$

$$(ii) \quad \zeta = 1 \quad \rightarrow \quad \frac{dv}{d\zeta} = 0$$

equation (44) becomes:

$$(i) \quad \Rightarrow A' = 0 \quad (45 \text{ a})$$

$$(ii) \quad \Rightarrow \cos(\beta \sqrt{\text{Re}_r}) = 0 \Rightarrow \beta_n = \frac{2n+1}{2\sqrt{\text{Re}_r}} \pi \quad [\text{since } \beta \text{ varies with } n, \beta = \beta_n] \quad (45 \text{ b})$$

Substituting β_n back to equation (44), $v\eta$ becomes :

$$v\eta = \sum_{n=0}^{\infty} B_n e^{\frac{-\beta_n^2 \eta^2}{2}} \sin\left(\frac{2n+1}{2} \pi \zeta\right) = \phi\psi \Rightarrow$$

$$v = \frac{\phi\psi}{\eta} = \sum_{n=0}^{\infty} B_n \frac{e^{\frac{-\beta_n^2 \eta^2}{2}}}{\eta} \sin\left(\frac{2n+1}{2} \pi \zeta\right) \quad (46)$$

By applying the initial condition ($\eta = 1$ $v = 1.0$) to equation (46) and

by letting $E_n = B_n e^{\frac{-\beta_n^2}{2}}$, we get :

$$\Rightarrow 1 = \sum_{n=0}^{\infty} E_n \sin\left(\frac{2n+1}{2} \pi\right) \quad (47)$$

If E_n is expressed as the Fourier sine series of v , it is found to be equal to :

$$E_n = \frac{4}{(2n+1)\pi} \quad (48)$$

Then, $E_n = B_n e^{\frac{-\beta_n^2}{2}} \stackrel{(48)}{=} \frac{4}{(2n+1)\pi}$. Since from eq.(21 b) : $\beta_n = \frac{2n+1}{2\sqrt{\text{Re}_r}} \pi$, B_n becomes :

$$B_n = \frac{4}{(2n+1)\pi} e^{\frac{\left(\frac{2n+1}{2\sqrt{\text{Re}_r}} \pi\right)^2}{2}} \Rightarrow B_n = \frac{4}{(2n+1)\pi} e^{\left\{\frac{(2n+1)^2 \pi^2}{8 \text{Re}_r}\right\}} \quad (49)$$

Substituting the constant B_n back to equation (46) the tangential velocity v transforms to :

$$v = \sum_{n=0}^{\infty} \frac{4}{(2n+1)\pi} e^{\frac{\beta_n^2}{2}} e^{-\frac{\beta_n^2 \eta^2}{2}} \frac{1}{\eta} \sin\left(\frac{2n+1}{2} \pi \zeta\right) \Rightarrow$$

$$v = \sum_{n=0}^{\infty} \frac{4}{(2n+1)\pi} e^{-\left\{\frac{(2n+1)^2 \pi^2}{8 \text{Re}_r} (\eta^2 - 1)\right\}} \frac{1}{\eta} \sin\left(\frac{2n+1}{2} \pi \zeta\right) \quad (50)$$

The maximum tangential velocity v occurs at the centerline where $\zeta = 1$.

From equation (50) we obtain :

$$v_{\max} = \sum_{n=0}^{\infty} \frac{4(-1)^n}{(2n+1)\pi} \frac{1}{\eta} e^{-\left\{\frac{(2n+1)^2 \pi^2}{8 \text{Re}_r} (\eta^2 - 1)\right\}} \quad (51)$$

Since v_{\max} is known, the pressure $\Delta\Xi(\eta)$ for the swirling outflow can be calculated.

Therefore,

$$\Delta\Xi(\eta) = \frac{\lambda \sin(2\lambda)}{\lambda \sin(2\lambda) - 2\sin^2(\lambda)} = \Delta\Pi(\eta) - \frac{2s^2\eta^2}{(\eta^2 - 1)} \int_1^\eta \frac{v_{\max}^2(\eta)}{\eta} d\eta \quad (52)$$

and from eqn.(51)

$$v_{\max} = \sum_{n=0}^{\infty} \frac{4(-1)^n}{(2n+1)\pi} \frac{1}{\eta} e^{-\left\{\frac{(2n+1)^2 \pi^2}{8 \text{Re}_r} (\eta^2 - 1)\right\}} = \sum_{n=0}^{\infty} \frac{4(-1)^n}{(2n+1)\pi} \frac{1}{\eta} e^{-\left\{\frac{\beta_n^2}{2} (\eta^2 - 1)\right\}} \Rightarrow$$

$$v_{\max}^2 = \sum_{n=0}^{\infty} \sum_{m=0}^{\infty} \frac{16(-1)^{n+m}}{(2n+1)(2m+1)\pi^2} \frac{1}{\eta^2} \exp\left\{-\frac{(\beta_n^2 + \beta_m^2)}{2} (\eta^2 - 1)\right\} \quad (53)$$

Therefore the $\int_1^\eta \frac{v_{\max}^2(\eta)}{\eta} d\eta$ becomes:

$$\int_1^\eta \frac{v_{\max}^2(\eta)}{\eta} d\eta = \sum_{n=0}^{\infty} \sum_{m=0}^{\infty} \frac{16(-1)^{n+m}}{(2n+1)(2m+1)\pi^2} \underbrace{\int_1^\eta \frac{1}{\eta^3} \exp\left\{-\frac{(\beta_n^2 + \beta_m^2)}{2} (\eta^2 - 1)\right\} d\eta}_{(54)} \quad (54)$$

And by using the same methodology as in the case of inflow and swirl to solve the above integral, we obtain:

$$\begin{aligned} \int_1^\eta \frac{v_{\max}^2(\eta)}{\eta} d\eta &= \sum_{n=0}^{\infty} \sum_{m=0}^{\infty} \frac{16(-1)^{n+m}}{(2n+1)(2m+1)\pi^2} \int_1^\eta \frac{1}{\eta^3} \exp\left\{-\frac{(\beta_n^2 + \beta_m^2)}{2} (\eta^2 - 1)\right\} d\eta = \\ &= \sum_{n=0}^{\infty} \sum_{m=0}^{\infty} \frac{16(-1)^{n+m}}{(2n+1)(2m+1)\pi^2} e^\alpha \int_1^\eta \frac{1}{\eta^3} e^{-\alpha\eta^2} d\eta \end{aligned} \quad (55)$$

Then the integral becomes : $\int_1^\eta \frac{1}{\eta^3} e^{\alpha(\eta^2-1)} d\eta = e^\alpha \int_1^\eta \frac{1}{\eta^3} e^{-\alpha\eta^2} d\eta$ (56 a)

and by change of variables we get :

$$\int_1^\eta \frac{1}{\eta^3} e^{-\alpha\eta^2} d\eta = \frac{1}{2} \left\{ 1 - \frac{e^{\alpha(1-\eta^2)}}{\eta^2} + (-\alpha)e^\alpha \left[\ln(\eta^2) + \sum_{k=1}^\infty \frac{(-\alpha)^k}{k \cdot k!} (\eta^{2k} - 1) \right] \right\} \quad (56 b)$$

or

$$\int_1^\eta \frac{v_{\max}^2(\eta)}{\eta} d\eta = \sum_{n=0}^\infty \sum_{m=0}^\infty \frac{16(-1)^{n+m}}{(2n+1)(2m+1)\pi^2} \frac{1}{2} \left\{ 1 - \frac{e^{\alpha(\eta^2-1)}}{\eta^2} + (-\alpha)e^\alpha \left[\ln(\eta^2) + \sum_{k=1}^\infty \frac{(-\alpha)^k}{k \cdot k!} (\eta^{2k} - 1) \right] \right\} \quad (57)$$

The pressure can be obtained since the integral of $\int_1^\eta \frac{v_{\max}^2(\eta)}{\eta} d\eta$ was evaluated.

Therefore, from eqn(52):

$$\begin{aligned} \Delta\Pi(\eta) &= \frac{\lambda \sin(2\lambda)}{\lambda \sin(2\lambda) - 2\sin^2(\lambda)} + \frac{2s^2\eta^2}{(\eta^2-1)} \int_1^\eta \frac{v_{\max}^2(\eta)}{\eta} d\eta \Rightarrow \\ \Delta\Pi(\eta) &= \frac{\lambda \sin(2\lambda)}{\lambda \sin(2\lambda) - 2\sin^2(\lambda)} + \\ &\quad + \frac{2s^2\eta^2}{(\eta^2-1)} \sum_{n=0}^\infty \sum_{m=0}^\infty \frac{16(-1)^{n+m}}{(2n+1)(2m+1)\pi^2} \frac{1}{2} \left\{ 1 - \frac{e^{\alpha(\eta^2-1)}}{\eta^2} + \right. \\ &\quad \left. (-\alpha)e^\alpha \left[\ln(\eta^2) + \sum_{k=1}^\infty \frac{(-\alpha)^k}{k \cdot k!} (\eta^{2k} - 1) \right] \right\} \end{aligned} \quad (58)$$

SUMMARY OF THE EQUATIONS DERIVED FOR OUTFLOW AND SWIRL:

Radial Velocity u :

$$u = \frac{1}{\eta} \frac{\lambda \sin(2\lambda)}{\lambda \sin(2\lambda) - 2\sin^2(\lambda)} \left[\frac{2\sin(\lambda)\cos[\lambda(1-\zeta)]}{\sin(2\lambda)} + 1 \right]$$

Tangential Velocity v :

$$v = \sum_{n=0}^{\infty} \frac{4}{(2n+1)\pi} e^{-\left\{ \frac{(2n+1)^2 \pi^2}{8 \text{Re}_r} (\eta^2 - 1) \right\}} \frac{1}{\eta} \sin\left(\frac{2n+1}{2} \pi \zeta\right)$$

Pressure $\Delta\Pi$:

$$\Delta\Pi(\eta) = \frac{\lambda \sin(2\lambda)}{\lambda \sin(2\lambda) - 2\sin^2(\lambda)} + \frac{2s^2 \eta^2}{(\eta^2 - 1)} \sum_{n=0}^{\infty} \sum_{m=0}^{\infty} \frac{16(-1)^{n+m}}{(2n+1)(2m+1)\pi^2} \frac{1}{2} \left\{ \begin{aligned} &1 - \frac{e^{\alpha(\eta^2-1)}}{\eta^2} + \\ &(-\alpha)e^{\alpha} \left[\ln(\eta^2) + \sum_{k=1}^{\infty} \frac{(-\alpha)^k}{k \cdot k!} (\eta^{2k} - 1) \right] \end{aligned} \right\}$$

The analytical expressions obtained in this section contain the trigonometric function of sine, whereas the equations derived in the swirling inflow involve the hyperbolic function of sine. Consequently, the sign of the equations change (for a negative angle) in the case of outflow.

3.4 Some Simpler Flow cases

3.4.1 Inflow without swirl

For this particular case, we let $s = 0$ or $V_{\theta in} = 0$. Therefore, the flow is assumed to be pure radial. Then, the r-momentum becomes:

$$u \frac{\partial u}{\partial \eta} = -\frac{d(\Delta p)}{d\eta} + \frac{1}{Re_r} \left\{ \frac{1}{\eta} \frac{\partial^2 (u\eta)}{\partial \zeta^2} \right\} \quad (59)$$

By linearization of the r - momentum equation and substituting $u = \frac{\Phi(\zeta)}{\eta}$ into eq.(59) :

$$\frac{\partial^2 \Phi(\zeta)}{\partial \zeta^2} - \lambda^2 \Phi(\zeta) = \frac{Re_r}{\ln(\eta)} \Delta p(\eta) \quad (60)$$

$$\text{where } \Delta \Pi(\eta) = \frac{Re_r}{\ln(\eta)} \Delta p(\eta) \quad (61)$$

The differential equation becomes :

$$\frac{\partial^2 \Phi(\zeta)}{\partial \zeta^2} - \lambda^2 \Phi(\zeta) = \Delta \Pi(\eta) \quad (62)$$

If we apply the Boundary conditions and global continuity we obtain the same equation for the radial velocity as for the case of the Inflow and Swirl.

$$u = \frac{1}{\eta} \frac{\lambda \sinh(2\lambda)}{\lambda \sinh(2\lambda) - \cosh(2\lambda) + 1} \left\{ \frac{\sinh[\lambda(2 - \zeta)] + \sinh(\lambda\zeta)}{\sinh(2\lambda)} - 1 \right\} \quad (63)$$

where,

$$\lambda = \sqrt{\frac{(\eta^2 - 1) Re_r}{2\eta^2 \ln(\eta)}}, \quad \Delta \Pi(\eta) = \frac{Re_r}{\ln(\eta)} \Delta p(\eta), \quad \Delta \Xi(\eta) = \frac{\Delta \Pi(\eta)}{\lambda^2} \quad (64)$$

Since we assumed purely radial flow, $V_{\theta in} = 0$ and the tangential velocity v will be zero.

The pressure was found to be equal to:

$$\frac{\lambda \sinh(2\lambda)}{\lambda \sinh(2\lambda) - \cosh(2\lambda) + 1} = \frac{\Delta\Pi(\eta)}{\lambda^2} \Rightarrow$$

$$\Delta\Pi(\eta) = \frac{\lambda^3 \sinh(2\lambda)}{\lambda \sinh(2\lambda) - \cosh(2\lambda) + 1} \quad (65)$$

3.4.2 Outflow without swirl

For the case of outflow and purely radial flow the r-momentum becomes:

$$u \frac{\partial u}{\partial \eta} = -\frac{d(\Delta p)}{d\eta} + \frac{1}{\text{Re}_r} \left\{ \frac{1}{\eta} \frac{\partial^2(u\eta)}{\partial \zeta^2} \right\} \Rightarrow \quad (66)$$

$$\frac{\partial^2 \Phi(\zeta)}{\partial \zeta^2} + \lambda^2 \Phi(\zeta) = \frac{\text{Re}_r}{\ln(\eta)} \Delta p(\eta) \quad (67)$$

After solving the differential equation the same equation for the radial velocity was obtained as in the case of the outflow with swirl:

$$u = \frac{1}{\eta} \frac{\lambda \sin(2\lambda)}{\lambda \sin(2\lambda) - 2\sin^2(\lambda)} \left[\frac{2\sin(\lambda) \cos[\lambda(1-\zeta)]}{\sin(2\lambda)} + 1 \right] \quad (68)$$

The pressure was defined as follows:

$$\frac{\lambda \sin(2\lambda)}{\lambda \sin(2\lambda) - 2\sin^2(\lambda)} = \frac{\Delta\Pi(\eta)}{\lambda^2} \Rightarrow$$

$$\Delta\Pi(\eta) = \frac{\lambda^3 \sin(2\lambda)}{\lambda \sin(2\lambda) - 2\sin^2(\lambda)} \quad (69)$$

Chapter IV

Discussion Of The Results

The results to be reported herein have been divided into two main categories; those that pertain to the accelerating (sink-flow), and those that pertain to the decelerating (source) flow. In both cases, the effects of swirl are also included.

4.1 Sink Flow

Admitting the fluid into the gap by the periphery, and allowing it to exit through centrally located outlet(s) produces the accelerating or sink-flow. This kind of fluid motion is characterized by a monotonically decreasing pressure gradient. The stabilizing effect of acceleration assists the flow to remain laminar even at very high inlet Reynolds numbers, or to laminarize when the entering fluid is initially turbulent. Because there is a sustained variation of its velocity, the creeping flow assumption is not valid for the entire domain, even if the fluid has a low Reynolds number at the inlet.

I. Non – Swirling Flow

The present theory presupposes that the flow is unidirectional. There are however two regions in the sink-flow where the previous assumption is not valid. The first is in zone I, shown in Fig. 4.1, located near the inlet of the gap. The other in zone III is situated in the neighborhood of the exit. As the fluid enters the flow-field, it is immediately under the influence of two types of forces. The first strives to transform the inlet uniform velocity in order to accommodate the non-slip condition on the wall (entrance region). The other is its variation due to the monotonic acceleration.

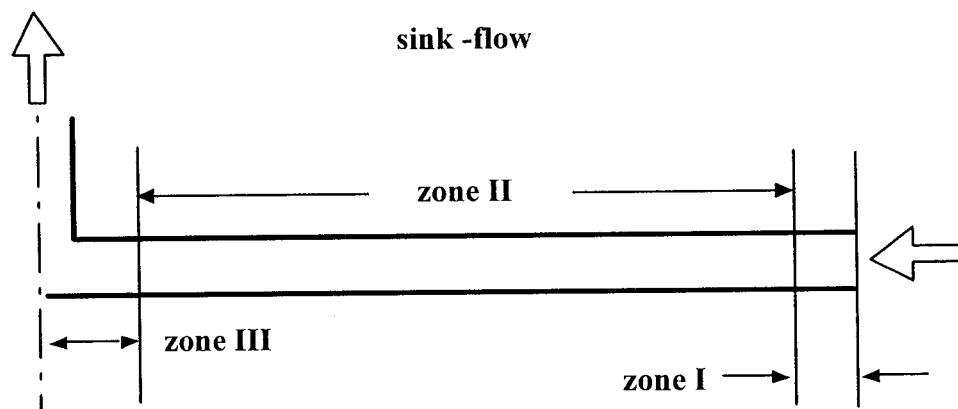


Figure 4.1- Schematic of flow zones

Exploratory calculations using Twaites' method (Appendix B) have shown that for the sink flow, the boundary layer development near the entrance is very quick. As it is evident from Fig. 4.2, the boundary layer displacement thickness increases as the fluid is admitted at the periphery of the discs, and reaches a maximum at about $r = 0.8$. This shows that the entrance effects have already taken place at that radius. From that point

on, the displacement thickness decreases almost linearly as $r \rightarrow 0$. DeSantis and Rakowsky [2] also approximated the displacement thickness to achieve a maximum at approximately two thirds of the distance from the center of the discs to their periphery, and showed that the momentum integral technique over a flat plate approximates well with their experimental data over a flow between two discs, provided that the flow is inviscid.

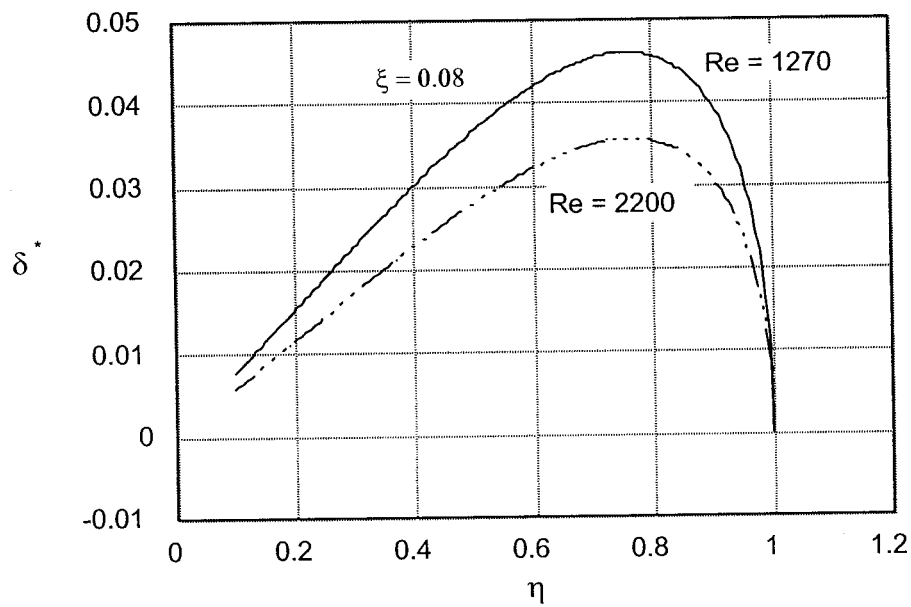


Figure 4.2 – Variation of B.L displacement thickness versus radial position

As the flow approaches the outlet the streamlines have to curve in order for the fluid to find the exit port. Consequently, in addition to the radial velocity, an axial component must be developed. According to Koval and Michailov [33], the extent of the radial location of this region can be calculated by the experimentally obtained empirical formula

$$\eta_{III} = \exp(1.132 \eta_e) - 1$$

that has been plotted in Fig. 4.3. Although we find that the values provided by the above expression to be conservative, they nevertheless provide at least an order of magnitude of the size of this sector.

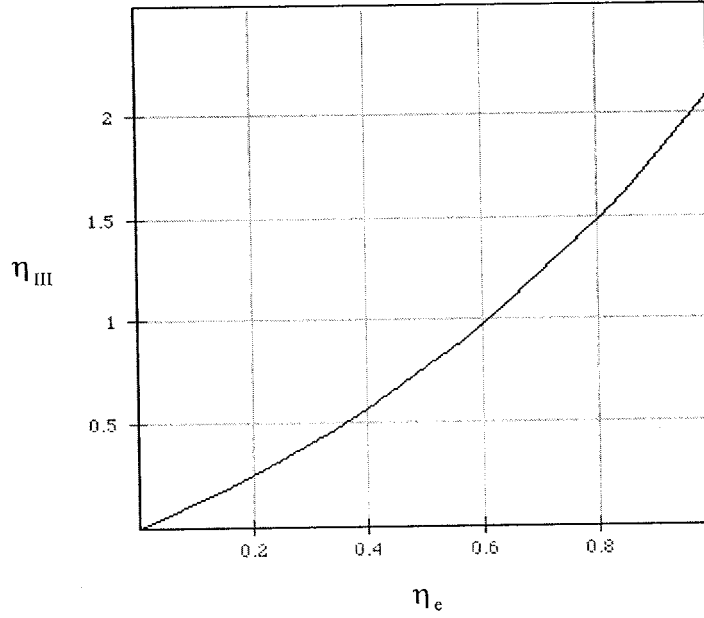


Figure 4.3 – Variation of exit zone III versus radial position η_e

In the case of small gaps, Eq. (7) suggests that both the radial velocity and static pressure distributions are solely functions of parameter λ , which is a combination of Re_r and η . For small values of Re_r , the familiar Poiseuille - like profile is present (see Fig. 4.4 or 4.5, similar to the flow between two flat plates).

As λ increases, the velocity profile levels-out at mid-gap ($\zeta = 1$). The flat region gradually expands towards the walls ($\zeta = 0$ and $\zeta = 2$) where the velocity reduces to zero via a thin layer. Comparison with the present experimental data with the theory (Eq. 63) is shown in Fig. 4.6 (a), (b) and (c). Radial velocity profiles were obtained for gap ratios

of $\xi=0.02778$, 0.01389 and Re of 328.74, 493.12 and 657.49. It is evident from the graphs that the experimental data clearly displays characteristics of the accelerating flow. The entry effects of the fluid flow into the chamber have been neglected. As the fluid progresses towards the center of the discs, the area decreases and the velocity increases for continuity to be satisfied. This results in a pressure drop in the flow direction, to be shown later.

At the inlet, the flow displayed the parabolic like Poiseuille profiles, as the viscous effects were as strong as the inertia affects. As the fluid advanced, it started to accelerate. Consequently, the profiles became more flat at the mid-channel, hence a thin boundary layer developed close to the disc surfaces. As the inlet Reynolds number increased, the inertia contribution grew larger, thus prompting the radial velocities to develop at a faster rate into their flat distribution at the mid-plane. This is also evident in Singh's radial velocity profiles [8] through his investigation at no-swirling inflow for high Reynolds numbers. However, for the largest gap ($\xi=0.02778$), a consistent asymmetry close to the disc surfaces was observed. This was not seen at the smaller height.

Moreover, for the lowest Reynolds number and gap size (Re=328.74 and $\xi=0.01389$), it is observed that the results are affected by the exit conditions as the fluid tries to negotiate the turn. The results also tend to deviate from the theoretical approximation. This occurrence is not detected in the higher gap. Singh [8] also observed that as the fluid approached the exit, velocity profiles exhibited a maximum towards the disc that contained the exit hole. This was because only one disc enclosed the outlet. Due

to insufficient data from the present results, this argument cannot be supported. More investigation is needed to explore in more detail what is happening at the exit.

It is therefore clear, with the exemption of regions I and III (figure 4.1) where the analysis is not valid, that the present theory provides reliable approximation for the velocity in Region II. A similar conclusion can also be derived using the results of Singh [8] and DeSantis and Rakowsky [2], as shown in Figures 4.7 (a) and (b) respectively. In Singh's [8] case, the inlet and exit profiles were neglected, thus the comparison with the present theory proved to be very good. In the latter study by DeSantis and Rakowsky [2], the radial velocity was measured using a hot-wire anemometer, and became evident that it is difficult to resolve the velocity near the walls adequately. This is especially true in the neighborhood of the discs' surfaces. Nevertheless, the data does provide some indication regarding the development of the radial velocity.

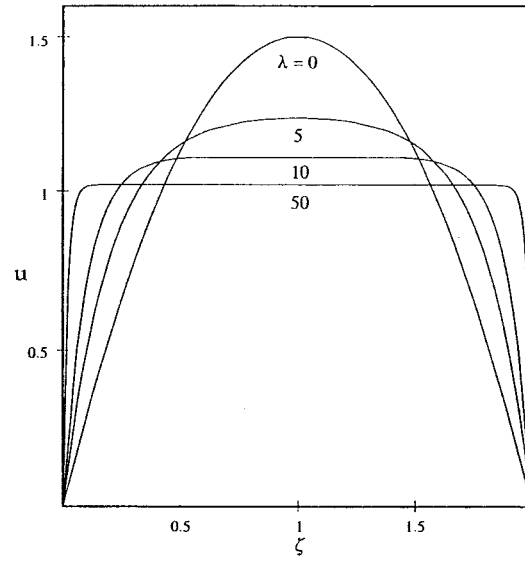


Figure 4.4 – Radial Velocity profiles for various λ

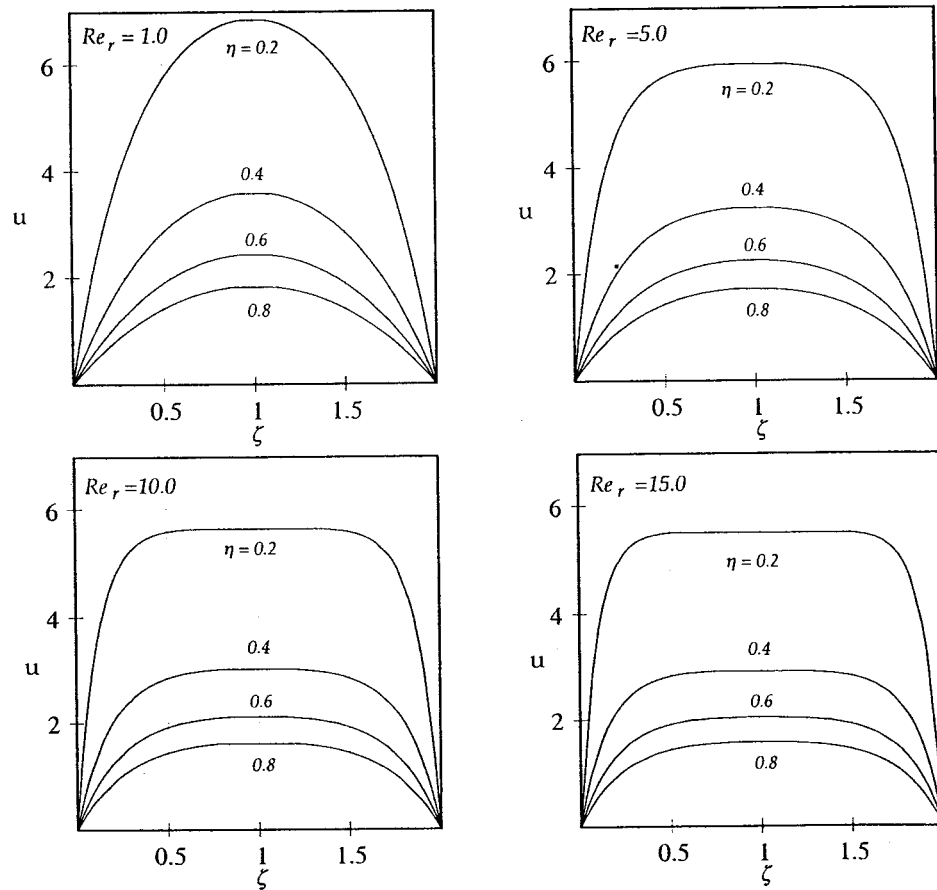


Figure 4.5 – Radial velocity profiles for various reduced Reynolds numbers

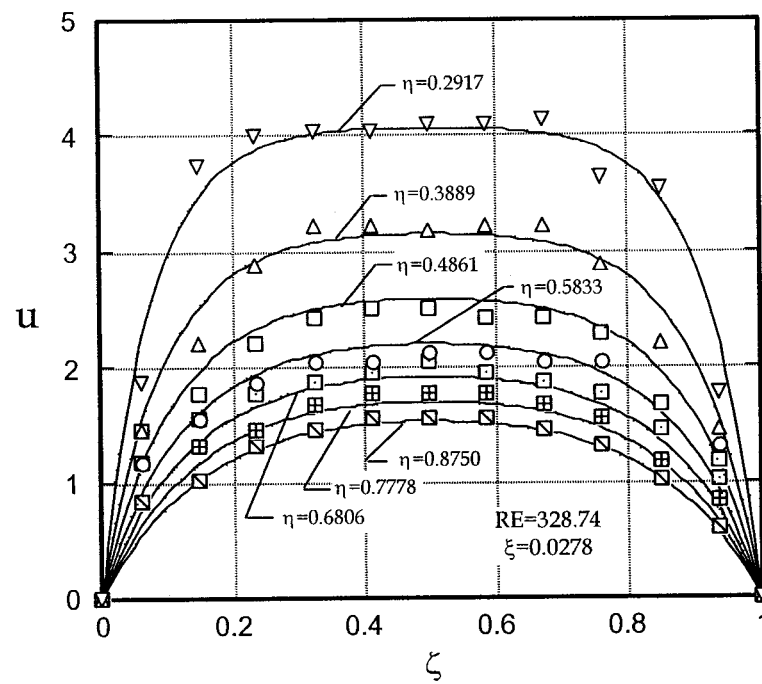
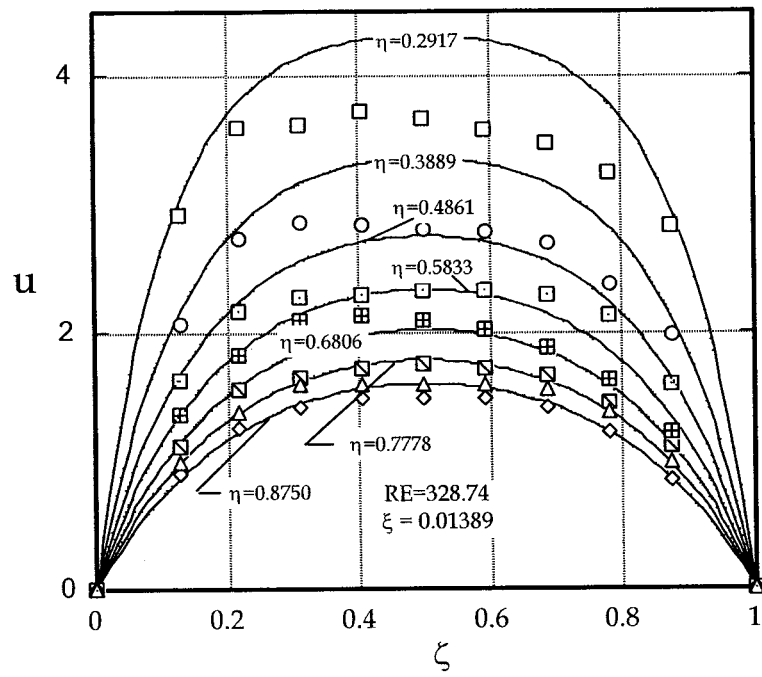


Figure 4.6 (a) – Present radial velocity profiles for $Re=328.74$

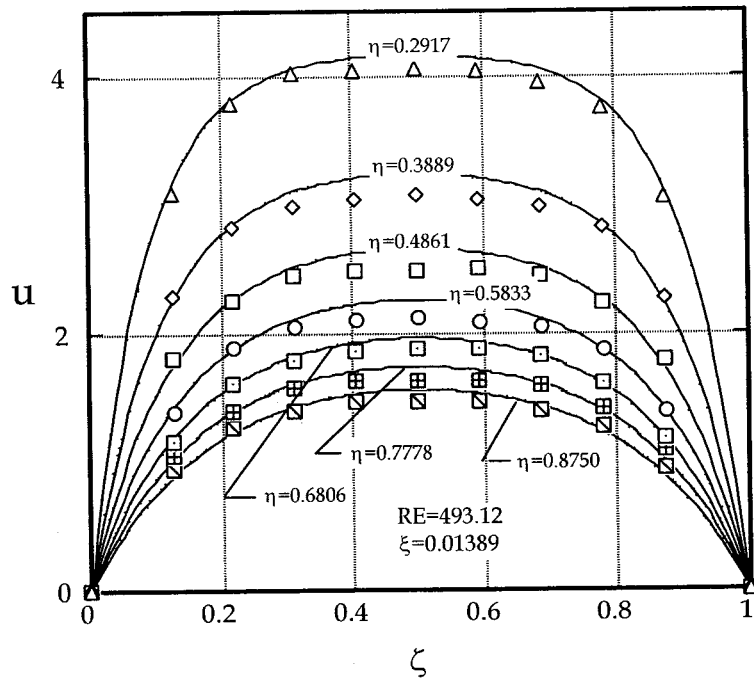
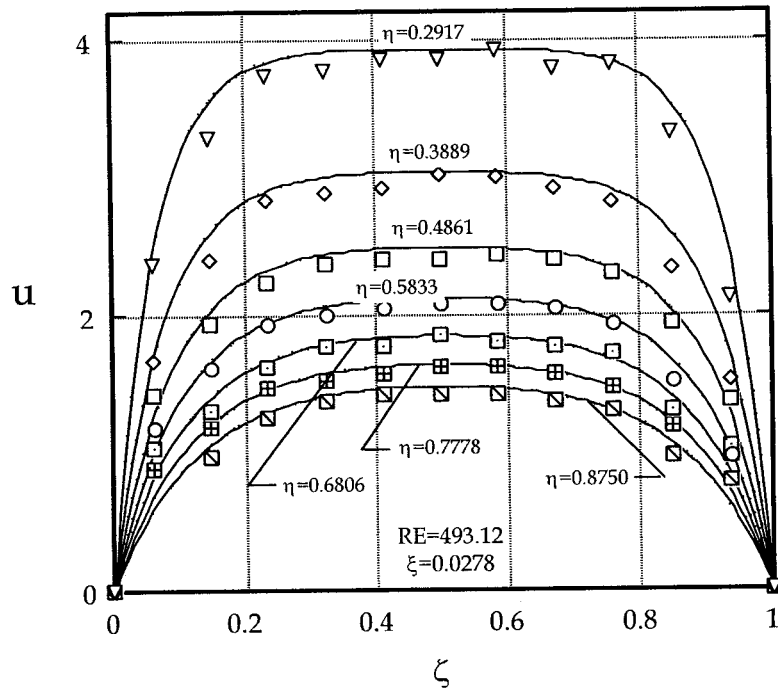


Figure 4.6 (b) – Present radial velocity profiles for $Re=493.12$

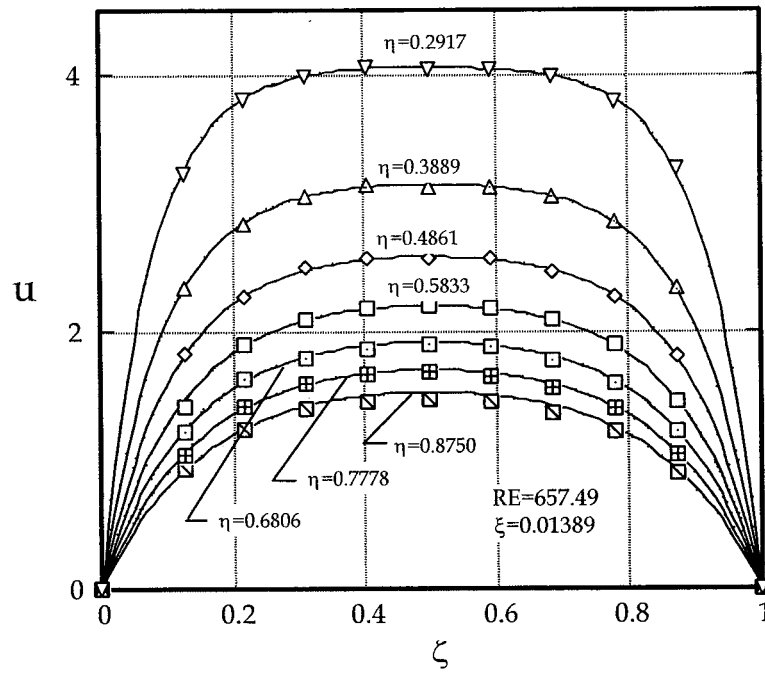
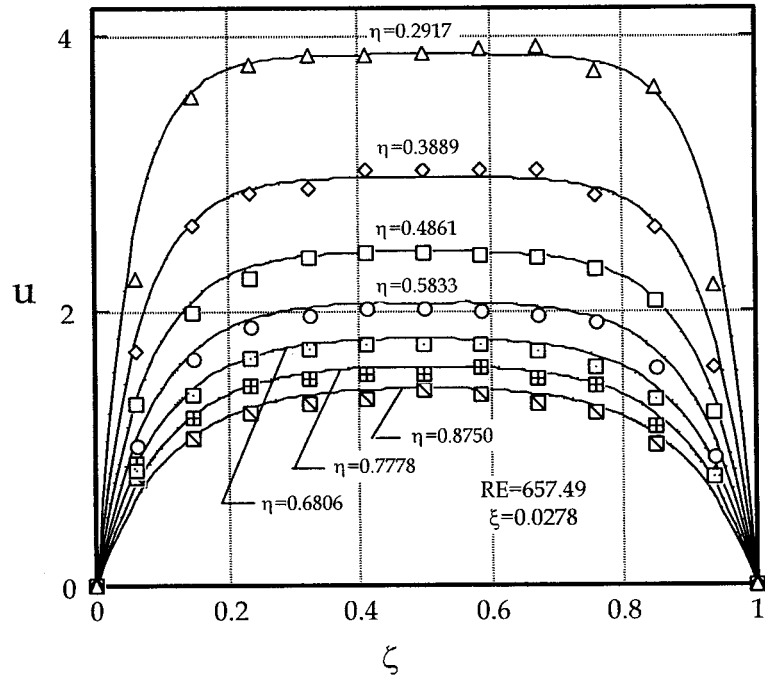


Figure 4.6 (c) – Present radial velocity profiles for $Re=657.49$

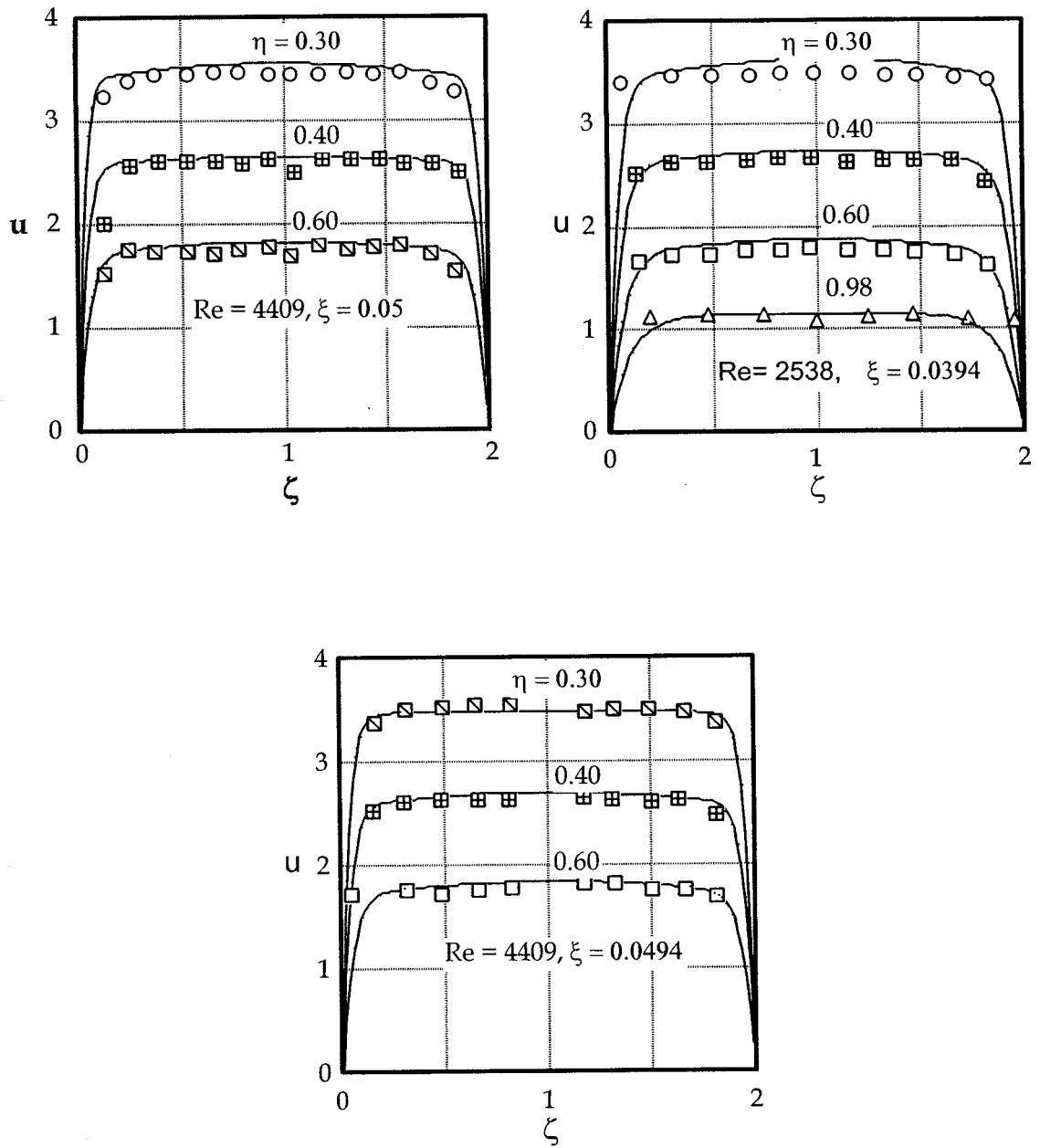


Figure 4.7 (a) –Radial velocity profiles of present theory with experiments [8]

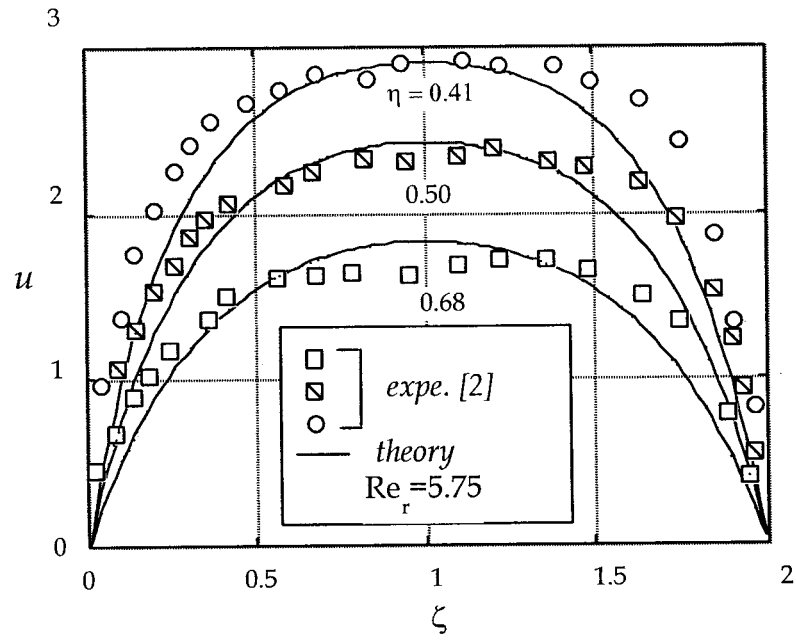


Figure 4.7 (b) – Radial velocity profiles of present theory with experiments [2]

The variation of the maximum radial velocity component as a function of the radius is shown in Figs. 4.8 (a) and (b).

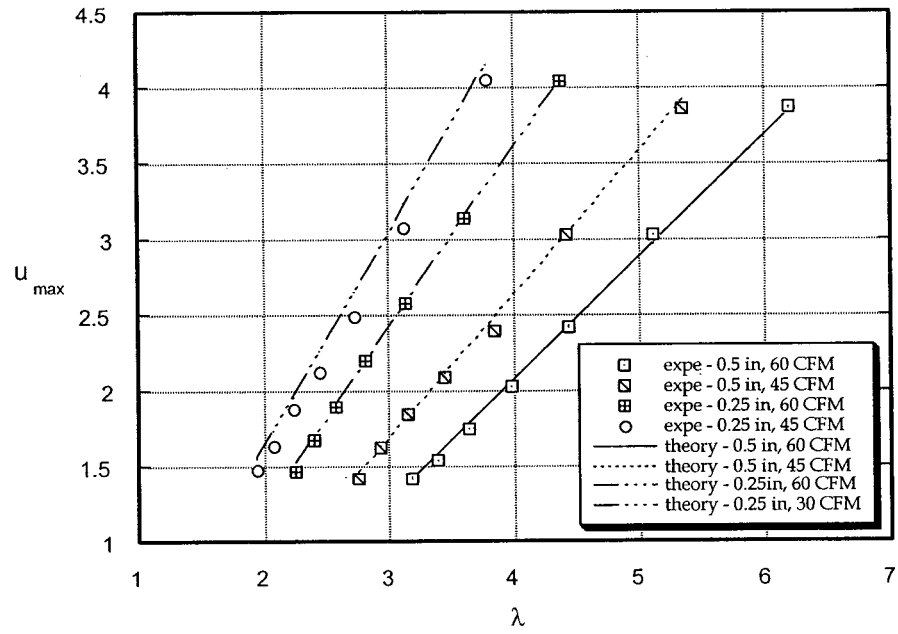


Figure 4.8 (a) – Present experimental maximum radial velocity versus λ

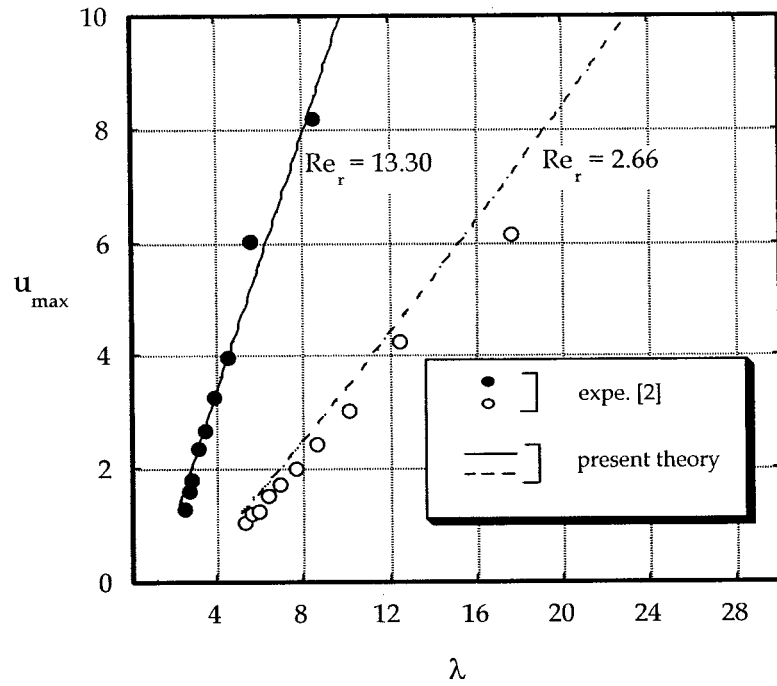


Figure 4.8 (b) Maximum radial velocity of present theory with experiments [2]

Due to flow symmetry, the second derivative of the velocity mid-channel ($\zeta = 1$) is zero. Consequently, the viscous effects in the η – momentum equation will drop-out, or

$$u_{\zeta=1} \frac{\partial u}{\partial \eta} \bigg|_{\zeta=1} = - \frac{d\Delta p}{d\eta}$$

which yields Euler's equation. Therefore, the centerline velocity should approach the potential solution. The last is evidently confirmed by Fig. 4.1.9.

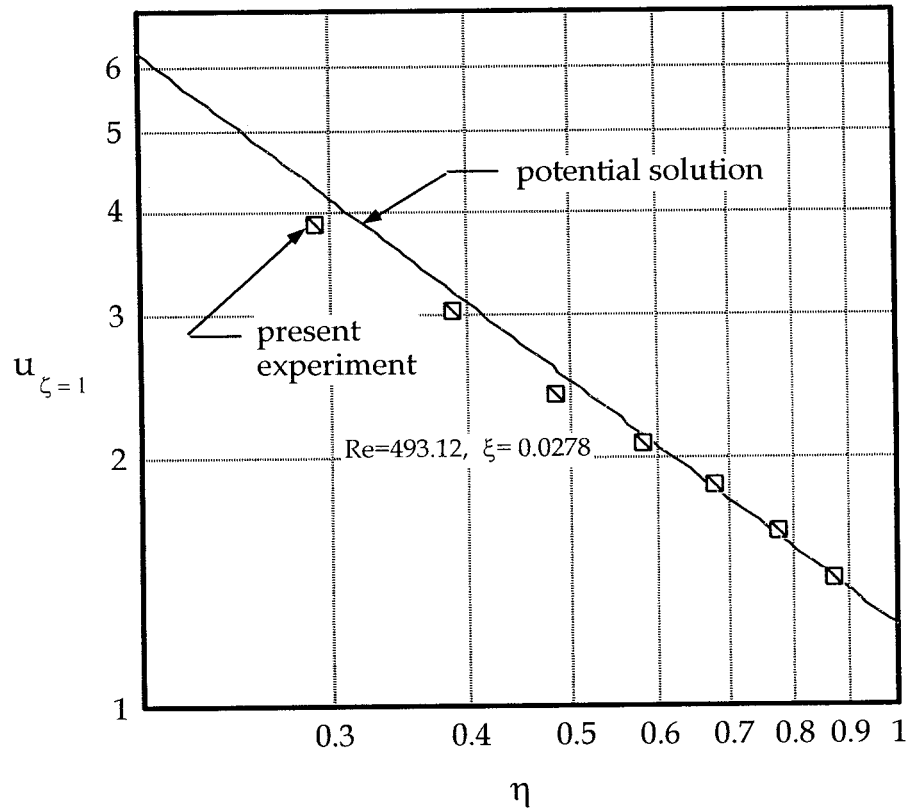


Figure 4.9 – Approximation of maximum radial velocity

As the entering fluid streams towards the center, its radial velocity increases monotonically. It is therefore anticipated that the static pressure decreases in a similar manner. Our experimental results, as well the results reported by others, do indicate this flow behaviour, see Figs. 4.10 (a) – (d).

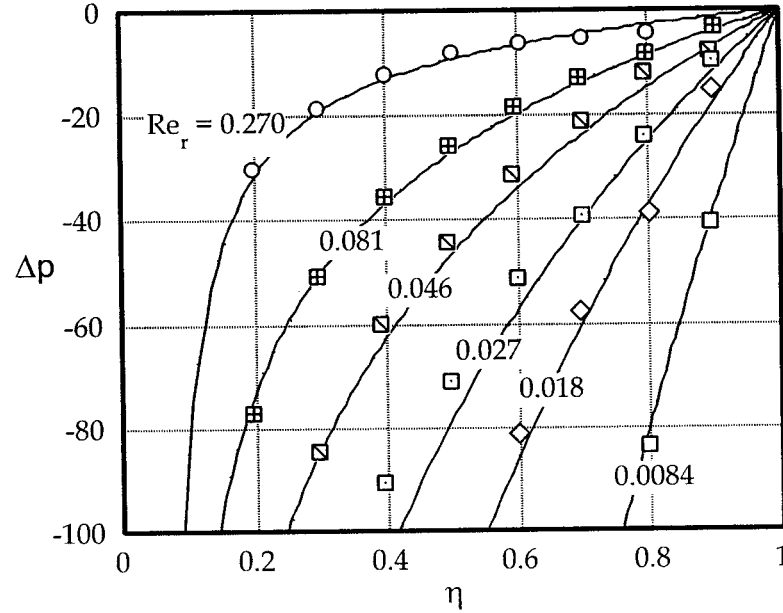


Figure 4.10 (a) – Static pressure profiles from theory [6] and experiments [32]

In figures 4.10 (b) and (c), the present experimental data is presented for the gap ratios of 0.0278, 0.01389, 0.01042, 0.00694 and Reynolds numbers of 328.74, 493.12, and 657.49. It is observed that as the inlet Reynolds number increases, the inertia effects, and consequently the acceleration, are augmented, and the pressure drops in the flow direction. This is more profound in the largest gap. As the gap ratio further decreases, the aforementioned observation is not as obvious. Rather, it appears that the pressure drops in a constant manner. Consequently, the effect of the Reynolds number or gap ratio on the

pressure distribution is minimal. That further leads to the conclusion that the smaller the gap, the more stable the flow becomes. It is also noticeable from the graphs that the theory approximates the present experimental pressure distribution very well. To validate the theory with previous work, a comparison is done in figure 4.10 (d), where the present analysis is plotted against Singh's experimental data and his numerical solution. It was found that the analysis approximates the experiments better than the more complicated solution by Singh [8] that contains the turbulence $k-\varepsilon$ model. Therefore, a simpler approximation for the pressure that uses the assumption of the laminar flow better predicted the experimental findings by Singh [8], and marks the behavior of the accelerating flow, which tends to laminarize if it is initially turbulent. That is further supported by the fact that the turbulent intensities were found to decrease with increasing Reynolds numbers, thus reaching the conclusion that the accelerating flow suppresses any turbulent fluctuations. [11]

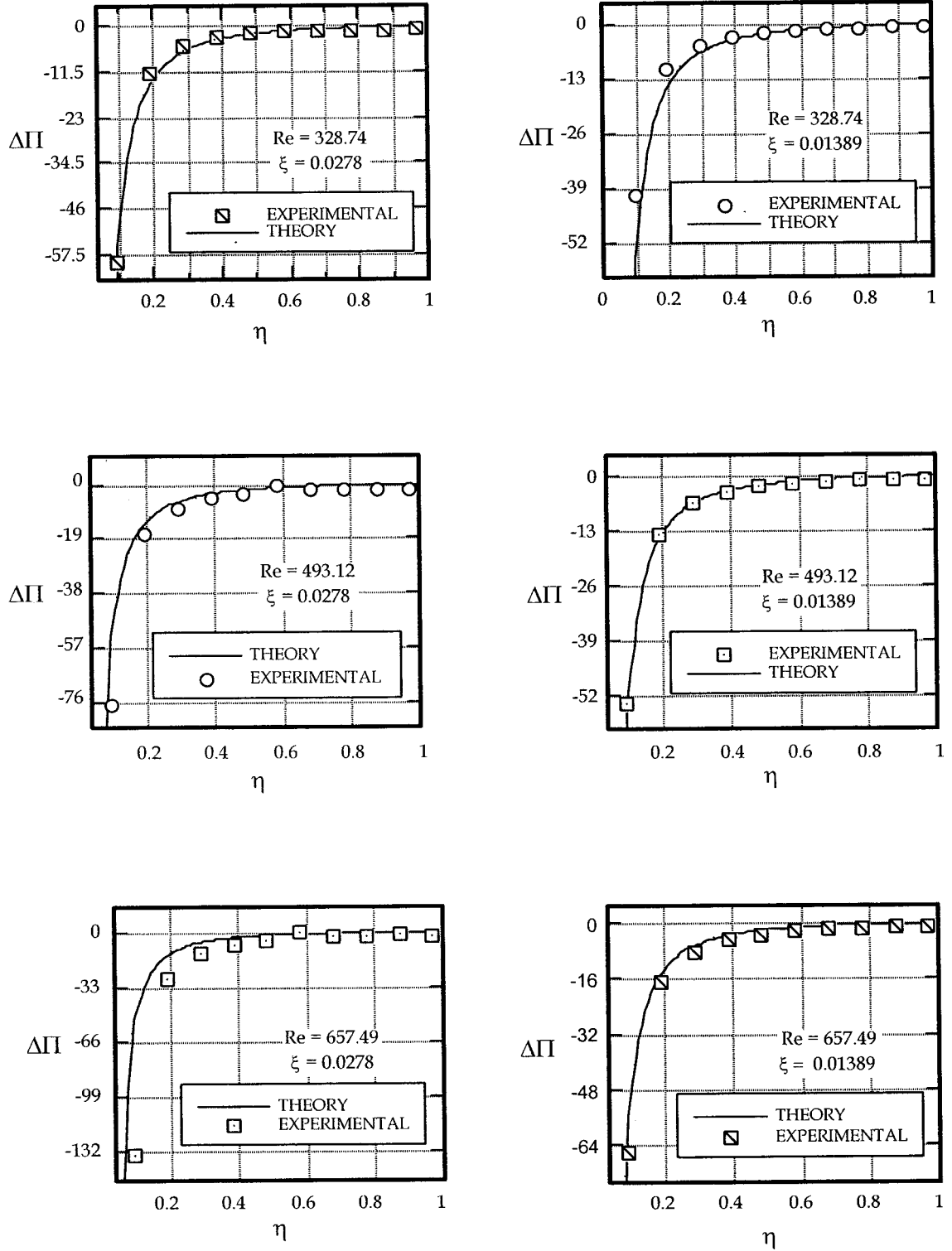


Figure 4.10 (b) – Static pressure profiles for non-swirling inflow and for $\xi = 0.0278$,
0.01389

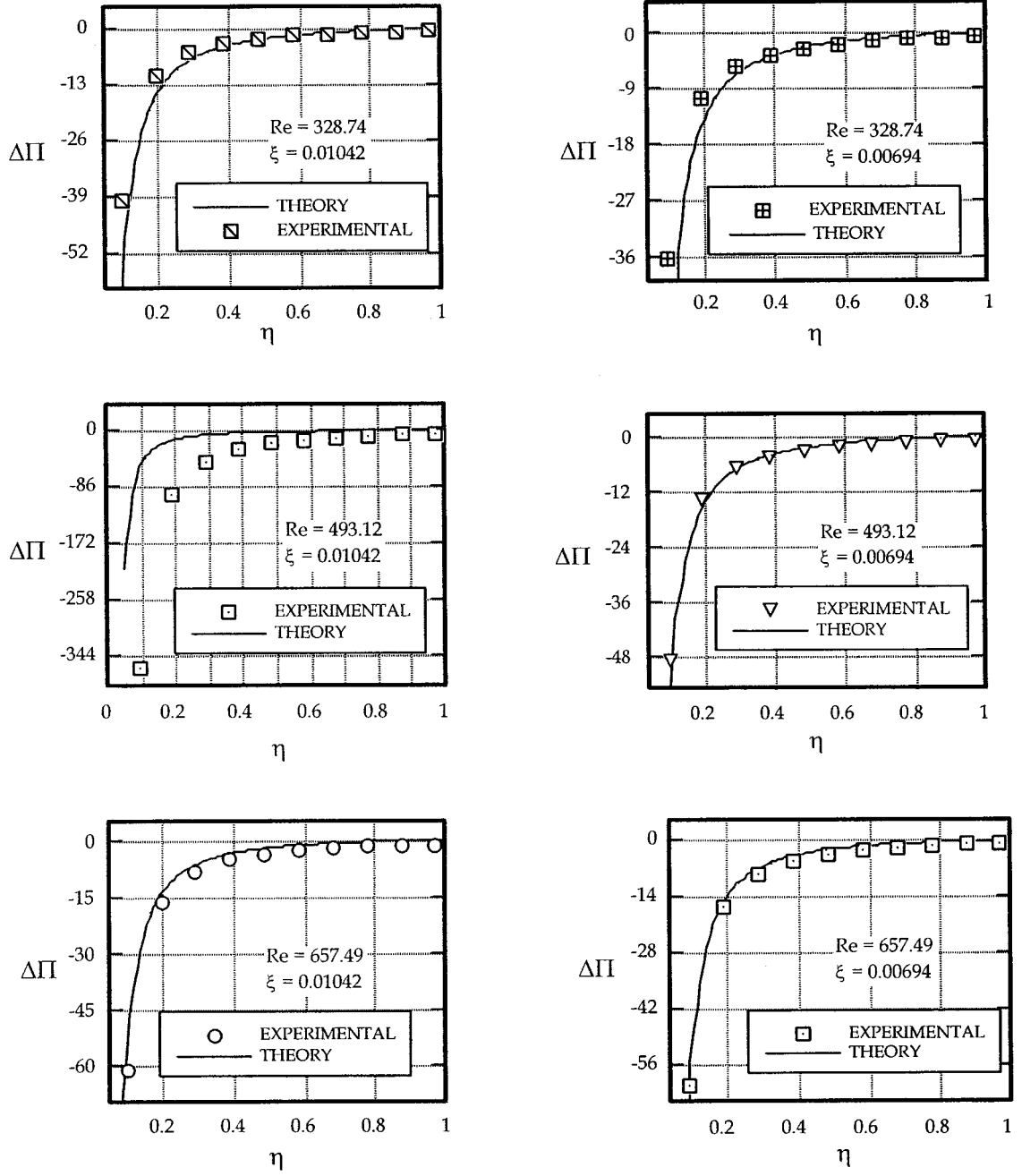


Figure 4.10 (c) – Static pressure profiles for non-swirling inflow and $\xi = 0.01042$,
0.00694

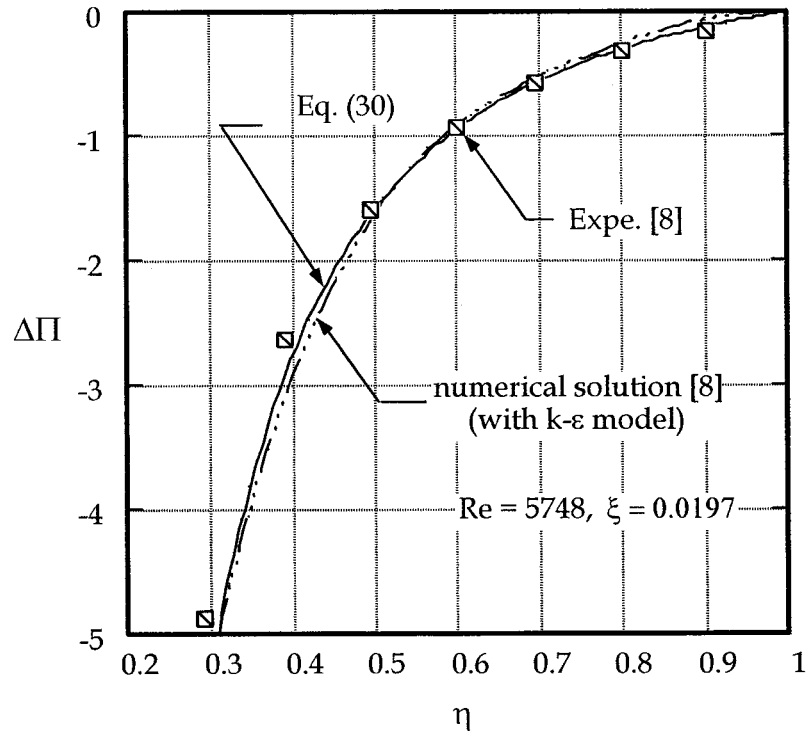
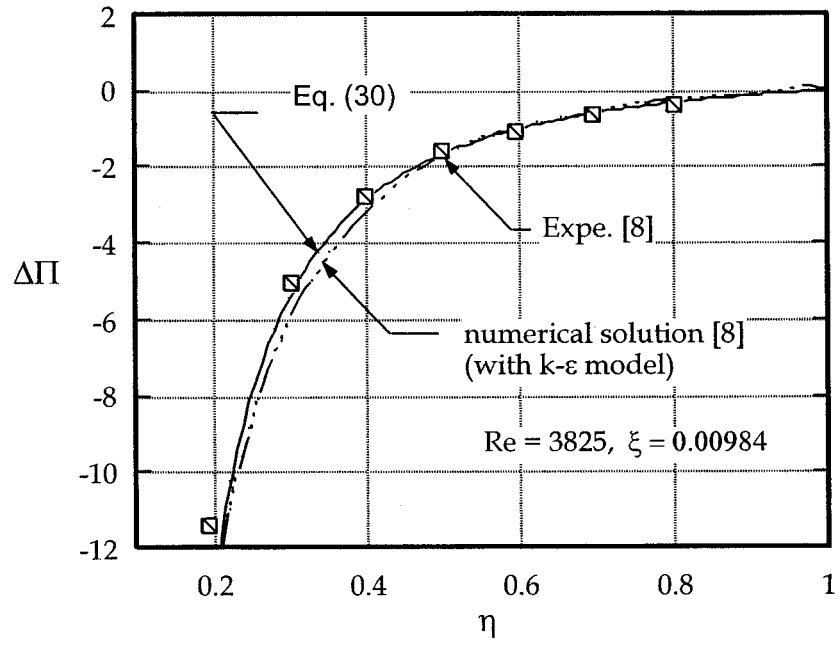


Figure 4.10 (d) – Static pressure approximation of present theory with [8]

II. Swirling Flow

The analysis, including the effects of swirl, suggests that the radial velocity distribution is unaffected. It would be interesting to experimentally confirm the theoretically obtained conjecture about the form of the latter velocity for stationary discs with swirl flow at the inlet. The only reliable experimental data for the radial velocity in such geometry is that of Savino and Keshock [13]. Unfortunately, these pertain to relatively large gaps ($h/R_{in} \approx 0.1$), a condition for the radial velocity that is outside the range of the present study. As the fluid enters the gap through the inlet, a strong centrifugal force field immediately confronts it. In its attempt to find the outlet with the least opposition, it flows closely to the discs where the tangential velocity reduces in order to satisfy the non-slip condition on the solid wall. This in turn produces the Ekman's boundary layers, which are characterized by two radial velocity peaks near the plates. They are however unsuitable for comparisons to the present asymptotic flow solution.

With their experiments for very high swirl, Savino and Keshock [13] confirmed, that the bulk of the radial flow was diverted in the neighborhood of the outer walls. As the fluid progressed to the center of the discs, the radial velocities increased, hence creating peaks at the end walls, while at the mid section the radial momentum decreased significantly. This is an indication that the centrifugal effects were dominant in that region. Wormley [12] also confirmed the lack of radial flow at the mid section by his milk injection visualization technique. In his experiments, a "milky ring" occupied the mid region of the chamber for a long time, while the exit areas and next to the walls were

free of milk. As the swirl strength decreases, the centrifugal forces decrease, and so a considerable amount of radial flow penetrates the middle section between the two discs.

For considerably smaller gap ratios, the Ekman's layers are expected to merge, and approach the conditions of the present analysis. This is the case indicated in figures 4.11 (a) and (b), where the swirl is very weak and the radial velocity is seen to develop a dimple at the mid-channel, which is the initial stage of the development of Ekman's boundary layer. At higher gaps and a stronger swirl, the depression observed in the middle will grow larger, thus maturing to the phenomenon described previously.

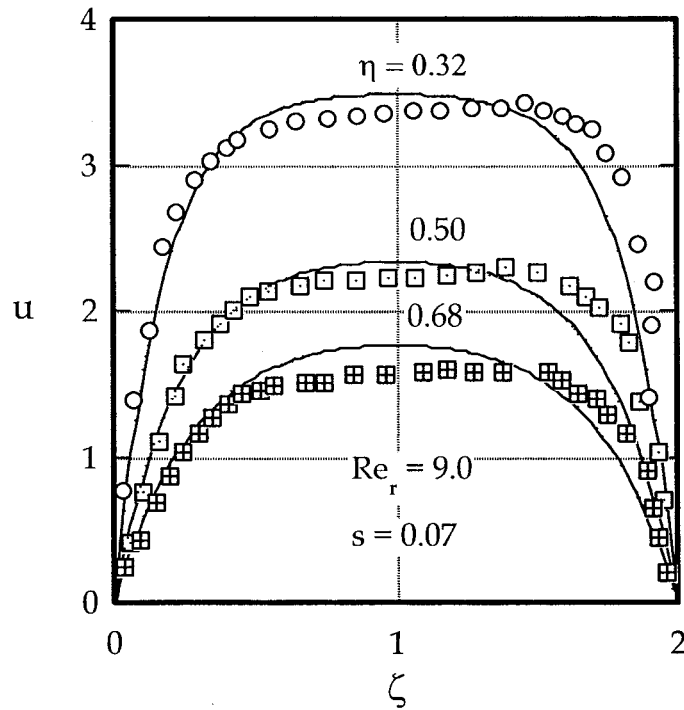


Figure 4.11 (a) --- Radial velocity profiles of present theory with experiments [2] for $s = 0.07$

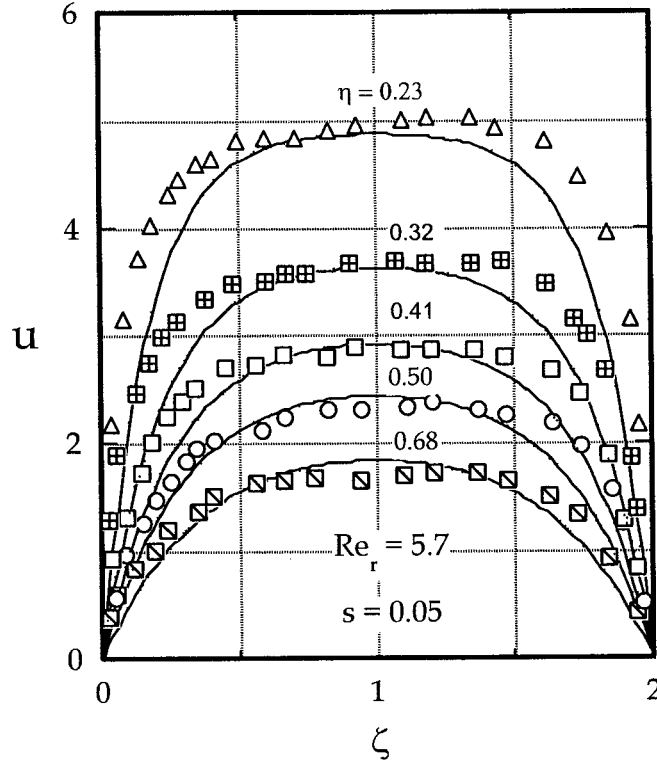


Figure 4.11 (b) – Radial velocity profiles of present theory with experiments [2] for $s = 0.05$

The development of the tangential velocity component for the case of stationary and rotating discs with swirl at the inlet is shown in Figs. 4.12 and 4.13 respectively. It is clearly evident that the tangential velocity exhibits characteristics similar to that of the radial velocity. For small values of Re_r , the familiar Poiseuille like profile appears. When we increase Re_r , the velocity profile flattens at mid-gap, progressively spreading towards the walls. A closer look at the tangential momentum equation reveals that vorticity is carried by convection in the η -direction, meanwhile in the ζ -direction it is diffused by only the action of viscosity. For large Re_r values, the diffusion is confined within the layers near the plates, leaving the rest of the fluid in the ζ -direction oblivious to the

action taking place near the solid walls.

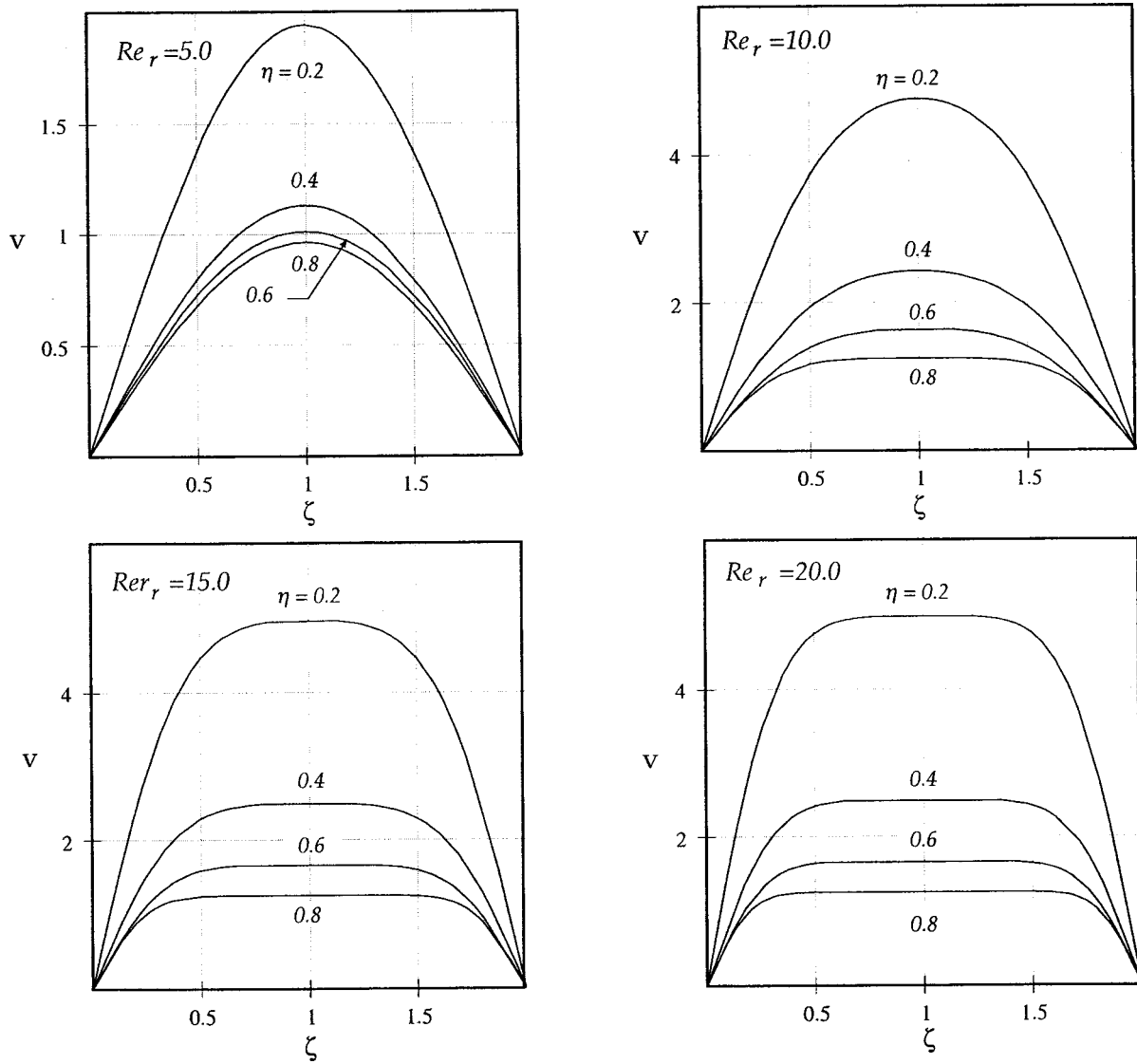


Figure 4.12 – Theoretical tangential velocity profiles for two stationary discs

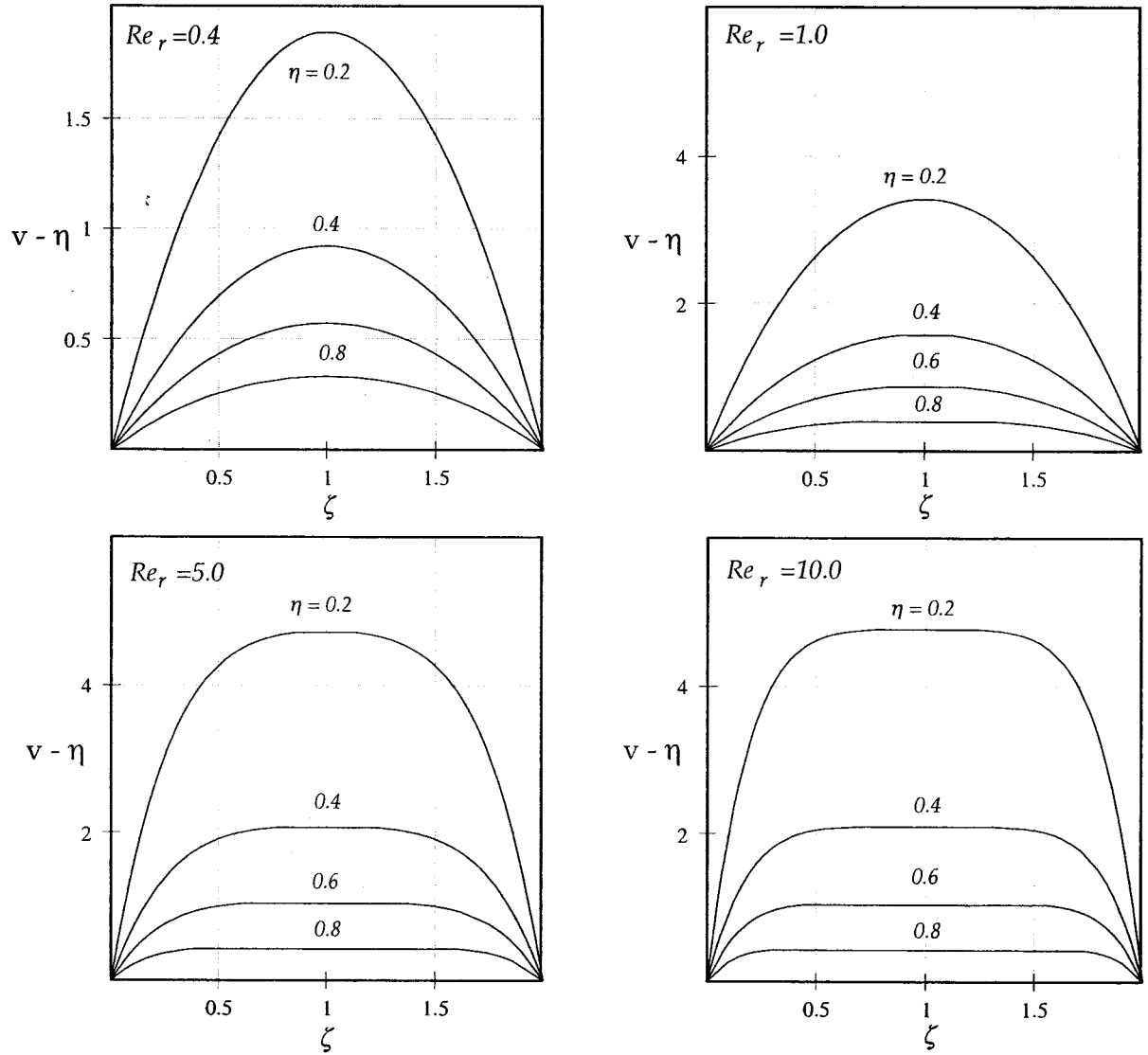


Figure 4. 13 – Theoretical tangential velocity profiles for two rotating discs

The maximum tangential velocity occurs at the mid-channel height ($\zeta = 1$). Its variation with the radius η is shown in Figs. 4.14 and 4.15. It is apparent that as Re_r increases, both cases tend asymptotically to a potential vortex distribution. It is also evident that the rotating disc arrangement tends faster to the potential profile than the stationary disc case. For the case of stationary discs (fig.4.14), it is observed that for low Reynolds numbers the tangential velocity decreases considerably as it enters the disc chamber due to the strong viscous effects. As the fluid accelerates, the radial velocity increases and further feeds the tangential velocity component, which in turn starts to grow. For higher Reynolds numbers, the drop at the entrance gets smaller and the tangential velocity approaches the potential vortex faster. In fact, for Re_r values of 12 and 9 for stationary and rotating disc situations respectively, the maximum deviation from the free vortex is less than 0.1 %. When $Re_r \rightarrow \infty$, the curvature of $V\eta \rightarrow 0$ at $\zeta = 1$, and thus from Eq. (3) $V_{max}\eta \rightarrow 1$ which is the characteristic property of a potential vortex.

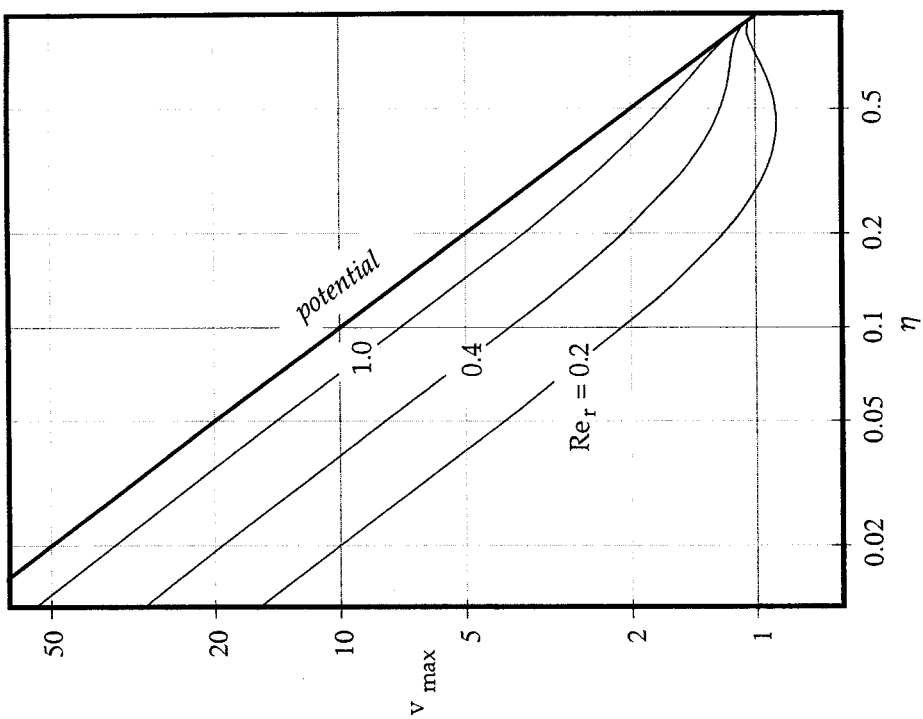


Figure 4.15 – Maximum tangential velocity
versus η for rotating discs

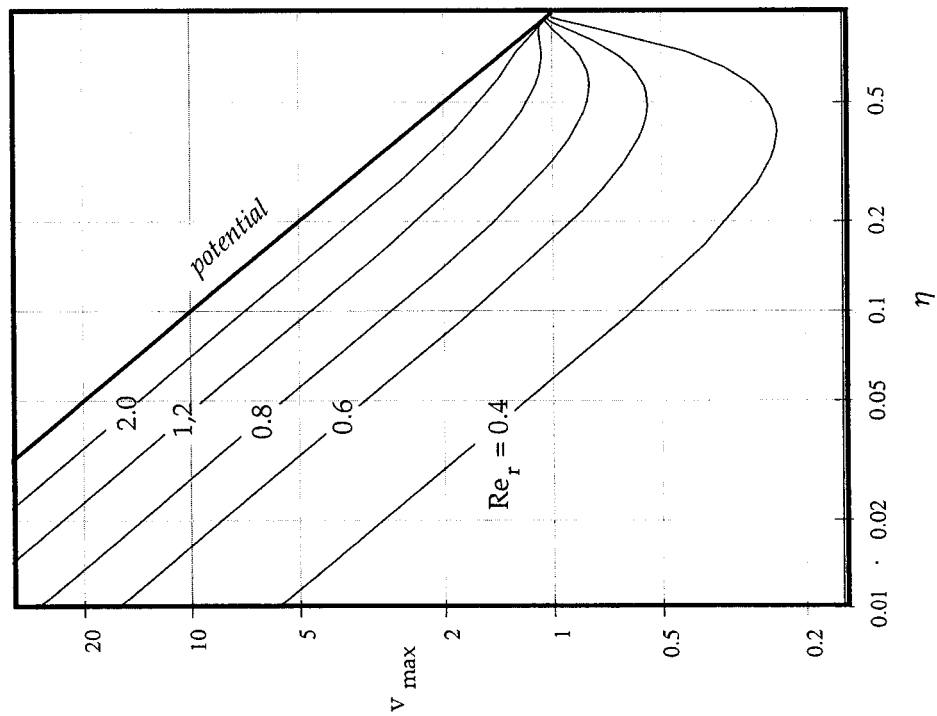


Figure 4.14 - Maximum tangential velocity
versus η for stationary discs

For low Reynolds numbers, the maximum velocity first undergoes a gradual decrease, and then recovers, tending to an asymptotic profile for smaller radii. Therefore, for high Re_r values, as it is amply evident from the experiments of Savino and Keshock [13], and DeSantis and Rakowsky [2] (see Fig. 4.16 (a)), and (b) respectively), the mid-gap value of the tangential velocity must be close to the free-vortex. In figure 4.16 (a) the value for $\eta = 0.15$ [13] is the exemption to the rule. One has to realize however, that this point is inside the outlet tube ($R_e/R_{in} = 0.2$) where the flow is turning towards the exit. In fact, the diminishing deviations of points $\eta = 2.0, 0.25$, and 3.0 from the free-vortex might also be due to the same effect.

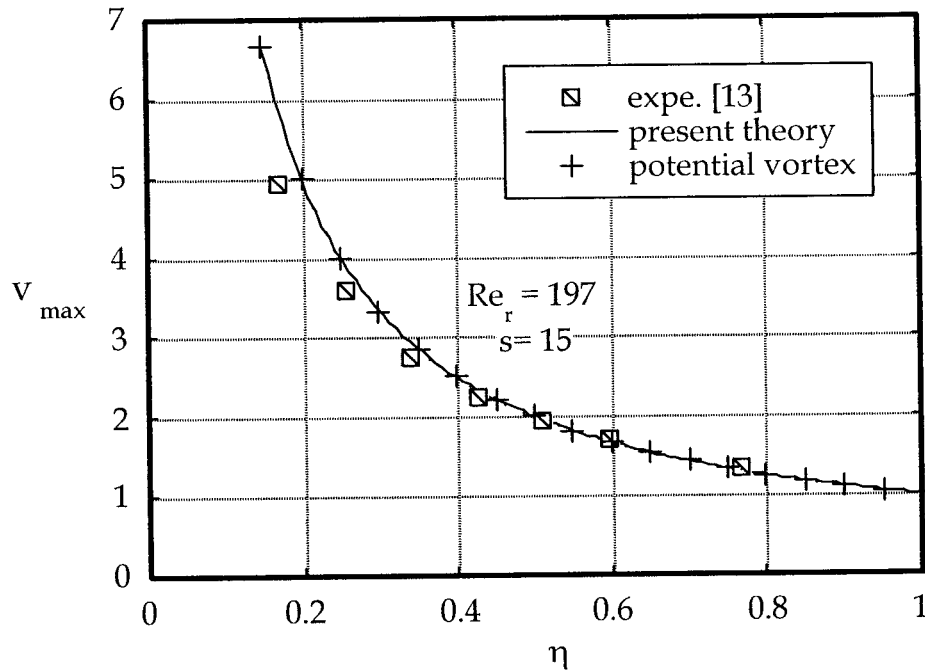


Figure 4.16 (a) - Maximum tangential velocity for $Re_r=197$ and $s=15$

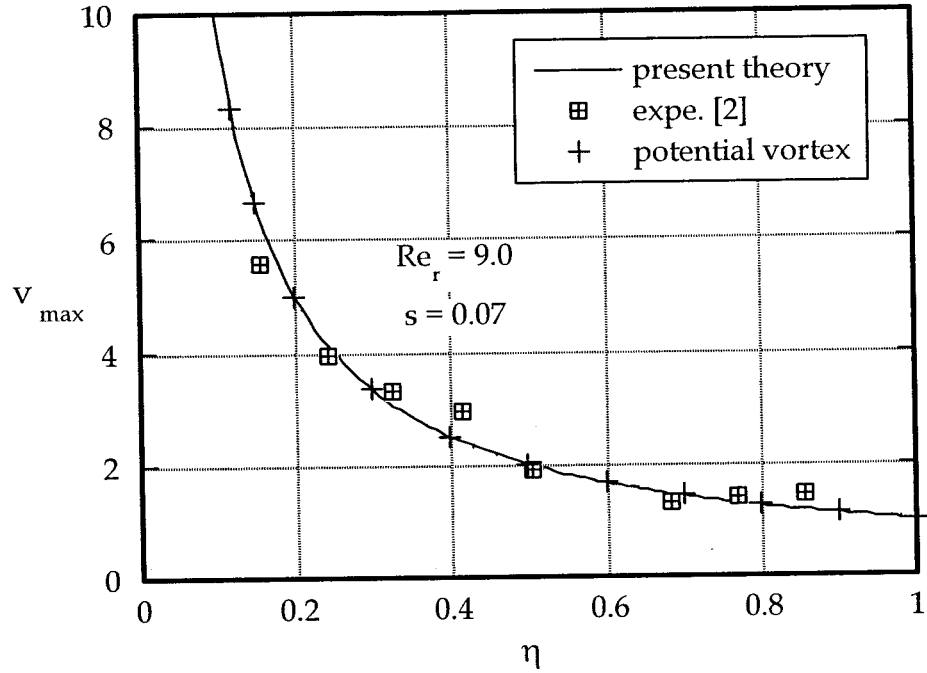


Figure 4.16 (b) – Maximum tangential velocity for $Re_r=9.0$ and $s=0.07$

Comparisons between the experimental [13] and theoretical (Eq. 26) tangential velocity distribution are found in Fig. 4.17. It is well known that in the case of a strong swirling flow like in the Savino and Keshock [13] experiments, the tangential velocity dominates the other two components and it increases significantly with a decreasing radius. It is therefore no surprise to find the theoretical tangential velocity to agree reasonably well with the experiment, while the radial velocity may not.

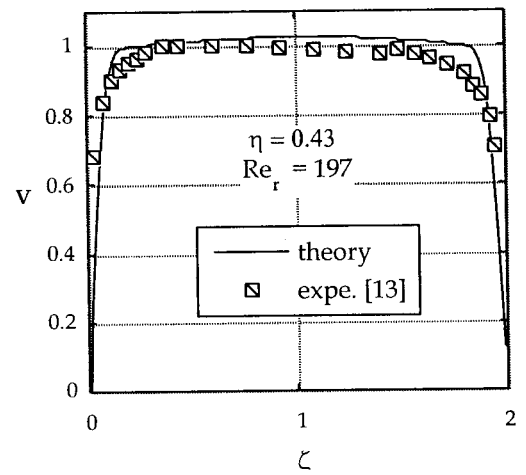
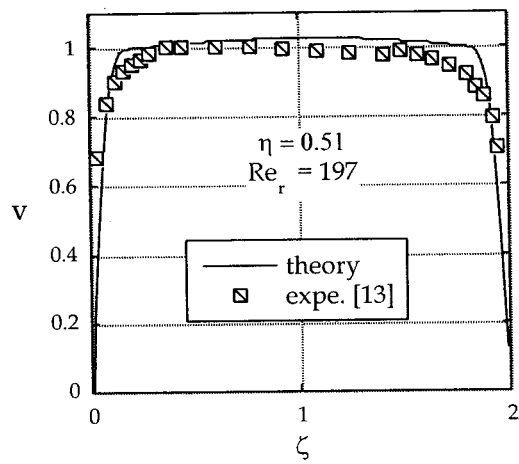
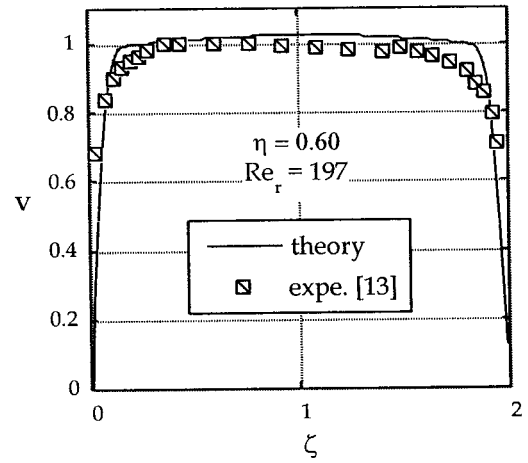
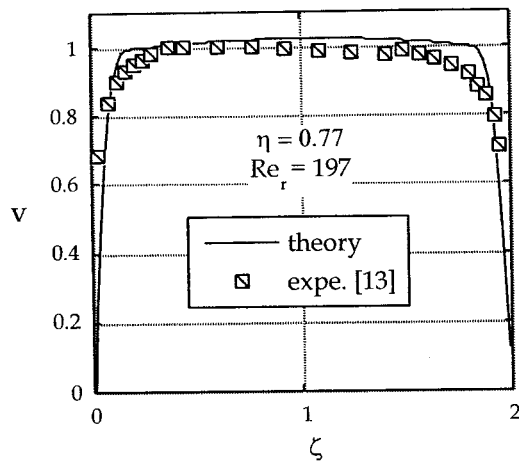


Figure 4.17 – Tangential velocity profiles from [13]

It has been shown previously that in the case of relatively large Re_T values, the tangential velocity at the mid-plane tends towards the free-vortex profile. Consequently,

$$\int_1^\eta \frac{v_{\max}^2}{\eta} d\eta \rightarrow \frac{\eta^2 - 1}{2\eta^2}$$

or

$$\Delta\Pi(\lambda) = \Delta\Xi(\lambda) + s^2$$

For this particular condition, the pressure $\Delta\Pi$ is only a function of parameter λ . Profiles of the static pressure as a function of λ for different swirl ratios (s) are shown in Fig. 4.18. The majority of the experimental points in the graph pertain to $s = 0$. Nevertheless, the pressure reported in Ref. [13] ($s \approx 15$) correlates reasonably well with the present theory.

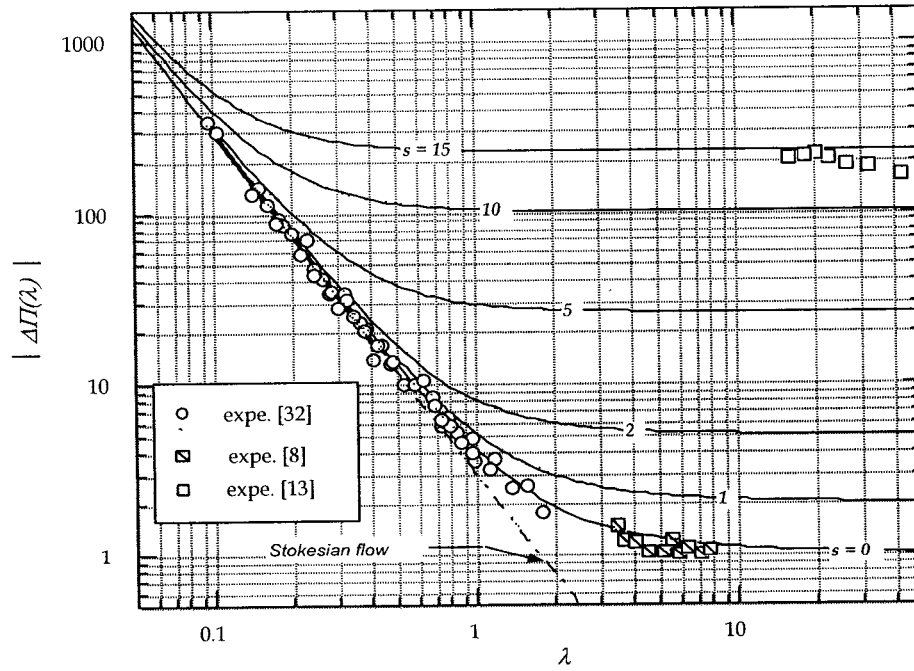


Figure 4.18 – Pressure $\Delta\Pi$ versus dimensionless parameter λ

For relatively small Re_r values ($Re_r < 12$ for stationary discs and $Re_r < 9$ for rotating discs) the original pressure equation must be used. Confirmation of its validity is shown in Fig. 4.19.

$$\Delta p(\eta) = \Delta \Xi(\eta) \frac{\eta^2 - 1}{2\eta} + s^2 \int_1^\eta \frac{v_{max}^2}{\eta} d\eta$$

It is observed that the static pressure profiles follow the trend dictated by the accelerating flow. The acceleration effects are not so strong at the entrance to the disc chamber, therefore the pressure drop decreases slowly from the periphery of the discs up to halfway through the center of the disc chamber. As the fluid strongly accelerates with decreasing area, the pressure drops significantly as the fluid approaches the exit. Moreover, it is seen that for the smaller gaps of $\xi = 0.01042$ and 0.00694 , the present theory approximates the experiments better. As the gap increases in the experimental results there is a deviation from the theory at the mid level of the discs. This might be due to the interaction of the radial flow with the centrifugal effects, which has as a result the beginning of the diversion of the radial flow towards the end wall boundary layers.

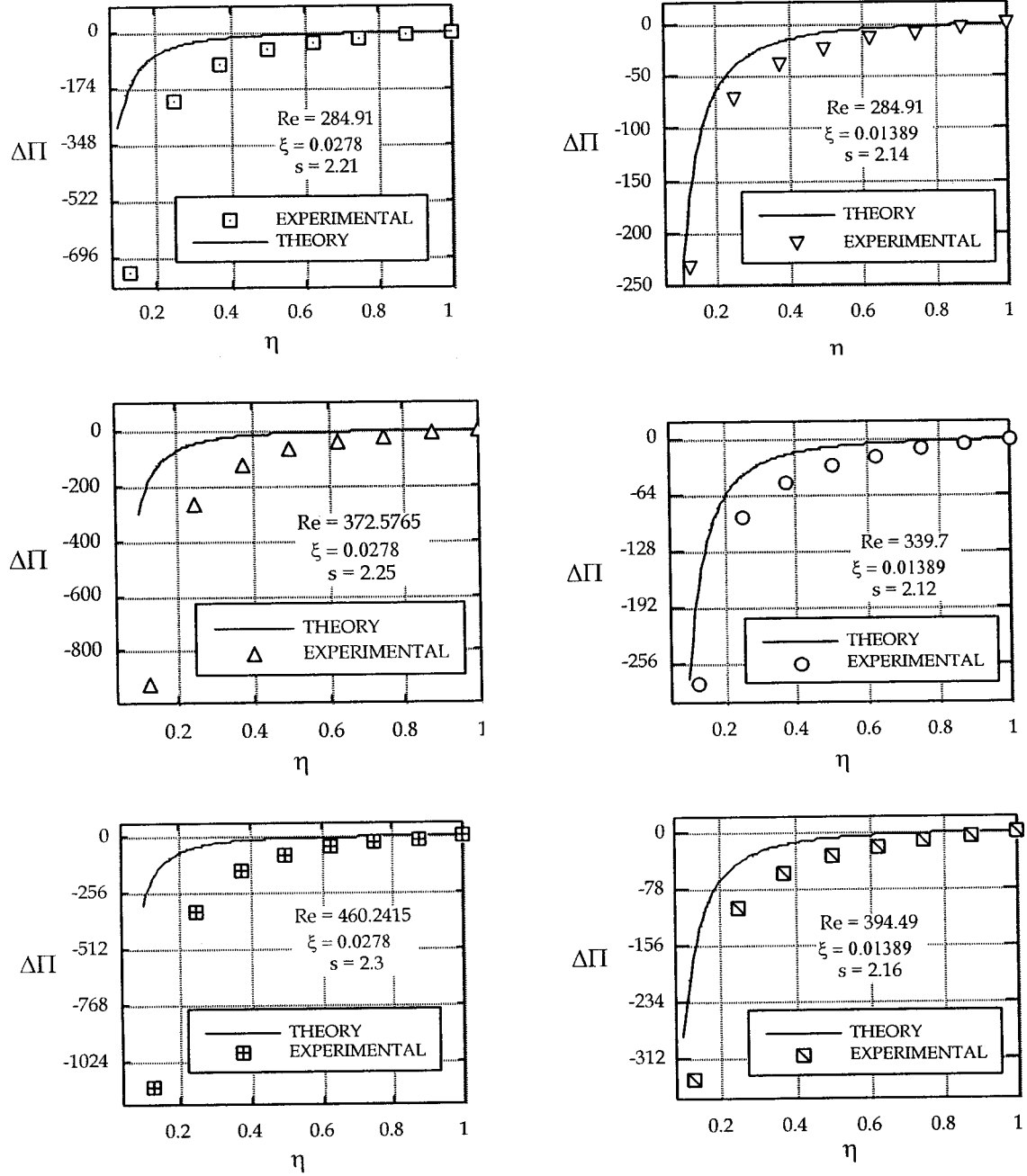


Figure 4.19 (a) – Static pressure profiles for swirling inflow and for $\xi = 0.0278, 0.01389$

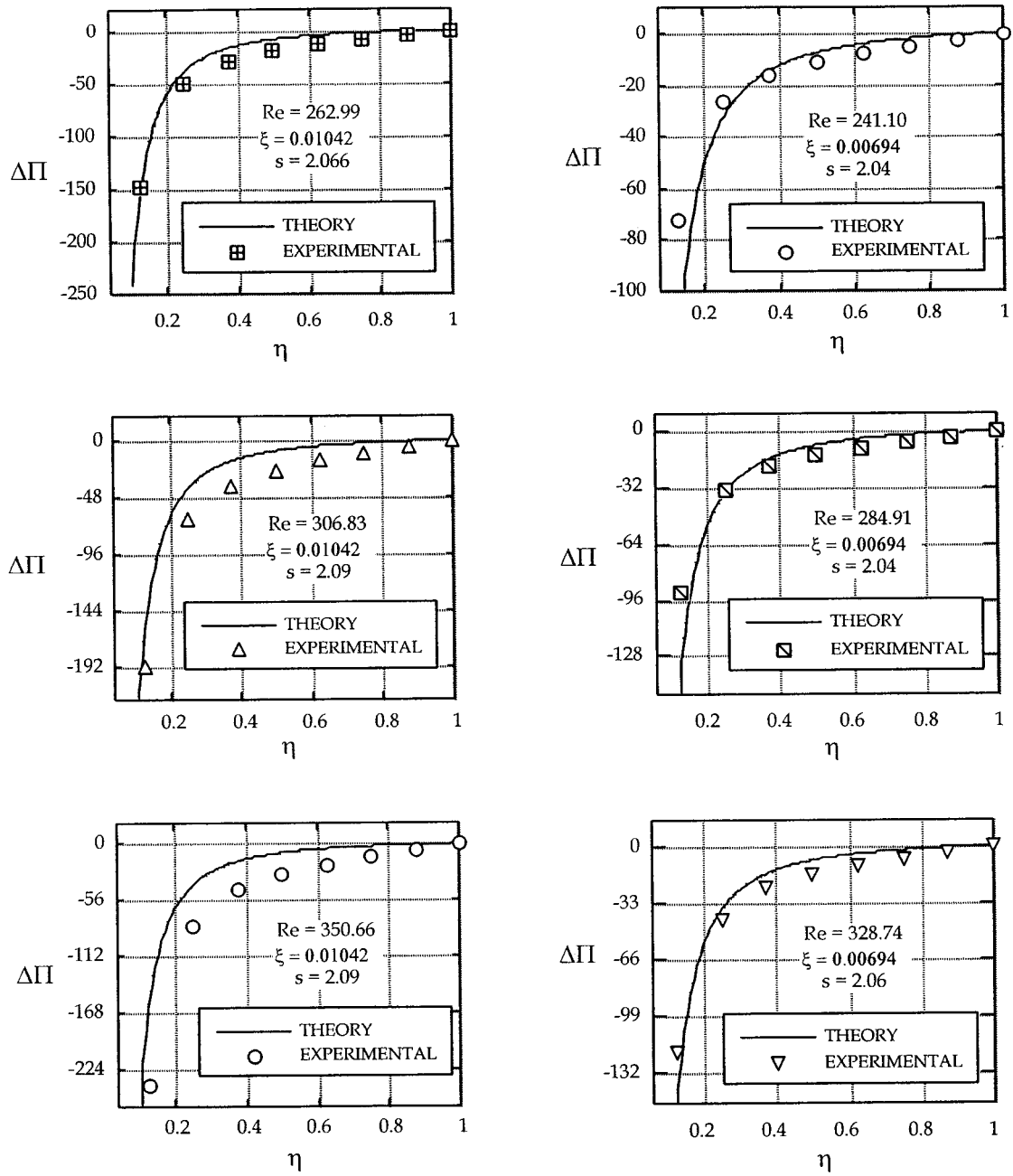


Figure 4.19 (b) – Static pressure profiles for swirling inflow and for $\xi = 0.01042, 0.00694$

A comparison of static pressure profiles between swirling and non-swirling sink flow is presented. The reduction of pressure is similar to the condition without swirl, but due to the presence of the strong vortex, it now becomes more dramatic, see Fig. 4.20.

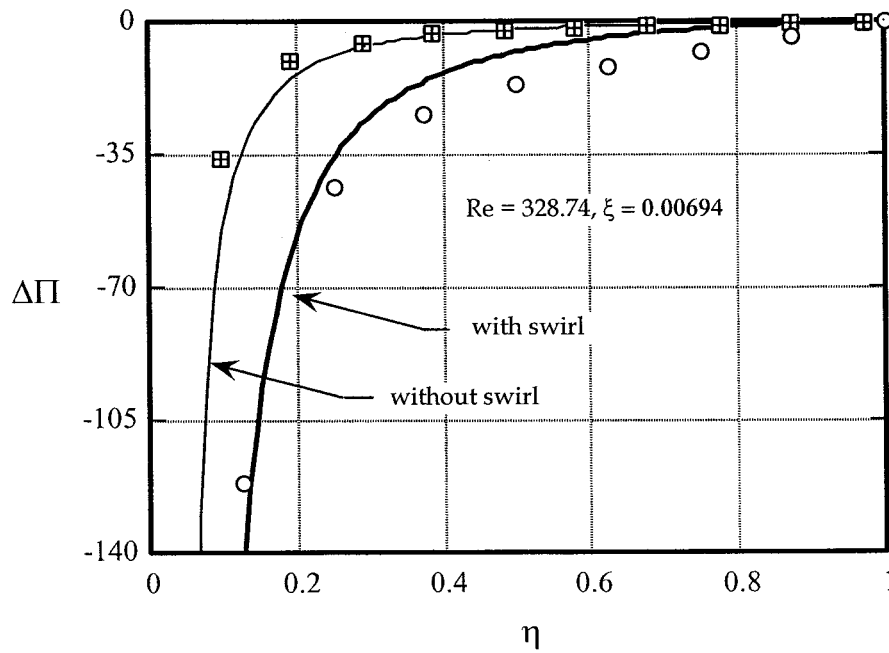


Figure 4.20 –Present static pressure profiles for swirling and non-swirling inflow

4.2 Source Flow

A decelerating (or source) flow unfolds by reversing the flow direction of the previous case. Three particular flow types are known to occur in the latter fluid motion. At relatively low inlet Reynolds numbers, a laminar flow emerges throughout the gap. For intermediate inlet Reynolds numbers, a decaying, self-controlled oscillatory flow emerges. Finally, for high inlet Reynolds numbers, this condition is replaced by a self-sustained fluctuating flow that progressively matures into a laminar-turbulent transition. This is followed by a reverse flow transformation and a condition that bears a resemblance to laminar flow at larger radii. Because of the enhanced time-dependent complexity exhibited by this type of flow, it is to be understood that the results presented here concern the time-averaged flow field effects. A more detailed description should however consider the dynamic effects that can perhaps be described by the Particle Image Velocimetry.

I. Non – Swirling Flow

The fluid entering the gap through the inlet pipe must immediately turn. However, because of the fluid's inability to negotiate a 90-degree corner, a *vena contracta* is formed near the inlet (Region I), as established in Fig. 4.21. In its attempt to respond to the reduced area of the inlet, the fluid accelerates locally. Since the streamlines are squeezed at the inlet bend, a secondary flow results and the pressure no longer remains constant along the curved path. Due to the sharp edge at the entrance, flow separation causes the formation of a recirculation zone.

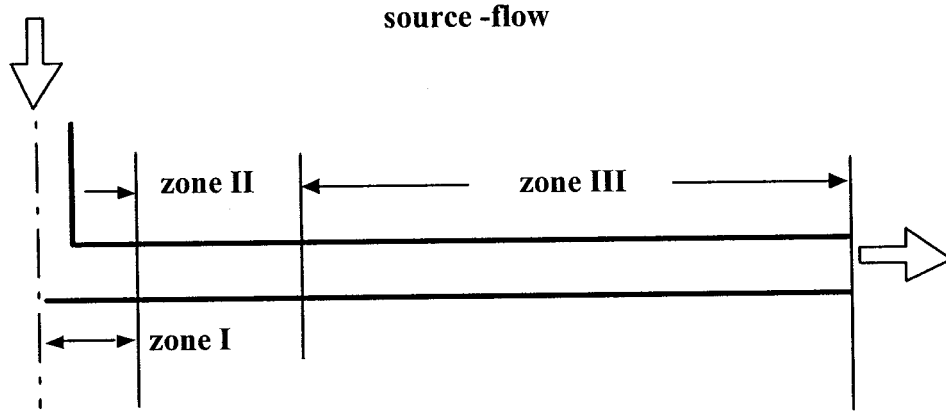
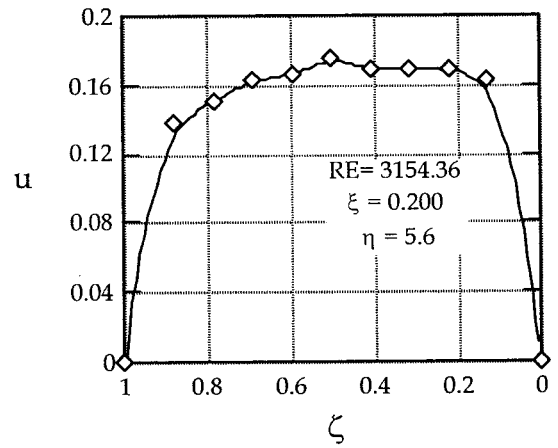
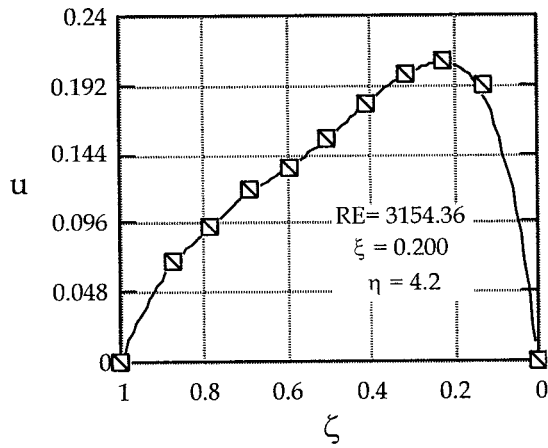
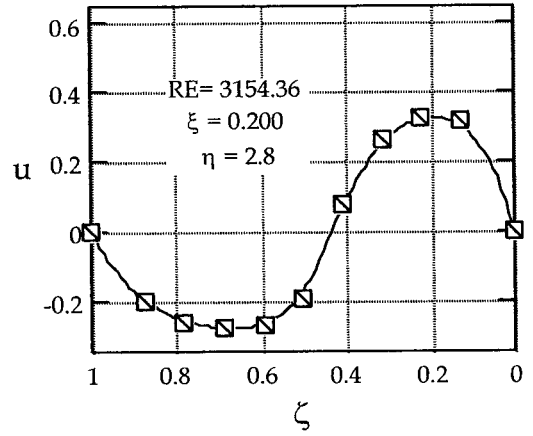
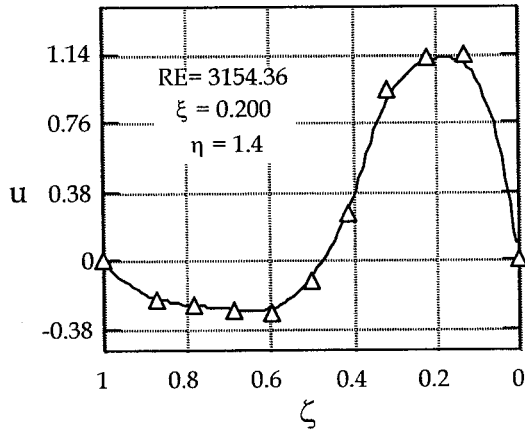


Figure 4.21 – Schematic of flow regions in the source flow

The generated vortex partially blocks part of the gap entrance of the upper disc. This causes a convergence of the streamlines (marked by an increase in the flow velocity in the opposite side) which is evident in the data for $\eta = 1.4$ to 5.6 (see Fig. 4.22). The static pressure responds by a sudden drop. Depending on prevailing conditions, the flow may re-attach further down-stream. The cross-sectional area in a source-flow increases along the stream and the fluid experiences a deceleration, which is accompanied by a pressure increase in Regions II and III.

From figures 4.22 (a)-(e), it is evident that for a smaller gap ratio ($\xi = 0.200$), the separation zone is smaller and the phenomenon of reattachment seems to take place rapidly (at $\eta = 4.2$). As the gap increases ($\xi = 0.400$), the size of the separation bubble increases up to the radius of $\eta = 5.6$, while the flow reattaches at $\eta = 7.0$. Raal [26] observed that the size of the separation bubble increases as the Reynolds number increases. This was not confirmed by the present work. At the radial location of $\eta = 4.2$

for $\xi = 0.200$, and $\eta = 7.0$ for $\xi = 0.400$, the velocity profiles seem to approach laminar-like profiles.



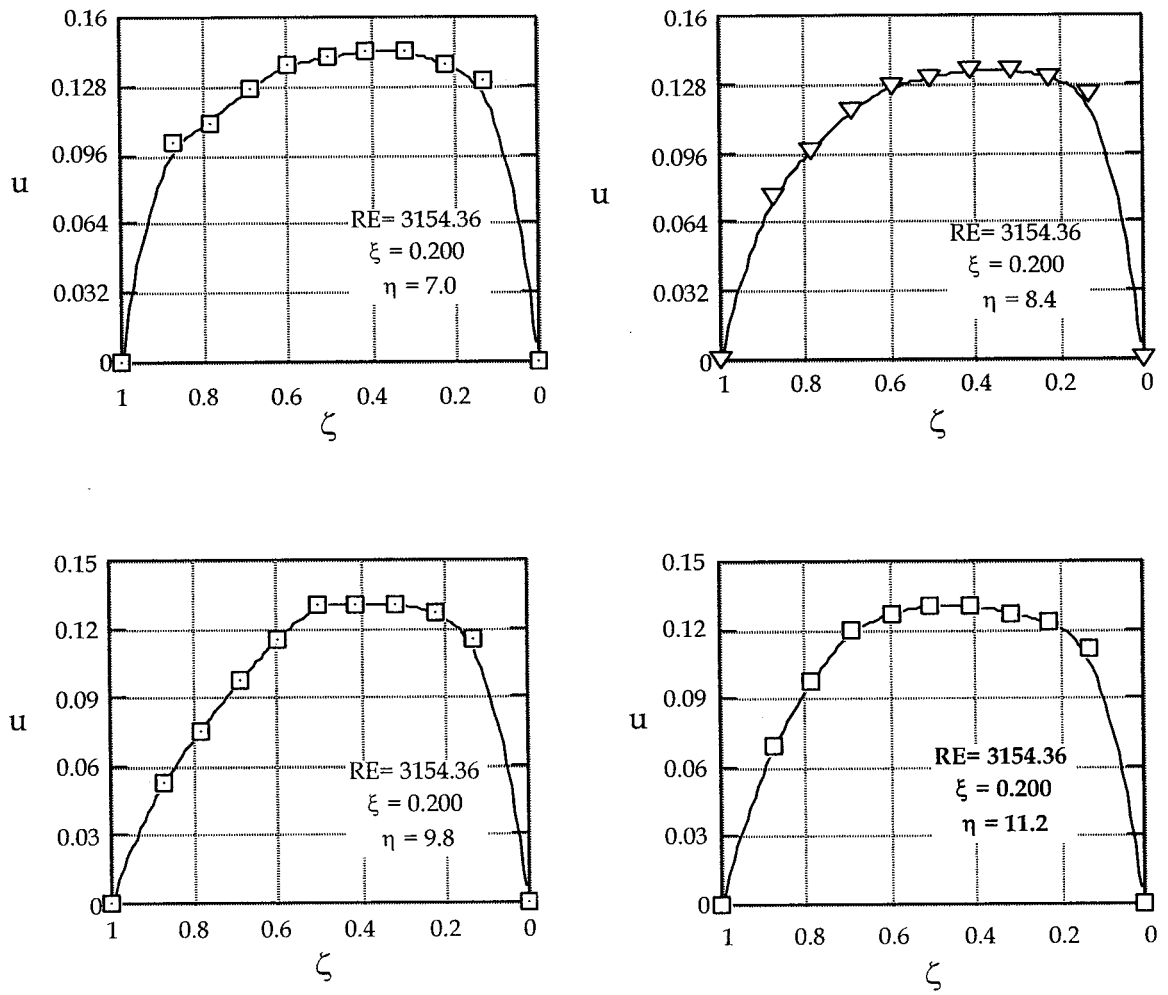
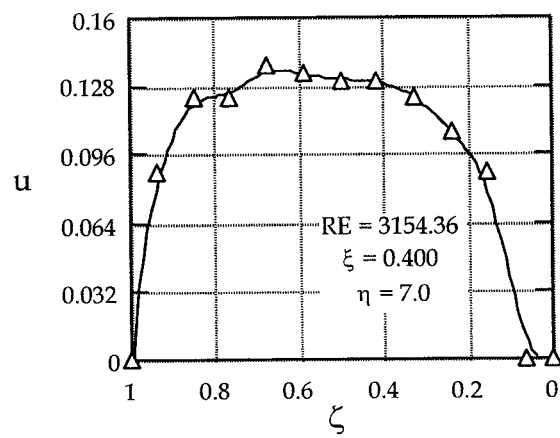
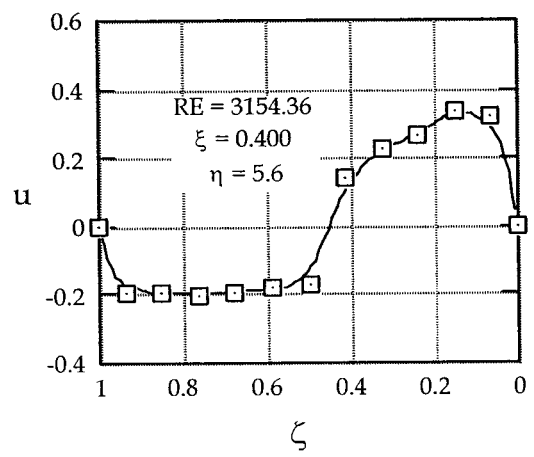
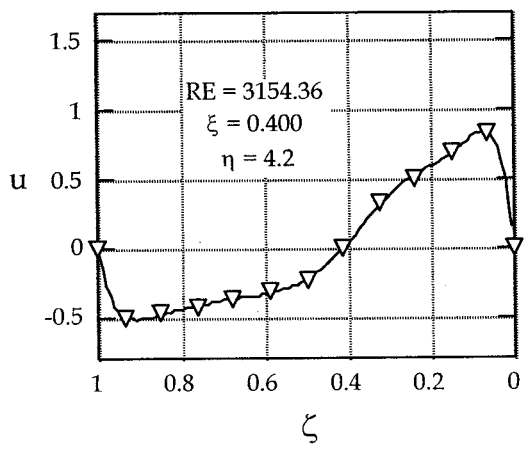
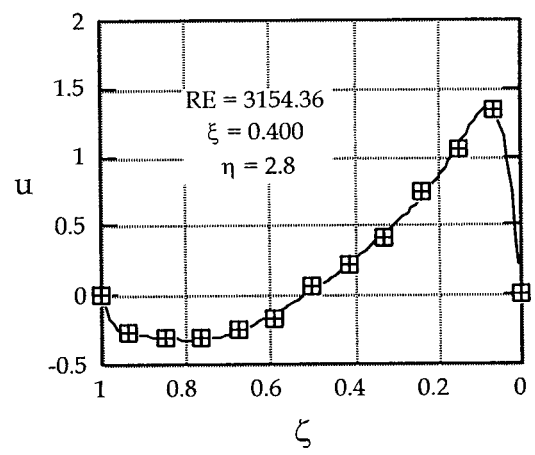
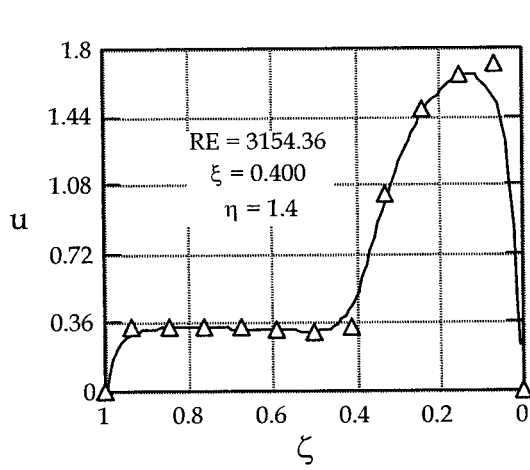


Figure 4.22 (a) – Radial velocity profiles for $H = 0.25$ in and $Q = 20$ CFM



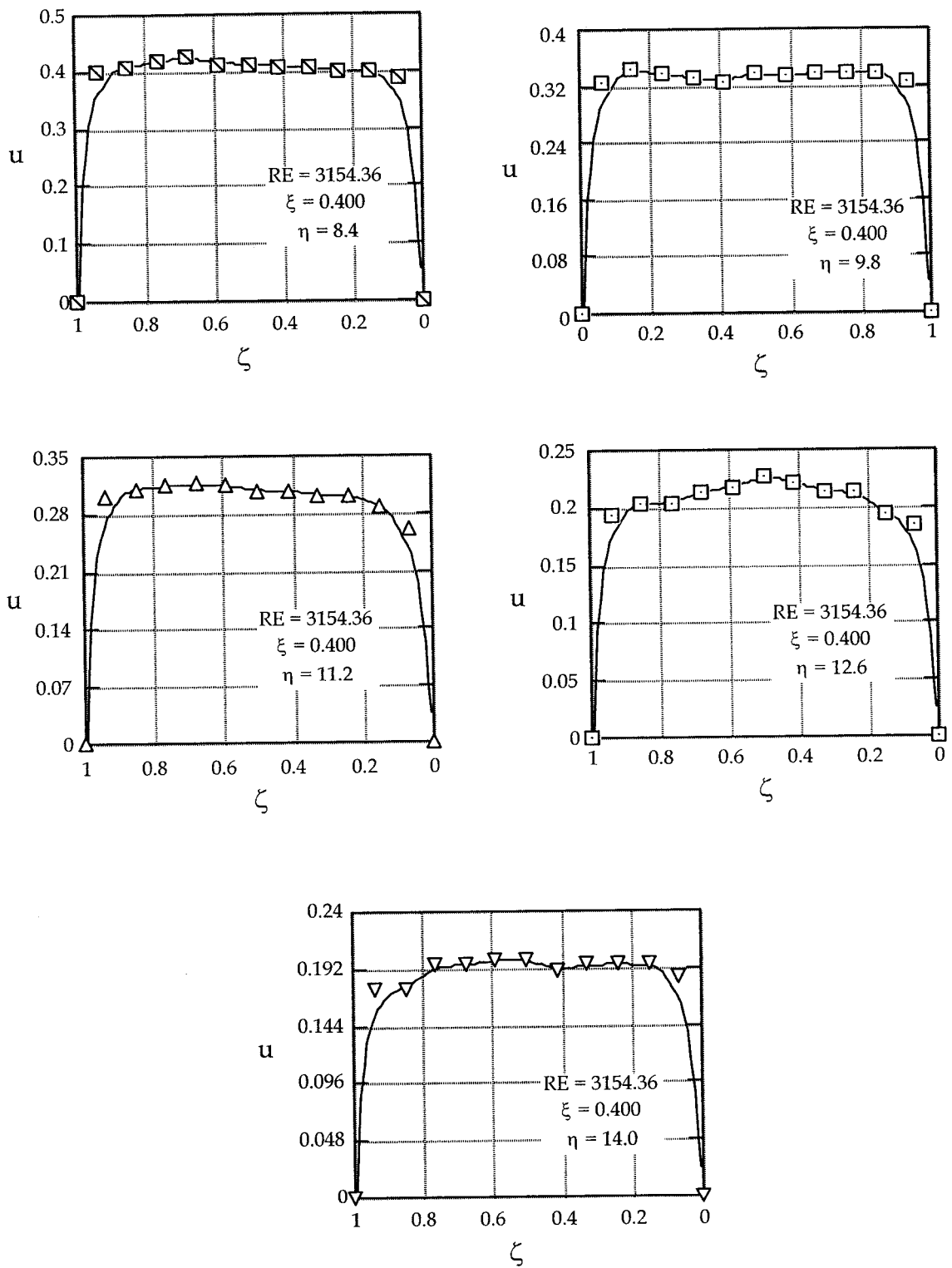
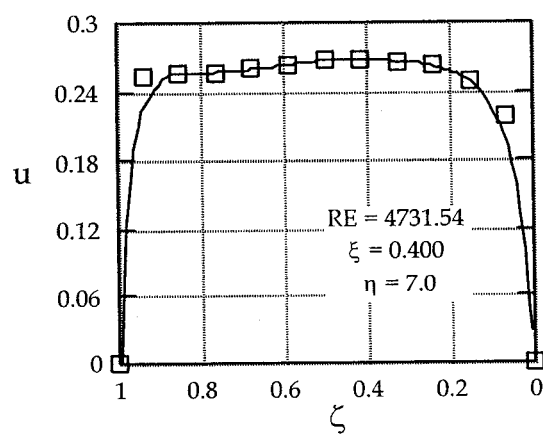
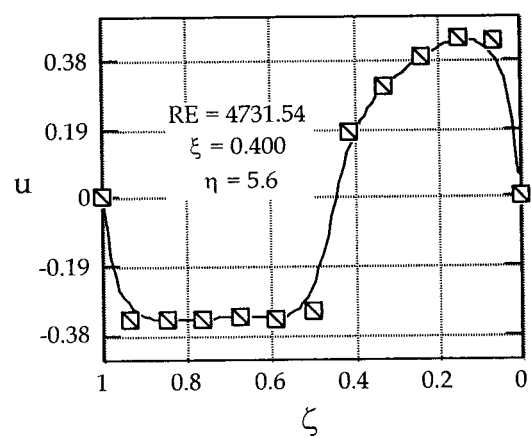
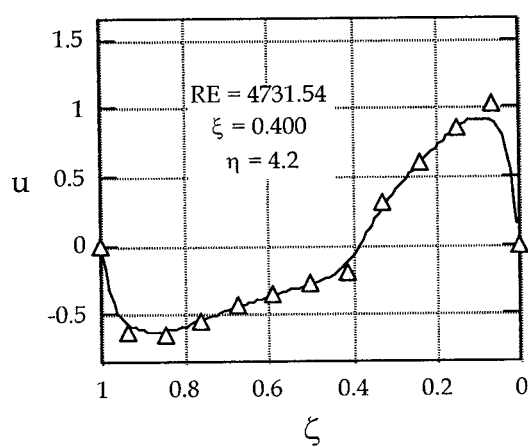
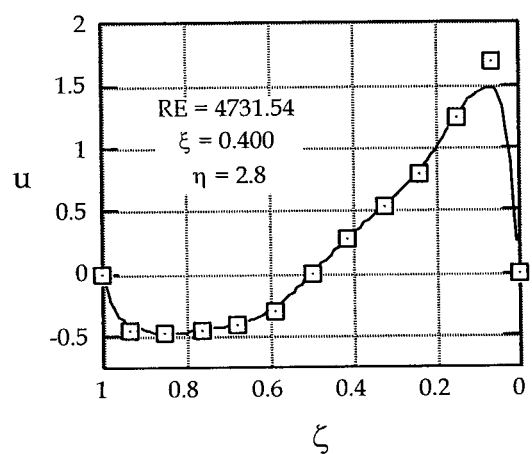
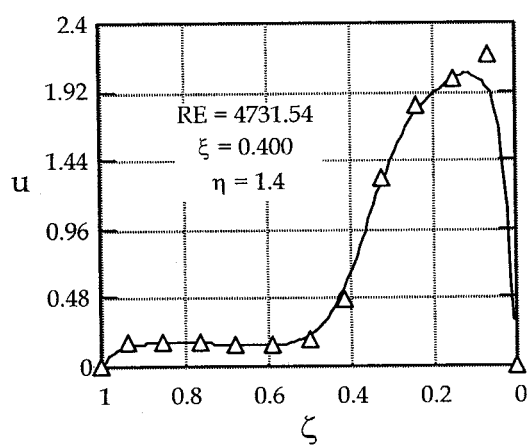


Figure 4.22 (b) – Radial velocity profiles for $H = 0.5$ in and $Q = 20$ CFM



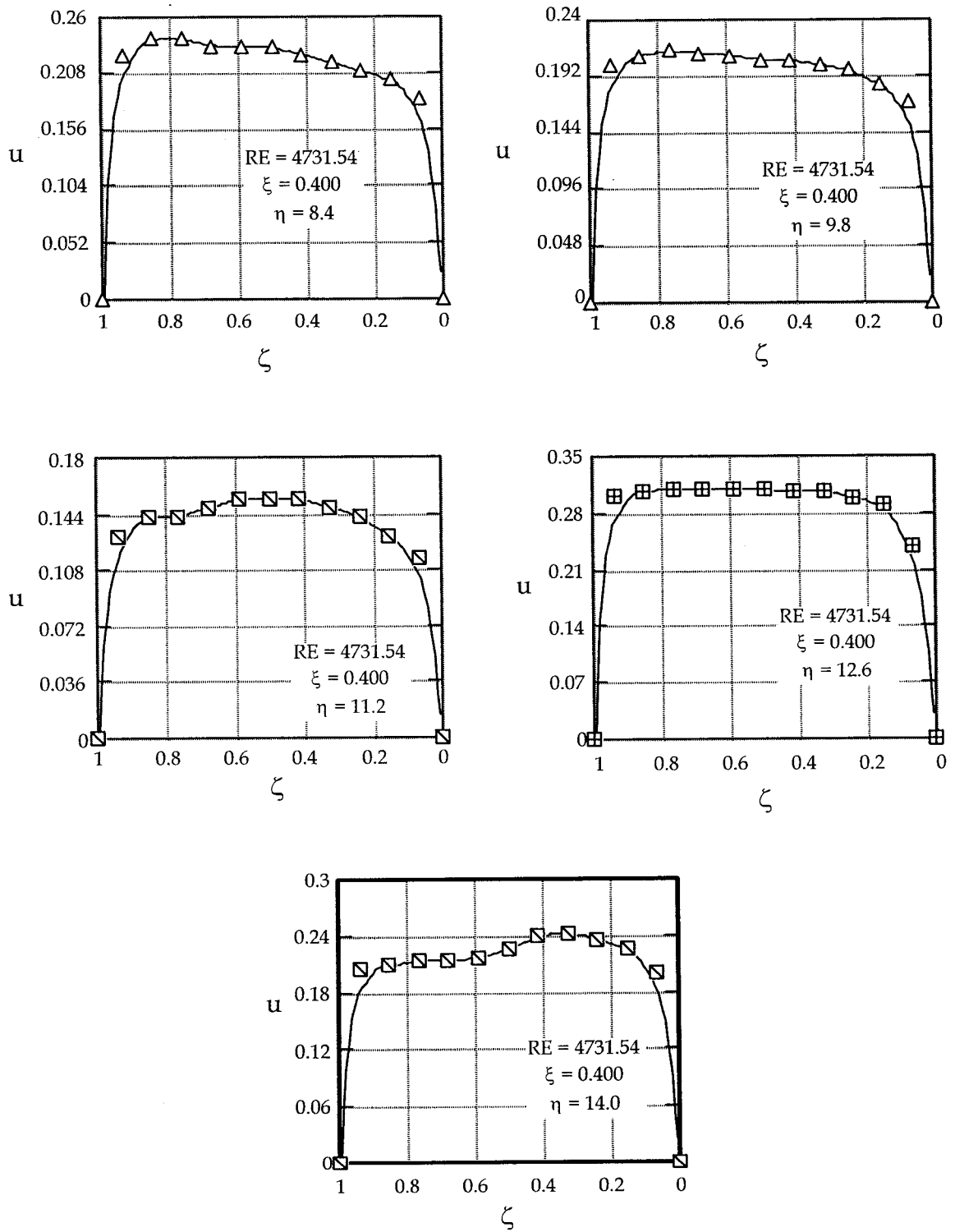
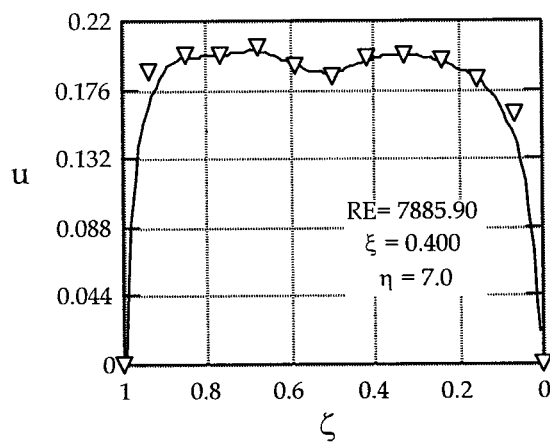
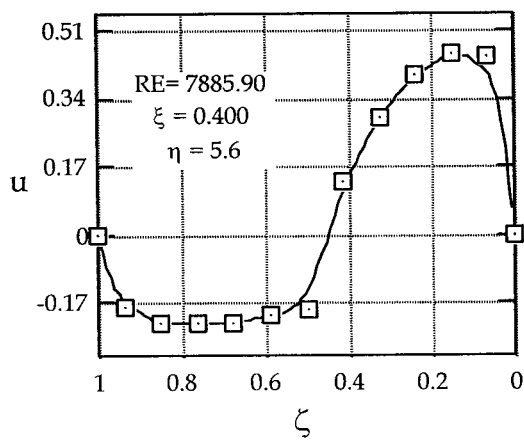
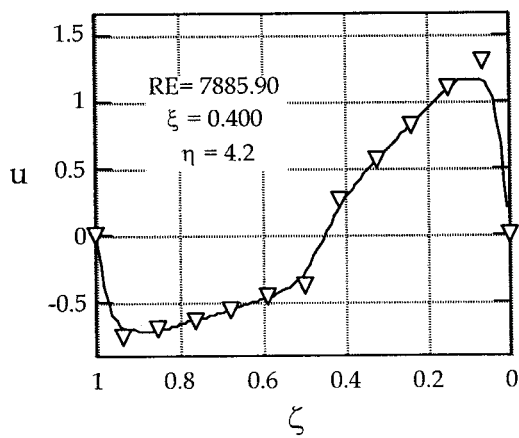
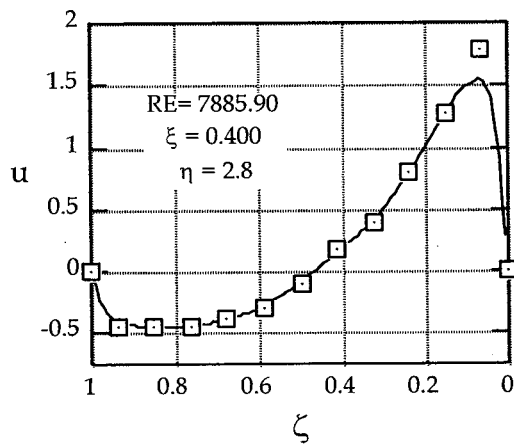
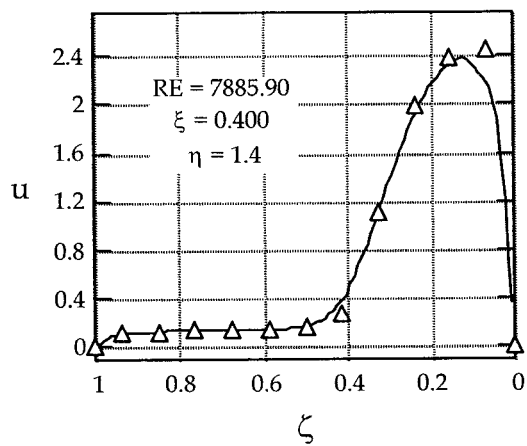


Figure 4.22 (c) – Radial velocity profiles for $H = 0.5$ in and $Q = 30$ CFM



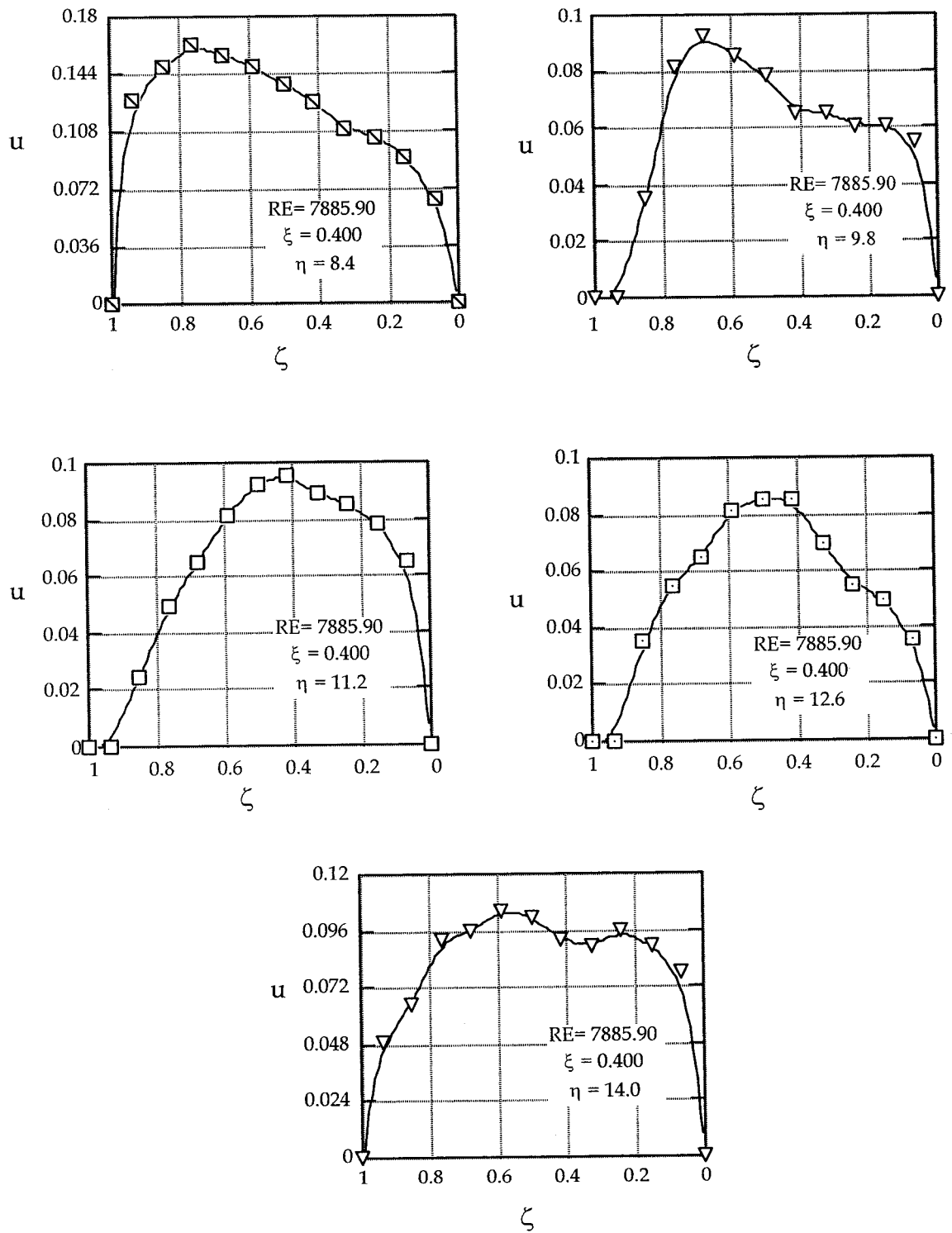
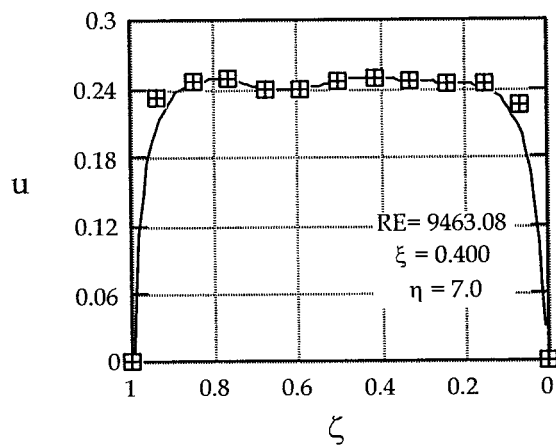
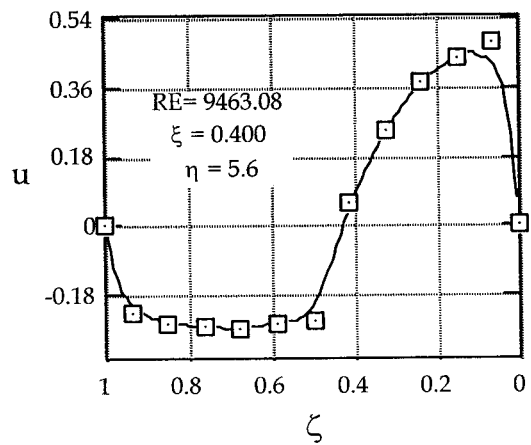
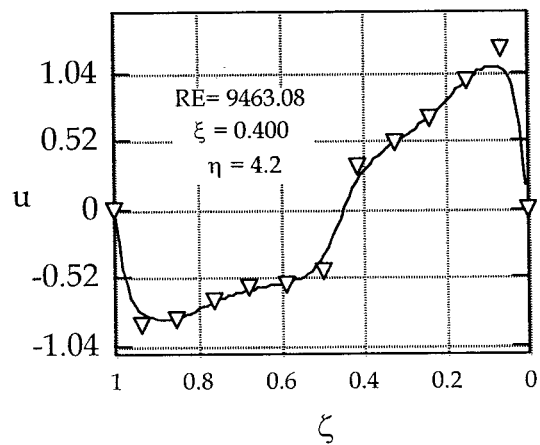
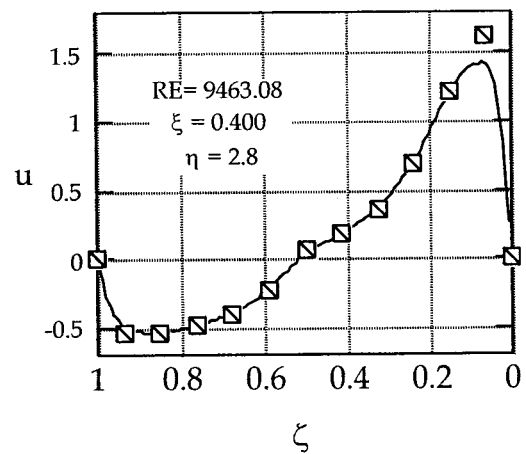
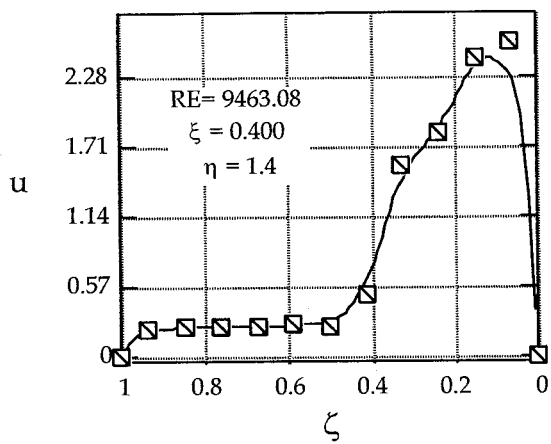


Figure 4.22 (d) – Radial velocity profiles for $H = 0.5$ in and $Q = 50$ CFM



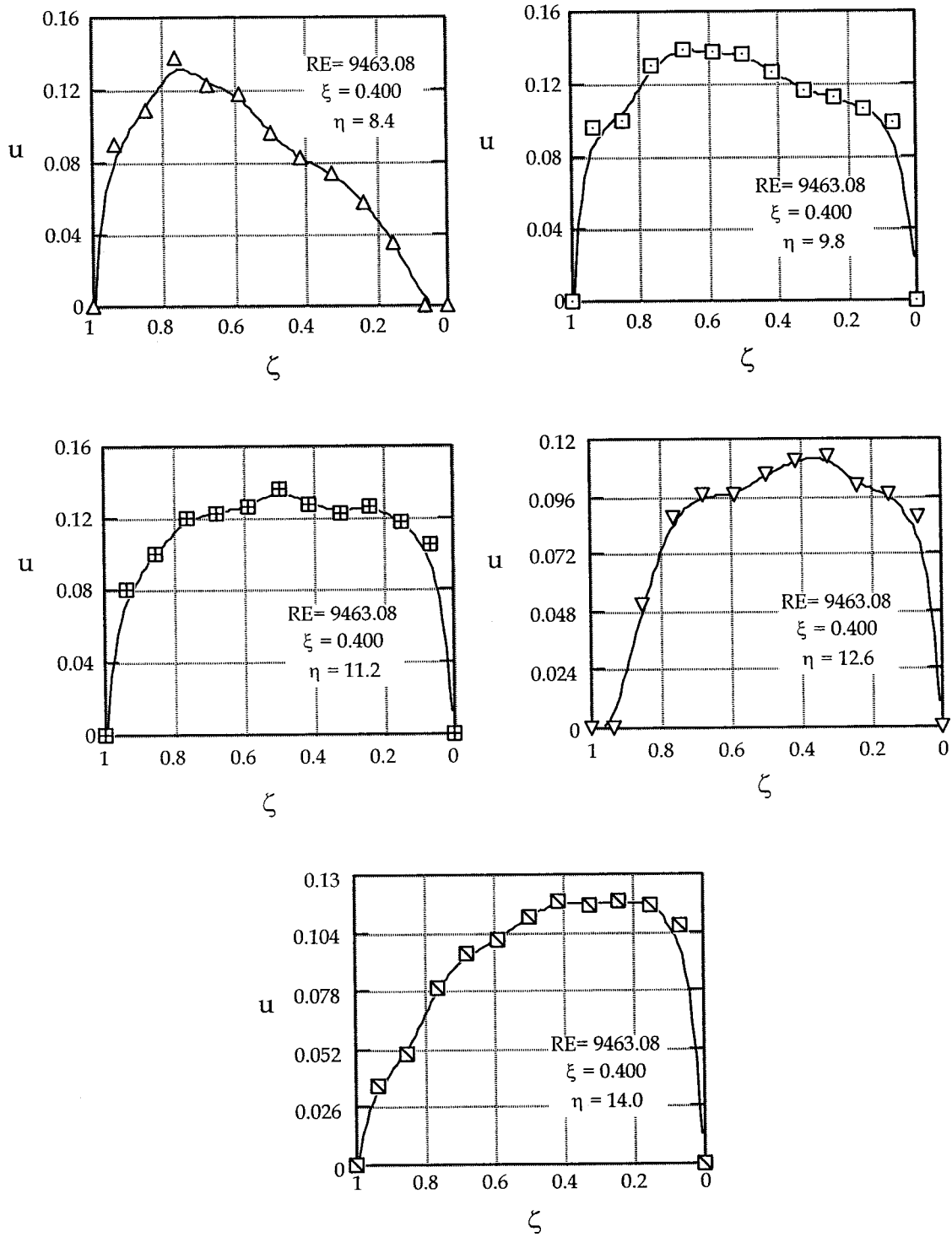


Figure 4.22 (e) – Radial velocity profiles for $H = 0.5$ in and $Q = 60$ CFM

This implies that relaminarization or a reverse transition from turbulent to laminar flow has probably taken place. Bakke et al [25], showed that for $\xi = 0.00909$ and $\xi = 0.01363$, the turbulence intensity remains high even though the velocity profiles have approached a parabolic distribution. The same observation was made by Ervin et al [30] who measured high turbulent intensities at the discs' exit. He also illustrated that the velocity profiles near the inlet display unsteadiness, and at small radii (close to entrance), the velocities are skewed towards the lower disc. The *vena contracta* effects were not reported in [30]. Ervin et al [30] also approximated the velocity profiles with parabolic distributions close to the exit, thus pointing towards the reverse transition trend from the turbulent to the laminar flow. Moller [18] also supported that for relaminarization to occur the initial flow Reynolds number must exceed the lower critical Reynolds number for pipe flow, namely the value of 2000. The inlet Reynolds number pertaining to the present experimental work varies in the range of 3154.36 to 9463.31. This confirms that the phenomenon of relaminarization has occurred, as observed from the velocity profiles. The effects of instability caused in the flow by the adverse pressure gradient of the decelerating flow, the separation, and the still present turbulence, are apparent in the radial velocity profiles of fig.4.22 (a) to (e).

The opposite behavior of the pressure along the flow direction, in comparison to the sink-flow, is observed in Fig. 4.23 (a) and (b). However, , there is a special flow phenomenon that occurs here due to adverse pressure gradient, which is absent in the monotonically accelerating sink-flow. In this case, fluid particles near the walls are moving within an adverse pressure gradient. Due to the no-slip condition, the particles

touching the walls will affect the fluid layers above or below them, and cause them to have a very low momentum.

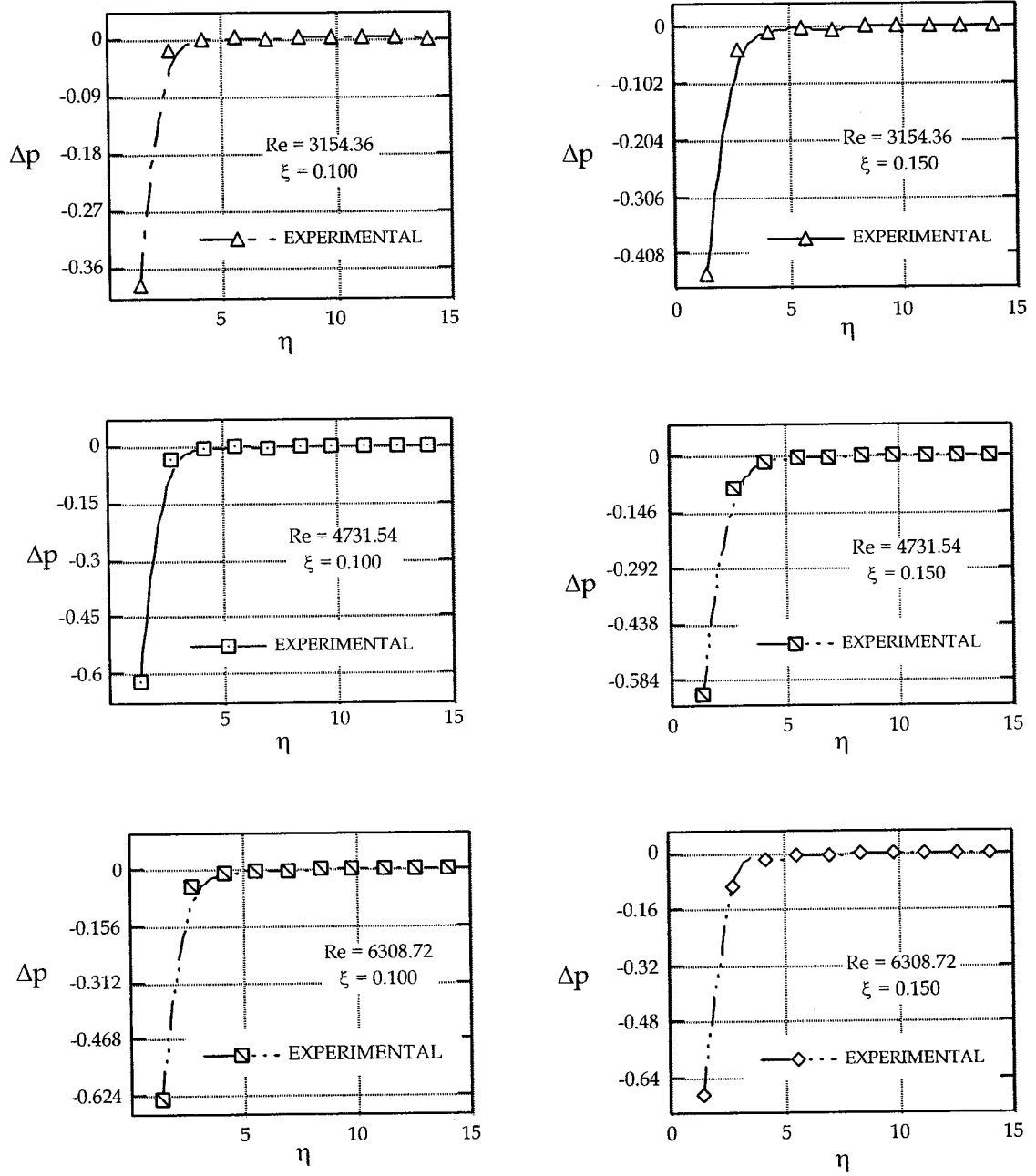


Figure 4.23 (a) – Static pressure profiles for non-swirling outflow and for $\xi = 0.1, 0.15$

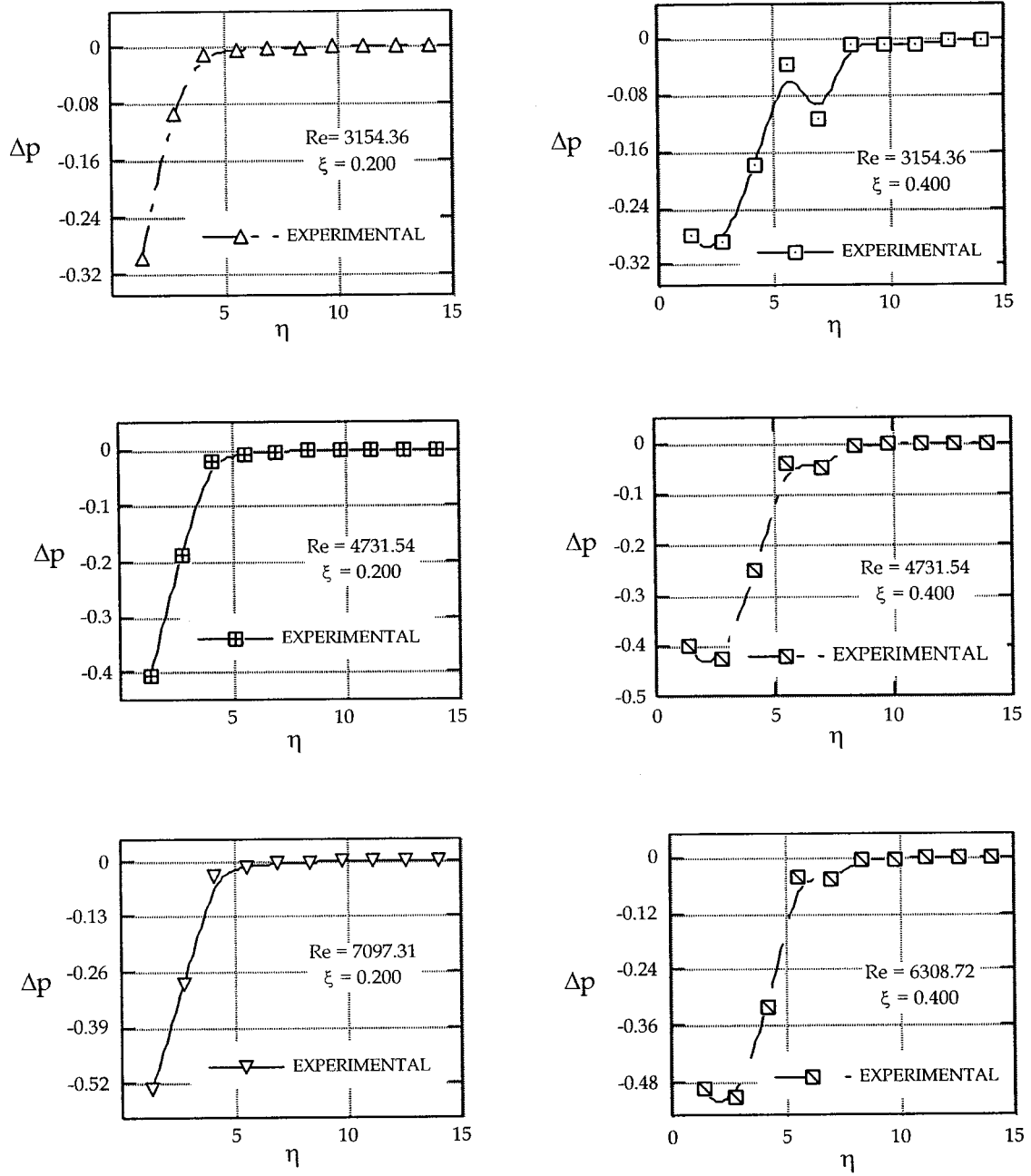


Figure 4.23 (b) – – Static pressure profiles for non-swirling outflow and for $\xi = 0.2, 0.4$

The flow particles are being slowed down, and thus do not have the adequate momentum needed to resist the increasing pressure gradient. As a result, those fluid layers will be stopped and turned around to develop a reverse flow region.

For a given Reynolds number and gap ratio, the flow may develop a stagnation point at a specified radius downstream giving rise to a flow reversal near the wall. The latter action produces a series of alternating vortices that are evident in the visualization experiments of Mochizuki et al [28]. Initially, the relatively powerful positive mid-channel velocity drags the fluid particles underneath, towards the adverse pressure gradient, forcing them to move closely to the discs. However, whilst the centerline velocity gradually declines, it reaches a value, which is insufficient to pull the entire flow field in the η -axis along the positive radial direction. The two competing actions, i.e. the pressure and viscous effects, will act together to oppose the flow by decreasing the momentum. This causes deceleration, drives the wall derivative of the velocity ($\partial u / \partial \eta$) to zero, and eventually sets up a back-flow downstream.

As soon as the opposite of the main flow appears, the particles of the outwards flowing current will be deflected towards the center of the gap and will form a recirculating zone beyond the separation point. The flow past the separation point is fully two-dimensional. As the main flow detaches from the walls, the formed recirculation zone will cause an aerodynamic blockage. In order to satisfy continuity, the fluid will adjust to the new condition by increasing the centerline velocity to a value that again is sufficient to drag the layers below. The latter will then force the boundaries of the recirculatory motion to reduce, thus giving it the appearance of a vortex. Therefore, the expected local pressure depression, seen in the experimental results of Fig. 4.23, may

mark its presence in this region. Since the probable vortex is not detected by the probe in the velocity profile at $\eta = 7.0$, more investigation for this case is needed. This local pressure depression is present for all gaps at the same radial location, even though it is not as evident in the smaller gaps as it is for $\xi = 0.4$. Many features of the present problem also appear analogous to the classical Jeffrey-Hamel flow field between two inclined planes.

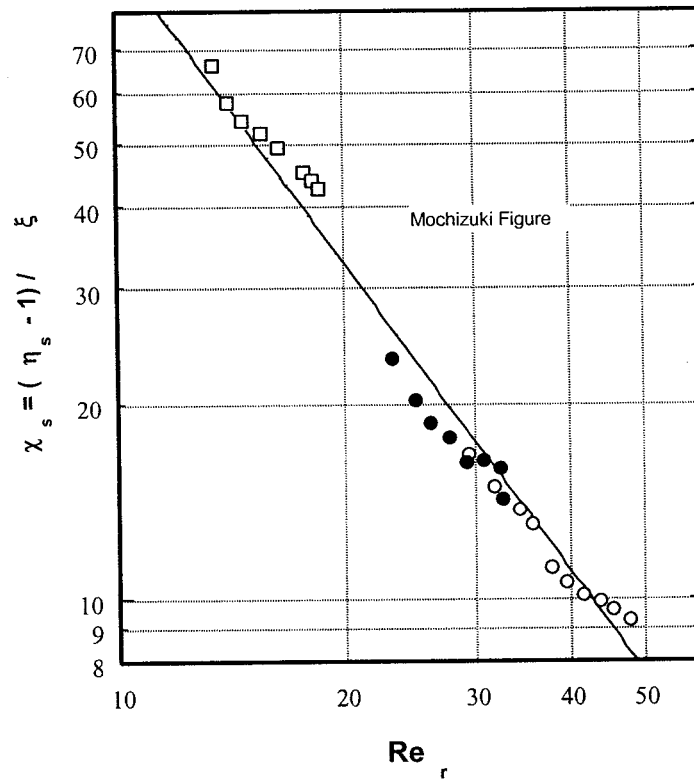


Figure 4.24 Test results for the separation point versus Reynolds number [28]

According to the visualization experiments of Mochizuki et al [28] the case under consideration should produce a flow motion that is detached from both discs along the entire diameter of the discs, see Fig. 4.24. However, this type of behaviour is not present

in our results. Instead, our data indicate that there will be a *vena contracta* near the inlet and that the flow will slowly reattach downstream ($\eta = 7.0$), reverting to laminar-like conditions. The conditions may develop a vortex that produces the pressure dip mentioned before. Yet, it is also important to note that for our case, the inlet Reynolds number is well beyond the interval of the previous experimental study.

II. Swirling Flow

The importance of study of the swirling inlet flow to a diverging channel between the discs lies in the many applications it can be found, such as, centrifugal compressors and gas turbine combustors, which require swirling in the flow entering them in order to enhance mixing in the combustion process. As previously mentioned, this kind of flow possesses several complexities, which are absent not only in its accelerating counterpart, but also in the decelerating no-swirling flow. The complexity of the entire affair is further exacerbated by the introduction of a centrifugal force field via the imposition of swirl at the inlet. Guide vanes in the radial direction with a 30-degree swirl angle, controlled the strength of the swirl.

The variation of the static pressure along the radius is shown in Fig. 4.25 (a) and (b). Firstly, it was observed that because the flow does not have to negotiate the entrance corner, there is no indication of a *vena contracta*. Therefore, the recirculation region that existed at zone I (figure 4.21) for the non-swirling case is now vanished. Moreover, because the fluid is guided through the vanes prior to its entry in the diffuser, the tangential velocity component comes into the picture and give rise to centrifugal effects.

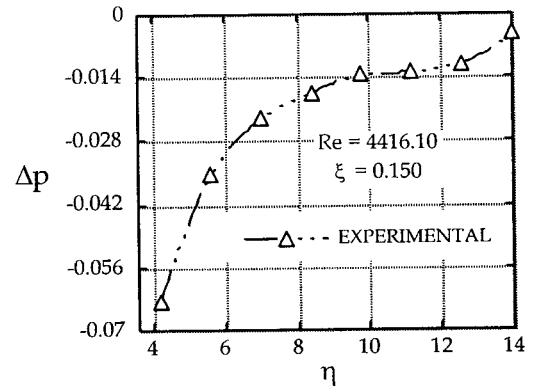
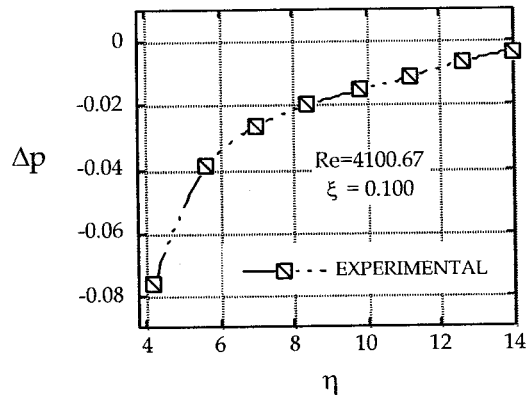
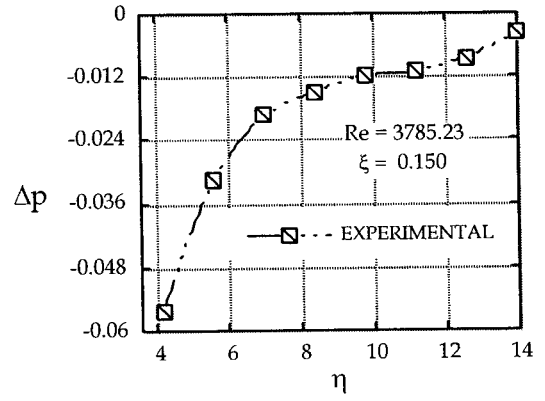
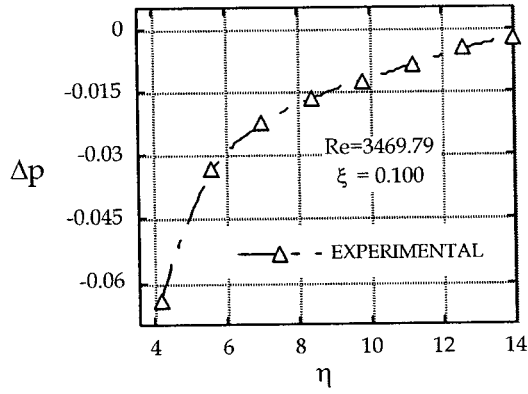
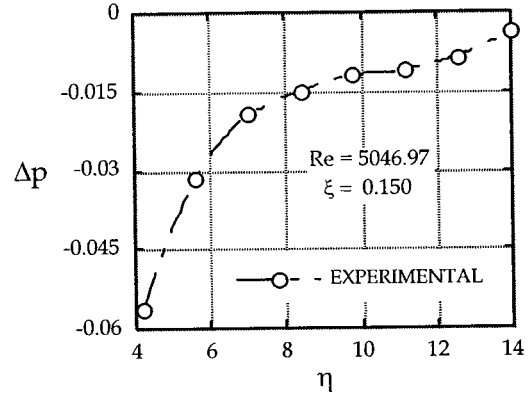
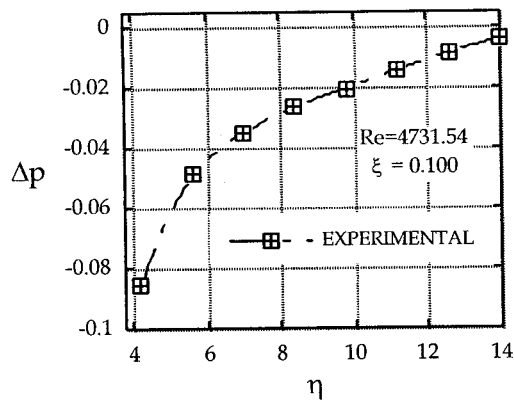


Figure 4.25 (a) – Static pressure profiles for swirling outflow and $\xi = 0.1, 0.15$

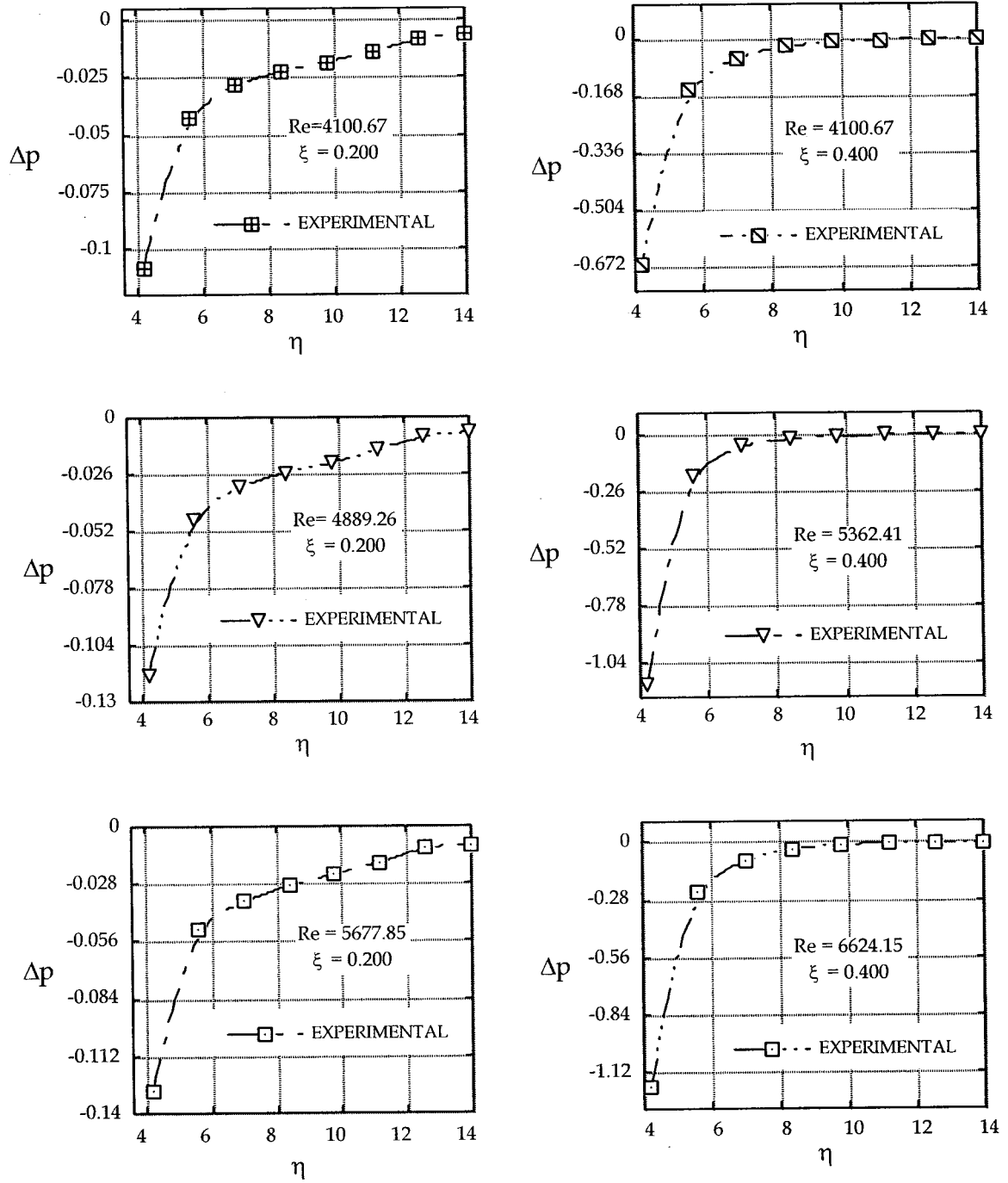


Figure 4.25 (b) – Static pressure profiles for swirling outflow and $\xi = 0.2, 0.4$

In addition, we detected that the pressure dip that was observed at $\eta \approx 7.0$ is no longer present. This further indicates that the manifestation of the pressure dip is due to the existence of a vortex. Consequently, the centrifugal force acting along the flow direction has eliminated the second recirculation zone, and has introduced a stabilizing effect on the static pressure distribution.

In its effort to balance the centrifugal forces, the increasing pressure gradient due to the decelerating flow, takes more time to recover. For the highest gap $\xi=0.4$, the static pressure profile approaches faster the one corresponding to the non-swirling pressure distribution. As the gap decreases, the pressure recovery occurs at a slower pace, as it approaches the non-swirling one for the same flow-rate.

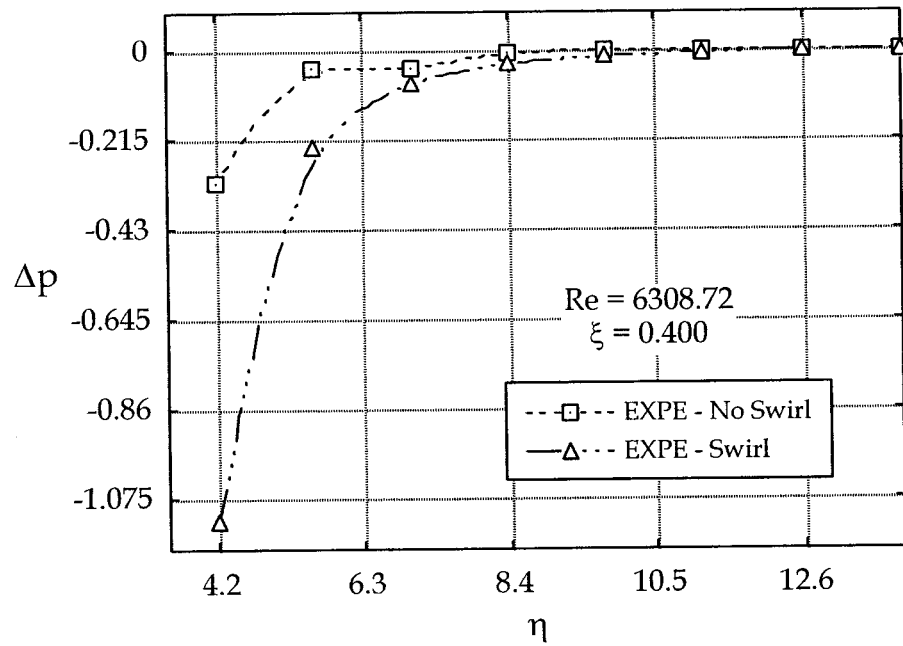


Figure 4.26 - Comparison of static pressure for swirling and non-swirling outflow

A typical static pressure profile for a swirling source flow is presented in Fig. 4.26. In this case, the trend of pressure recovery is similar to the one in the previous condition (i.e. source flow without swirl). However, the values of static pressure are lower in this case (more dramatic), owing to the presence of the centrifugal force. Because the effective area is increasing, the velocity drops and the radial outflow does not have enough momentum to penetrate the centrifugal field. As a consequence, the adverse pressure gradient that is being developed interacts with the centrifugal forces.

Moreover, the static pressure behavior in the swirling outflow could be attributed to two mechanisms: (i) due to the reduction of the tangential velocity component in the diverging channel with increasing radius, and (ii) due to the modification in the way the

radial pressure recovers as a result of the coupling between the radial and the tangential components. The degree of interaction between the aforementioned flow mechanisms is not fully known.

For certain conditions ($\xi=0.150$) we have identified a peculiar consistent behavior that does not appear in the other cases. For the previously mentioned situations the increase of the pressure gradient (at about 10 inlet pipe diameters) is more pronounced than usual. A local pressure decrease is dictated by the experiments near the exit for all the Reynolds numbers. We are not certain what triggers this pressure drop. We feel that more investigation is needed to shed light on this behavior.

CONCLUSIONS

The analytical and experimental investigation on the flows developed within the gap of two discs was presented in this thesis. Two distinct flows were manifested, one where the flow is admitted via the periphery of the discs (inflow), and the other where the flow enters through a centrally located hole (outflow). The effects of swirl on both cases were also examined. Based on the aforementioned analysis (presented in chapters one through four), the following conclusions were drawn:

1). Inflow

1. A theory was developed for a laminar, steady, axisymmetric, and incompressible flow between two closely - spaced discs. The entrance and exit effects were not taken into consideration.
2. The analytical development provided expressions for the radial and tangential velocity as well as for the static pressure distribution. It was shown that the radial velocity depends only on the radial location and Reynolds number. For the swirling flow cases, the static pressure was found to depend on the radial location, Reynolds number and the vortex strength.
3. The theory was found to be a good approximation for the present experimental results. It was also validated with previous findings.

4. The experimental findings displayed all the characteristics of the accelerating flow. As the flow moved towards a decreasing area, it started accelerating and the radial profiles became more flat at the mid section, thus approximating the potential solution at the center. As the fluid started to approach the exit, a discrepancy was observed in the velocity profiles as the fluid sensed the upcoming turn and tried to negotiate it. The asymmetry in the profiles was more pronounced for the lowest Reynolds number and gap.

- i.) The static pressure exhibited an increasing drop towards the flow direction. At the highest gap, as the Reynolds number increased, the drop became more dramatic. At the smaller heights, it was shown that the effect of Reynolds number and gap ratio had a minimal effect on the pressure distribution.
- ii.) For the swirling inflow, as the fluid enters through the periphery, it is immediately confronted by a centrifugal field. As a result, the radial flow moves towards the end-walls to resist opposition and leaves the centrifugal effects to dominate in the mid region.
- iii.) The mid-plane value of the tangential velocity was found to approximate the potential vortex. This was confirmed by comparing present theory with previous experimental findings.
- iv.) The analysis approximated well the static pressure measurements for small gap ratios. As the gap increased, a small deviation from theory is observed at the mid region. That could be due to the interaction of the radial flow

and the centrifugal forces. Moreover, the effects of swirl proved to be more dramatic on the static pressure distribution.

II). Outflow

1. Analytical expressions were developed for the radial and tangential velocity profiles as well as static pressure distribution.
2. The *vena contracta* effects, as well as the phenomenon of separation, were manifested in the present experimental findings. The flow separates in its attempt to negotiate a 90-degree turn, and thus creates a recirculation zone at the inlet region. This was evident at all heights and Reynolds numbers.
 - i.) For the smaller gap, the separation zone was found to be smaller, and the reattachment of the flow took place more rapidly (compared to the higher gap).
 - ii.) After the reattachment of the flow, the radial velocities approached laminar-like profiles. That indicated that the flow experienced a reverse transition from turbulent to laminar.
3. The decelerating nature of the flow causes an adverse pressure gradient in the flow direction. For the non-swirling outflow a local pressure depression is noticed in the pressure profiles at the radial location of $\eta=7.0$, making its presence more apparent at the highest gap. The probable cause is the existence of a recirculation zone, which is not manifested in the velocity profiles.
4. For the swirling outflow, the flow does not experience the *vena contracta* effects, thus the recirculation zone at the inlet region is absent.

- i.) The local pressure depression previously observed at the no-swirling outflow and at $\eta=7.0$ is also vanished. This justifies our speculation that the probable cause of the pressure dip is the existence of a vortex. Consequently, the centrifugal forces have eliminated the vortex and created a stabilizing effect on the static pressure distribution.
- ii.) The pressure recovery of the swirling outflow resembled the one in the no-swirling outflow. It was detected however that swirl had a drastic effect on the static pressure. A similar conclusion was reached previously for the case of the inflow.

Future Work

Many areas of the present analysis can be further explored to acquire a more complete picture of the flow phenomena. Some of these areas are as follows:

- i. The entrance and exit effects can be incorporated in the investigation. The extent of these regions can be estimated using analytical or numerical tools. The boundary layer behavior for both inflow and outflow can also be explored.
- ii. For the cases of no-swirling inflow and outflow, velocity profiles can be obtained for smaller gaps than the ones presented in the present analysis. For the inflow case experimental data can be obtained in the vicinity of the exit region, while for the outflow case, the observed pressure dip in the static pressure distribution needs to be further investigated.
- iii. For the swirling inflow and outflow, radial and tangential velocity profiles can be obtained in order to establish the interacting mechanism between the two flow components. The effect of various swirl strengths on the radial and tangential velocity profiles, as well as the static pressure distribution could also be addressed.
- iv. Visualization techniques can be employed to quantify the flow, (i.e. Particle Image Velocimetry methodology).
- v. Numerical simulation could also shed light to the occurring phenomena and confirm theory and experiments.

REFERENCES

1. G.Sovran, "Fluid mechanics of internal flow." 1967, Elsevier publishing company, TA 357 S93, pp.39-43.
2. M.J. DeSantis, E.L.Rakowsky, "An experimental investigation of the viscous flow field in a pneumatic vortex rate sensor." (1971), ASME, 70-FLCS-16, pp.1-12.
3. H.D. Murphy, M.Coxon, D.M. McEligot, "Symmetric sink flow between parallel plates." Dec.(1978), Journal of Fluids Engineering, vol.100, pp.477-484.
4. H.D Murphy, F.W. Chambers, D.M McEligot, "Laterally converging flow. Part1. Mean flow." (1983), J. Fluid Mech., vol.127, pp.379-401.
5. P.M. Lee, S. Lin, "Pressure distribution for radial inflow between narrowly spaced discs." Sept. (1985), Journal of Fluids Engineering, vol.107, pp. 338-341.
6. G.H. Vatistas, "Radial flow between two closely placed flat discs." July (1988), Journal AIAA, vol.26, no.7, pp.887-889.
7. G.H. Vatistas, "Radial inflow within two flat discs." July (1990), Journal AIAA, vol.28, no.7, pp.1308-1310.
8. A. Singh, "Theoretical and experimental investigations on inward flow between two discs." (1993), Ph.D thesis, IIT Bombay, India.
9. G. Zitouni, G.H. Vatistas, "Purely accelerating and decelerating flows within two flat discs." (1997), Acta Mechanica, 123, pp. 151-161.
10. W. Ghaly, G.H. Vatistas, "Numerical Solution of the flow between two discs." September (1997), ASME, Proceedings of CIE, Sacramento, California, pp. 1-6.

11. A.Sing, B.D.Vyas, U.S.Powle, "Investigations on inward flow between two stationary discs." Aug.(1999), J.Heat and Fluid flow, vol.20, issue 4, pp.395-401.
12. D.N. Wormley, "An analytical model for the incompressible flow in short vortex chamber." June (1969), Transactions ASME, , pp.264-276.
13. J.M. Savino, E.G.Keshock, "Experimental profiles of velocity components and radial pressure distributions in a vortex contained in a short cylindrical chamber." October (1965), NASA TN D-3072, Library of University of California San Diego, pp.2-32.
14. C.C.K. Kwok, N.D. Thinh, S. Lin, "An investigation of confined vortex flow phenomena." September (1972), Journal of Basic Engineering, Transactions of ASME, pp.689-696.
15. J.H. McGinn, "Observations on the radial flow of water between fixed parallel plates." (1956), Applied Scientific Research, vol.5, pp.255-264.
16. J.L. Livesey, "Inertia effects in viscous flows." (1960), Int. J. Mech. Sci., vol. I, pp. 84-88.
17. P.G. Morgan, A. Saunders, "An experimental investigation of inertia effects in viscous flow." (1960), Int. J. Mech. Sci. Pergamon Press Ltd, vol.2, pp.8-12.
18. P.S. Moller, "Radial flow without swirl between parallel discs." May (1963), Aeronautical Quart., pp.163-185.
19. S. B. Savage, "Laminar radial flow between parallel plates." Dec. 1964, Journal of Applied Mechanics, pp. 594-596.
20. F. Kreith, "Reverse transition in radial source flow between two parallel planes." June (1965), The Physics of Fluids, vol.8, no. 6, pp.1189-1190.

21. J.D. Jackson, G. R. Symmons, "An investigation of laminar radial flow between two parallel discs." (1965), Appl. Scientific Res., Section A, vol.15, pp.59-71.
22. P.S. Moller, "A radial diffuser using incompressible flow between narrowly spaced discs." March (1966), Journal of Basic Engineering, pp.155-162.
23. B.E. Boyack, W. Rice, "An integral solution for the laminar radial outflow of a viscous fluid between parallel stationary discs." Sept.(1970), Journal of Basic Engineering, pp.662-663.
24. T. Kawaguchi, "Entrance loss for turbulent flow without swirl between parallel discs." (1971), Bulletin of the JSME, vol.14, no.70, pp.355-363.
25. E. Bakke, J. F Kreider, F. Kreith, "Turbulent source flow between parallel stationary and co-rotating discs." (1973), J. Fluid Mech., vol.58, part 2, pp. 209-231.
26. J.D. Raal, "Radial source flow between parallel plates." (1978), J. Fluid Mech., vol. 85, part 3, pp.401-416.
27. C. E. Wark, J.F. Foss, "Forces caused by the radial outflow between parallel discs." (1984), Trans. ASME, J. Fluids Eng., 106, 292.
28. S. Mochizuki, W. J. Yang, "Self-sustained radial oscillating flows between parallel discs." (1985), J. Fluid Mech., vol. 154, pp.377-397.
29. Tabatabai M., Pollard A., "Turbulence in radial flow between parallel discs at medium and low Reynolds numbers." (1987), J. Fluid Mech., vol. 185, pp.483-502.

30. Ervin J.S., Suryanarayana N.V., Hon Chai Ng, "Radial turbulent flow of a fluid between two coaxial discs." Dec. (1989), J. Fluids Engineering, vol.111, pp.378-383.
31. J.P. Holman, "Experimental methods for engineers." 1994, McGraw Hill, Inc., 6th edition, p.3, 102.
32. W.F. Hayes, H.G.Tucker, "Theoretical radial pressure distribution for viscous fluid inflow within a thin disc chamber." (1973), National Research Council of Canada, Ottawa, Canada, NRC-CS-51.
33. Koval, P.V. and Michailov, "Velocity and pressure distribution of liquid in a swirl chamber." (1972), Teploenergetika, vol. 19 (2) 25-28, pp.39-.43.

APPENDIX A - DERIVATION OF THE EQUATIONS

Introducing the non-dimensional parameters into the governing equations, we get:

Continuity:

$$\begin{aligned} \frac{1}{r} \frac{\partial}{\partial r} (r V_r) &= 0 \Rightarrow \frac{1}{\eta R_{in}} \frac{\partial}{\partial (\eta R_{in})} (u V_{r_{in}} \eta R_{in}) = 0 \\ \Rightarrow \underbrace{\frac{V_{r_{in}}}{R_{in}}}_{\text{constant}} \frac{1}{\eta} \frac{\partial (\eta u)}{\partial \eta} &= 0 \Rightarrow \frac{1}{\eta} \frac{\partial (\eta u)}{\partial \eta} = 0 \end{aligned} \quad (1)$$

r-momentum:

$$\begin{aligned} u V_{r_{in}} \frac{\partial (u V_{r_{in}})}{\partial (\eta R_{in})} - \frac{(v V_{\theta_{in}})^2}{\eta R_{in}} &= -\frac{1}{\rho} \frac{\partial (p_{(r)} - p_{in})}{\partial (\eta R_{in})} + v \left\{ \frac{1}{\eta R_{in}} \frac{\partial^2 (u V_{r_{in}} \eta R_{in})}{\partial (\zeta h)^2} \right\} \Rightarrow \\ u \frac{V_{r_{in}}^2}{R_{in}} \frac{\partial u}{\partial \eta} - \frac{V_{\theta_{in}}^2}{R_{in}} \frac{v^2}{\eta} &= -\frac{1}{\rho R_{in}} \frac{d(p_{(r)} - p_{in})}{d\eta} + v \left\{ \frac{V_{r_{in}} R_{in}}{R_{in} h^2} \frac{1}{\eta} \frac{\partial^2 (u \eta)}{\partial \zeta^2} \right\} \Rightarrow \\ \text{multiply each term by } \frac{R_{in}}{V_{r_{in}}^2} &\Rightarrow \\ u \frac{\partial u}{\partial \eta} - \frac{R_{in}}{V_{r_{in}}^2} \frac{V_{\theta_{in}}^2}{R_{in}} \frac{v^2}{\eta} &= -\frac{R_{in}}{\rho V_{r_{in}}^2 R_{in}} \frac{d(p_{(r)} - p_{in})}{d\eta} + \frac{R_{in}}{V_{r_{in}}^2} \frac{V_{r_{in}} R_{in}}{R_{in} h^2} v \left\{ \frac{1}{\eta} \frac{\partial^2 (u \eta)}{\partial \zeta^2} \right\} \Rightarrow \\ u \frac{\partial u}{\partial \eta} - s^2 \frac{v^2}{\eta} &= -\frac{d(\Delta p)}{d\eta} + \underbrace{\frac{v}{V_{r_{in}} h}}_{=\frac{1}{\text{Re}}} \underbrace{\frac{R_{in}}{h}}_{=\frac{1}{\xi}} \left\{ \frac{1}{\eta} \frac{\partial^2 (u \eta)}{\partial \zeta^2} \right\} \Rightarrow \\ u \frac{\partial u}{\partial \eta} - s^2 \frac{v^2}{\eta} &= -\frac{d(\Delta p)}{d\eta} + \frac{1}{\text{Re}_r} \left\{ \frac{1}{\eta} \frac{\partial^2 (u \eta)}{\partial \zeta^2} \right\} \end{aligned} \quad (2)$$

θ -momentum:

$$uV_{r_{in}} \frac{\partial(\eta R_{in} v V_{\theta_{in}})}{\partial(\eta R_{in})} = v \left\{ \eta R_{in} \frac{\partial}{\partial(\eta R_{in})} \left[\frac{1}{\eta R_{in}} \frac{\partial(\eta R_{in} v V_{\theta_{in}})}{\partial(\eta R_{in})} \right] + \frac{\partial^2(\eta R_{in} v V_{\theta_{in}})}{\partial(\zeta h)^2} \right\} \Rightarrow$$

$$\frac{V_{r_{in}} R_{in} V_{\theta_{in}}}{R_{in}} \frac{u \partial(\eta v)}{\partial \eta} = v \left\{ \eta \frac{\partial}{\partial \eta} \left[\frac{R_{in}}{R_{in}^2} \frac{V_{\theta_{in}}}{\eta} \frac{\partial(\eta v)}{\partial \eta} \right] + \frac{R_{in} V_{\theta_{in}}}{h^2} \frac{\partial^2(\eta v)}{\partial \zeta^2} \right\} \Rightarrow$$

$$V_{r_{in}} V_{\theta_{in}} \frac{u \partial(\eta v)}{\partial \eta} = v \left\{ \eta \frac{\partial}{\partial \eta} \left[\frac{R_{in}}{R_{in}^2} \frac{V_{\theta_{in}}}{\eta} \frac{\partial(\eta v)}{\partial \eta} \right] + \frac{R_{in} V_{\theta_{in}}}{h^2} \frac{\partial^2(\eta v)}{\partial \zeta^2} \right\} \Rightarrow$$

$$\frac{u \partial(\eta v)}{\partial \eta} = \frac{v}{V_{r_{in}}} \left\{ \eta \frac{\partial}{\partial \eta} \left[\frac{1}{R_{in}} \frac{1}{\eta} \frac{\partial(\eta v)}{\partial \eta} \right] + \frac{R_{in}}{h^2} \frac{\partial^2(\eta v)}{\partial \zeta^2} \right\} \Rightarrow$$

$$\frac{u \partial(\eta v)}{\partial \eta} = \frac{v R_{in}}{V_{r_{in}} h^2} \left\{ \frac{h^2}{R_{in}^2} \eta \frac{\partial}{\partial \eta} \left(\frac{1}{\eta} \frac{\partial(\eta v)}{\partial \eta} \right) + \frac{\partial^2(\eta v)}{\partial \zeta^2} \right\} \Rightarrow$$

$$\frac{u \partial(\eta v)}{\partial \eta} = \left(\frac{v}{V_{r_{in}} h} \right) \frac{R_{in}}{h} \left\{ \underbrace{\xi^2 \eta \frac{\partial}{\partial \eta} \left(\frac{1}{\eta} \frac{\partial(\eta v)}{\partial \eta} \right)}_{=0; \xi^2 \ll 1} + \frac{\partial^2(\eta v)}{\partial \zeta^2} \right\} \Rightarrow$$

$$\frac{u \partial(\eta v)}{\partial \eta} = \frac{1}{\text{Re}_r} \frac{\partial^2(\eta v)}{\partial \zeta^2} \quad (3)$$

Case 1: Inflow and Swirl

From the continuity equation (eq.1), we get:

$$\frac{1}{\eta} \frac{\partial(u\eta)}{\partial\eta} = 0 \Rightarrow \frac{\partial(u\eta)}{\partial\eta} = 0. \Rightarrow u\eta = \Phi(\zeta) \Rightarrow u = \frac{\Phi(\zeta)}{\eta}$$

Equation 2 is linearized by using:

$$u \cong -\frac{1}{\eta} \quad (\text{for inflow})$$

$$\stackrel{(2)}{\Rightarrow} u \frac{\partial u}{\partial\eta} - s^2 \frac{v^2}{\eta} = -\frac{d(\Delta p)}{d\eta} + \frac{1}{\text{Re}_r} \left\{ \frac{1}{\eta} \frac{\partial^2(u\eta)}{\partial\zeta^2} \right\}$$

$$\left(-\frac{1}{\eta} \right) \frac{\partial}{\partial\eta} \left(\frac{\Phi(\zeta)}{\eta} \right) - s^2 \frac{v^2}{\eta} = -\frac{d(\Delta p)}{d\eta} + \frac{1}{\eta \text{Re}_r} \left\{ \frac{\partial^2(\Phi(\zeta))}{\partial\zeta^2} \right\} \Rightarrow$$

$$\left(-\frac{1}{\eta} \right) \left(-\frac{1}{\eta^2} \right) \Phi(\zeta) - s^2 \frac{v^2}{\eta} = -\frac{d(\Delta p)}{d\eta} + \frac{1}{\eta \text{Re}_r} \frac{\partial^2 \Phi(\zeta)}{\partial\zeta^2}$$

If we consider the centerline value of the tangential velocity to represent the maximum

value of the centrifugal force in the gap, then $v \rightarrow v_{\max}$:

$$\begin{aligned}
& \left(-\frac{1}{\eta} \right) \left(-\frac{1}{\eta^2} \right) \Phi(\zeta) - s^2 \frac{v^2_{\max}(\eta)}{\eta} = -\frac{d(\Delta p)}{d\eta} + \frac{1}{\eta \operatorname{Re}_r} \frac{d^2 \Phi(\zeta)}{d\zeta^2} \Rightarrow \\
& \left(\int_1^\eta \frac{1}{\eta^3} d\eta \right) \Phi(\zeta) - s^2 \int_1^\eta \frac{v^2_{\max}(\eta)}{\eta} d\eta = -\int_1^\eta \frac{d(\Delta p)}{d\eta} d\eta + \frac{1}{\operatorname{Re}_r} \frac{d^2 \Phi(\zeta)}{d\zeta^2} \int_1^\eta \frac{1}{\eta} d\eta \Rightarrow \\
& \left[-\frac{1}{2\eta^2} \right]_1^\eta \Phi(\zeta) - s^2 \int_1^\eta \frac{v^2_{\max}(\eta)}{\eta} d\eta = -[\Delta p]_1^\eta + \frac{1}{\operatorname{Re}_r} \frac{d^2 \Phi(\zeta)}{d\zeta^2} [\ln(\eta)]_1^\eta \Rightarrow \\
& -\left(\frac{\eta^2 - 1}{2\eta^2} \right) \Phi(\zeta) + \frac{1}{\operatorname{Re}_r} \frac{d^2 \Phi(\zeta)}{d\zeta^2} \ln(\eta) = \Delta p(\eta) - s^2 \int_1^\eta \frac{v^2_{\max}(\eta)}{\eta} d\eta \Rightarrow \\
& \frac{d^2 \Phi(\zeta)}{d\zeta^2} - \underbrace{\frac{\operatorname{Re}_r}{\ln(\eta)} \frac{(\eta^2 - 1)}{2\eta^2}}_{=\lambda^2} \Phi(\zeta) = \frac{\operatorname{Re}_r}{\ln(\eta)} \Delta p(\eta) - s^2 \frac{\operatorname{Re}_r}{\ln(\eta)} \int_1^\eta \frac{v^2_{\max}(\eta)}{\eta} d\eta \Rightarrow \\
& \frac{d^2 \Phi(\zeta)}{d\zeta^2} - \lambda^2 \Phi(\zeta) = \lambda^2 \left\{ \underbrace{\left(\frac{2\eta^2}{(\eta^2 - 1)} \right) \Delta p(\eta)}_{=\Delta \Pi(\eta)} - \frac{2s^2 \eta^2}{(\eta^2 - 1)} \int_1^\eta \frac{v^2_{\max}(\eta)}{\eta} d\eta \right\} \Rightarrow \\
& \frac{d^2 \Phi(\zeta)}{d\zeta^2} - \lambda^2 \Phi(\zeta) = \lambda^2 \underbrace{\left\{ \Delta \Pi(\eta) - \frac{2s^2 \eta^2}{(\eta^2 - 1)} \int_1^\eta \frac{v^2_{\max}(\eta)}{\eta} d\eta \right\}}_{=\Delta \Xi(\eta)} \\
& \frac{d^2 \Phi(\zeta)}{d\zeta^2} - \lambda^2 \Phi(\zeta) = \lambda^2 \Delta \Xi(\eta) \quad - \quad 2^{nd} \text{ non-homogeneous O.D.E} \quad (4)
\end{aligned}$$

Where,

$$\lambda^2 = \frac{(\eta^2 - 1) \operatorname{Re}_r}{2\eta^2 \ln(\eta)} \quad , \quad \Delta \Pi(\eta) = \frac{2\eta^2}{(\eta^2 - 1)} \Delta p(\eta) \quad , \quad \Delta \Xi(\eta) = \Delta \Pi(\eta) - \frac{2s^2 \eta^2}{(\eta^2 - 1)} \int_1^\eta \frac{v^2_{\max}(\eta)}{\eta} d\eta$$

To solve the 2nd order O.D.E, the homogeneous and particular solutions must be considered. Therefore, $\Phi(\zeta)$ will be:

$$\Phi(\zeta) = \Phi(\zeta)_h + \Phi(\zeta)_p$$

To define the particular solution, let $\Phi(\zeta)_p = g\lambda^2 \Delta\Xi(\eta)$, where $g = \text{constant}$

$$\Phi(\zeta)_p' = 0, \Phi(\zeta)_p'' = 0$$

Substitute the particular solution and its derivatives into the 2nd order O.D.E to obtain the final form of the particular solution. Therefore:

$$\Phi(\zeta)_p'' - \lambda^2 \Phi(\zeta)_p = \lambda \Delta\Xi(\eta) \Rightarrow 0 - \lambda^2 g \lambda^2 \Delta\Xi(\eta) = \lambda^2 \Delta\Xi(\eta) \Rightarrow -\lambda^2 g = 1 \Rightarrow g = -\frac{1}{\lambda^2}$$

$$\text{So, } \Phi(\zeta)_p = \underbrace{\left(-\frac{1}{\lambda^2}\right)}_{=g} \lambda^2 \Delta\Xi(\eta) = -\Delta\Xi(\eta)$$

The homogeneous 2nd order O.D.E has real solutions $\Phi(\zeta)_h = Ae^{\lambda\zeta} + Be^{-\lambda\zeta}$. Therefore:

$$\begin{aligned} \Phi(\zeta) &= Ae^{\lambda\zeta} + Be^{-\lambda\zeta} - \Delta\Xi(\eta) = u\eta \Rightarrow \\ Ae^{\lambda\zeta} + Be^{-\lambda\zeta} - \Delta\Xi(\eta) &= u\eta \end{aligned} \quad (5)$$

Apply Boundary Conditions:

$$(i) \ z = 0, \ V_r = 0 \Rightarrow \zeta = 0 \text{ then } u = 0$$

$$(ii) \ z = 2h, \ V_r = 0 \Rightarrow \zeta = 2 \text{ then } u = 0$$

$$(i) \zeta = 0 \quad u = 0$$

$$\stackrel{(5)}{\Rightarrow} Ae^0 + Be^0 - \Delta\Xi(\eta) = 0 \Rightarrow A + B - \Delta\Xi(\eta) = 0 \Rightarrow$$

$$A = \Delta\Xi(\eta) - B$$

$$(ii) \zeta = 2 \quad u = 0$$

$$\stackrel{(5)}{\Rightarrow} Ae^{2\lambda} + Be^{-2\lambda} - \Delta\Xi(\eta) = 0$$

substitute $A = \Delta\Xi(\eta) - B$ in the above equation to solve for B.

$$(\Delta\Xi(\eta) - B)e^{2\lambda} + Be^{-2\lambda} - \Delta\Xi(\eta) = 0 \Rightarrow \Delta\Xi(\eta)e^{2\lambda} - \Delta\Xi(\eta) + Be^{-2\lambda} - Be^{2\lambda} = 0 \Rightarrow$$

$$\Delta\Xi(\eta)[e^{2\lambda} - 1] + B[e^{-2\lambda} - e^{2\lambda}] = 0 \Rightarrow B = \Delta\Xi(\eta) \frac{1 - e^{2\lambda}}{e^{-2\lambda} - e^{2\lambda}}$$

Therefore the constant A will be :

$$A = \Delta\Xi(\eta) - \Delta\Xi(\eta) \frac{1 - e^{2\lambda}}{e^{-2\lambda} - e^{2\lambda}} = \Delta\Xi(\eta) \left[1 - \frac{1 - e^{2\lambda}}{e^{-2\lambda} - e^{2\lambda}} \right] \Rightarrow A = \Delta\Xi(\eta) \left[1 - \frac{1 - e^{2\lambda}}{e^{-2\lambda} - e^{2\lambda}} \right]$$

Replace the constants A and B into eq. (5) to find $\Phi(\zeta)$. Therefore we get:

$$\begin{aligned} \Phi(\zeta) &= Ae^{\lambda\zeta} + Be^{-\lambda\zeta} - \Delta\Xi(\eta) = \Delta\Xi(\eta) \left[1 - \frac{1 - e^{2\lambda}}{e^{-2\lambda} - e^{2\lambda}} \right] e^{\lambda\zeta} + \Delta\Xi(\eta) \left[\frac{1 - e^{2\lambda}}{e^{-2\lambda} - e^{2\lambda}} \right] e^{-\lambda\zeta} - \Delta\Xi(\eta) \\ &= \Delta\Xi(\eta) \left\{ e^{\lambda\zeta} - \left(\frac{1 - e^{2\lambda}}{e^{-2\lambda} - e^{2\lambda}} \right) e^{\lambda\zeta} + \left(\frac{1 - e^{2\lambda}}{e^{-2\lambda} - e^{2\lambda}} \right) e^{-\lambda\zeta} - 1 \right\} \\ &= \Delta\Xi(\eta) \left\{ \frac{e^{\lambda(\zeta-2)} - e^{-\lambda(\zeta-2)} + e^{-\lambda\zeta} - e^{\lambda\zeta}}{e^{-2\lambda} - e^{2\lambda}} - 1 \right\} = \Delta\Xi(\eta) \left\{ \frac{e^{\lambda(\zeta-2)} - e^{-\lambda(\zeta-2)}}{2 \frac{e^{-2\lambda} - e^{2\lambda}}{2}} + \frac{e^{\lambda\zeta} - e^{-\lambda\zeta}}{2 \frac{e^{2\lambda} - e^{-2\lambda}}{2}} - 1 \right\} \end{aligned}$$

Use the equation of the sin hyperbolic function: $\sinh x = \frac{e^x - e^{-x}}{2}$

$$\Phi(\zeta) = \Delta\Xi(\eta) \left\{ -\frac{\sinh[\lambda(\zeta - 2)]}{\sinh[2\lambda]} + \frac{\sinh[\lambda\zeta]}{\sinh[2\lambda]} - 1 \right\}$$

Since $\sinh(-x) = -\sinh x$

$$\Phi(\zeta) = \Delta\Xi(\eta) \left\{ \frac{\sinh[\lambda(2-\zeta)]}{\sinh[2\lambda]} + \frac{\sinh[\lambda\zeta]}{\sinh[2\lambda]} - 1 \right\}$$

$$\Phi(\zeta) = \Delta\Xi(\eta) \left\{ \frac{\sinh[\lambda(2-\zeta)] + \sinh[\lambda\zeta]}{\sinh[2\lambda]} - 1 \right\} \quad (6)$$

where,

$$\lambda = \sqrt{\frac{(\eta^2 - 1) \text{Re}_r}{2\eta^2 \ln(\eta)}}, \quad \Delta\Pi(\eta) = \left(\frac{2\eta^2}{\eta^2 - 1} \right) \Delta p(\eta)$$

$$\Delta\Xi(\eta) = \Delta\Pi(\eta) - \frac{2s^2\eta^2}{\eta^2 - 1} \int_1^\eta \frac{v^2_{\max}(\eta)}{\eta} d\eta$$

From global continuity, we have:

$$\int_0^{2h} V_r (2\pi r) dz = \underbrace{-}_{\text{Inflow}} V_{rin} (2\pi r R_{in}) (2h) \Rightarrow \int_0^2 \frac{V_r}{V_{rin}} \frac{r}{R_{in}} d\left(\frac{z}{h}\right) = -2 \Rightarrow \int_0^2 u \eta d\zeta = -2$$

$$\int_0^2 \Phi(\zeta) d\zeta = -2 \Rightarrow \int_0^2 \Delta\Xi(\eta) \left\{ \frac{\sinh[\lambda(2-\zeta)] + \sinh[\lambda\zeta]}{\sinh[2\lambda]} - 1 \right\} d\zeta = -2 \Rightarrow$$

$$\Delta\Xi(\eta) = \frac{-2}{\int_0^2 \left\{ \frac{\sinh[\lambda(2-\zeta)] + \sinh[\lambda\zeta]}{\sinh[2\lambda]} - 1 \right\} d\zeta} \quad (7)$$

To solve for equation (7), we must first solve the integrals:

$$\int_0^2 \sinh[\lambda(\zeta - 2)] d\zeta \quad \text{and} \quad \int_0^2 \sinh[\lambda\zeta] d\zeta$$

$$a) \int_0^2 \sinh[\lambda\zeta] d\zeta = \frac{1}{\lambda} [\cosh(\lambda\zeta)]_0^2 = \frac{1}{\lambda} [\cosh(2\lambda) - 1]$$

$$b) \int_0^2 \sinh[\lambda(\zeta - 2)] d\zeta$$

$$\text{Let } \psi = \lambda(2 - \zeta) \Rightarrow d\psi = -\lambda d\zeta \Rightarrow d\zeta = -\frac{d\psi}{\lambda}$$

$$\begin{aligned} \int_0^2 \sinh(\psi) \frac{d\psi}{\lambda} &= -\frac{1}{\lambda} \int_0^2 \sinh(\psi) d\psi = -\frac{1}{\lambda} [\cosh(\psi)]_0^2 = -\frac{1}{\lambda} [\cosh[\lambda(2 - \zeta)]] \\ &= -\frac{1}{\lambda} [1 - \cosh(2\lambda)] \end{aligned}$$

If we substitute the above integrals into equation (7), we have:

$$\begin{aligned}
\Delta\Xi(\eta) &= \frac{-2}{\int_0^2 \frac{\sinh[\lambda(2-\zeta)]}{\sinh(2\lambda)} d\zeta + \int_0^2 \frac{\sinh(\lambda\zeta)}{\sinh(2\lambda)} d\zeta - \int_0^2 d\zeta} \\
&= \frac{-2}{\frac{1}{\sinh(2\lambda) \left\{ -\frac{1}{\lambda} + \frac{\cosh(2\lambda)}{\lambda} + \frac{\cosh(2\lambda)}{\lambda} - \frac{1}{\lambda} \right\} - 2}} \\
&= \frac{-2}{\frac{2}{\sinh(2\lambda) \left[\frac{\cosh(2\lambda)-1}{\lambda} \right]} - 2} = \frac{-1}{\left[\frac{\cosh(2\lambda)-1-\lambda \sinh(2\lambda)}{\lambda \sinh(2\lambda)} \right]} \\
\Delta\Xi(\eta) &= \frac{\lambda \sinh(2\lambda)}{\lambda \sinh(2\lambda) - \cosh(2\lambda) + 1}
\end{aligned}$$

From eq. (6), $\Phi(\zeta)$ becomes :

$$\begin{aligned}
\Phi(\zeta) &= \frac{\lambda \sinh(2\lambda)}{\lambda \sinh(2\lambda) - \cosh(2\lambda) + 1} \left\{ \frac{\sinh[\lambda(2-\zeta)] + \sinh(\lambda\zeta)}{\sinh(2\lambda)} - 1 \right\} \\
\text{and } u &= \frac{\Phi(\zeta)}{\eta}
\end{aligned}$$

The radial velocity u was found to be equal to :

$$u = \frac{1}{\eta} \frac{\lambda \sinh(2\lambda)}{\lambda \sinh(2\lambda) - \cosh(2\lambda) + 1} \left\{ \frac{\sinh[\lambda(2-\zeta)] + \sinh(\lambda\zeta)}{\sinh(2\lambda)} - 1 \right\} \quad (8)$$

To solve for the tangential velocity, the θ – momentum must be considered (eq.3).

$$\frac{u \partial(v\eta)}{\partial\eta} = \frac{1}{\text{Re}_r} \frac{\partial^2(v\eta)}{\partial\zeta^2} \quad (3)$$

Since $v\eta = \varphi(\eta)\psi(\zeta)$ and $u \cong -\frac{1}{\eta}$, then the θ - momentum becomes :

$$\left(-\frac{1}{\eta}\right)\frac{\partial}{\partial\eta}[\varphi(\eta)\psi(\zeta)] = \frac{1}{\text{Re}_r}\frac{d^2[\varphi(\eta)\psi(\zeta)]}{d\zeta^2} \Rightarrow \frac{1}{\eta}\psi(\zeta)\frac{\partial\varphi(\eta)}{\partial\eta} = -\frac{1}{\text{Re}_r}\varphi(\eta)\frac{d^2\psi(\zeta)}{d\zeta^2} \Rightarrow$$

$$\frac{1}{\eta}\frac{1}{\varphi(\eta)}\frac{d\varphi(\eta)}{d\eta} = -\frac{1}{\text{Re}_r}\frac{1}{\psi(\zeta)}\frac{d^2\psi(\zeta)}{d\zeta^2} = \beta^2 \quad (\beta = \text{constant}) \quad (9)$$

$$1.) \quad \frac{1}{\eta}\frac{1}{\varphi(\eta)}\frac{d\varphi(\eta)}{d\eta} = \beta^2 \Rightarrow \int \frac{d\varphi(\eta)}{\varphi(\eta)} = \int \beta^2 \eta d\eta \Rightarrow \ln[\varphi(\eta)] = e^{\frac{\beta^2 \eta^2}{2}} + c$$

(c is a constant from integration)

$$\varphi(\eta) = e^{\frac{\beta^2 \eta^2}{2} + c} = k e^{\frac{\beta^2 \eta^2}{2}} \Rightarrow \varphi(\eta) = k e^{\frac{\beta^2 \eta^2}{2}}, \text{ k is a constant} \quad (10)$$

$$2.) \quad -\frac{1}{\text{Re}_r}\frac{1}{\psi(\zeta)}\frac{d^2\psi(\zeta)}{d\zeta^2} = \beta^2 \Rightarrow \frac{d^2\psi(\zeta)}{d\zeta^2} + \beta^2 \text{Re}_r \psi(\zeta) = 0$$

The characteristic equation of the 2nd O.D.E is : $p^2 + \beta^2 \text{Re}_r = 0 \Rightarrow p_{1,2} = \pm i\beta\sqrt{\text{Re}_r}$

Therefore, the differential equation has complex solutions :

$$\psi(\zeta) = A \cos(\beta\sqrt{\text{Re}_r}\zeta) + B \sin(\beta\sqrt{\text{Re}_r}\zeta) \quad (11)$$

where A , B are constants

Since $v\eta = \varphi(\eta)\psi(\zeta)$, then :

$$\stackrel{(9),(10)}{\Rightarrow} v\eta = k e^{\frac{\beta^2 \eta^2}{2}} [A \cos(\beta\sqrt{\text{Re}_r}\zeta) + B \sin(\beta\sqrt{\text{Re}_r}\zeta)] = e^{\frac{\beta^2 \eta^2}{2}} [A' \cos(\beta\sqrt{\text{Re}_r}\zeta) + B' \sin(\beta\sqrt{\text{Re}_r}\zeta)]$$

where $A' = kA$ and $B' = kB$

$$v\eta = \left\{ A' \cos(\beta\sqrt{\text{Re}_r}\zeta) + B' \sin(\beta\sqrt{\text{Re}_r}\zeta) \right\} e^{\frac{\beta^2 \eta^2}{2}} \quad (12)$$

Boundary Conditions:

$$1) z = 0 \text{ or } \zeta = 0 \Rightarrow v = 0$$

$$2) z = h \text{ or } \zeta = 1 \Rightarrow \frac{dv}{d\zeta} = 0 \text{ (maximum velocity at the centerline)}$$

$$(1) \text{ at } \zeta = 0 \quad v = 0 \xRightarrow{(12)} v\eta = 0 \Rightarrow A' = 0$$

$$(2) \text{ at } \zeta = 1 \quad \frac{dv}{d\zeta} = 0 \xRightarrow{(12)} \frac{d}{d\zeta} [B' \sin(\beta \sqrt{\text{Re}_r} \zeta)]_{\zeta=1} = 0 \quad [\text{Since } A' = 0 \text{ and } e^{\frac{\beta^2 \eta^2}{2}} \text{ are constants}]$$

$$\Rightarrow B' \beta \sqrt{\text{Re}_r} \cos(\beta \sqrt{\text{Re}_r}) = 0$$

Since $\beta \sqrt{\text{Re}_r}$ is a constant and B' must be different to zero in order for equation (11) to be valid,

it must be: $\cos(\beta \sqrt{\text{Re}_r}) = 0$. Since cosine becomes zero at $\frac{2n+1}{2} \pi$, then:

$$\cos(\beta \sqrt{\text{Re}_r}) = \cos\left(\frac{2n+1}{2} \pi\right) = 0 \Rightarrow \beta \sqrt{\text{Re}_r} = \frac{2n+1}{2} \pi \Rightarrow \beta = \frac{2n+1}{2\sqrt{\text{Re}_r}} \pi \Rightarrow \beta_n = \frac{2n+1}{2\sqrt{\text{Re}_r}} \pi \quad (13)$$

[$\beta = \beta_n$ (β varies with n)]

$v\eta$ from eq. (12) becomes as follows:

$$v\eta = \sum_{n=0}^{\infty} B_n e^{\frac{\beta_n^2 \eta^2}{2}} \sin\left(\frac{2n+1}{2} \pi \zeta\right) = \phi \psi \Rightarrow$$

Let $B' = B_n$, since B' will vary with n .

$$v = \frac{\phi \psi}{\eta} = \sum_{n=0}^{\infty} B_n \frac{e^{\frac{\beta_n^2 \eta^2}{2}}}{\eta} \sin\left(\frac{2n+1}{2} \pi \zeta\right) \quad (14)$$

From the initial condition ($\eta = 1 \Rightarrow v = 1.0$) equation (14) becomes:

$$1 = \sum_{n=0}^{\infty} B_n e^{\frac{\beta_n^2}{2}} \sin\left(\frac{2n+1}{2}\pi\zeta\right) \Rightarrow \text{If } E_n = B_n e^{\frac{\beta_n^2}{2}}, \text{ then :}$$

$$\Rightarrow 1 = \sum_{n=0}^{\infty} E_n \sin\left(\frac{2n+1}{2}\pi\right)$$

If E_n is written as the sine Fourier series of v , then :

$$E_n = \frac{2}{L} \int_0^L v(\zeta) \sin\left(\frac{n\pi}{L}\zeta\right) d\zeta = \frac{2}{2} \int_0^1 1 \cdot \sin\left(\frac{(2n+1)}{2}\pi\zeta\right) d\zeta$$

if $\alpha = \frac{(2n+1)}{2}\pi$, then

$$\begin{aligned} E_n &= \int_0^2 \sin(\alpha\zeta) d\zeta = -\frac{1}{\alpha} [\cos(\alpha\zeta)]_0^2 = -\frac{1}{\frac{(2n+1)}{2}\pi} \left[\cos\left(\frac{(2n+1)}{2}\pi\right) \right]_0^2 \\ &= -\frac{2}{(2n+1)\pi} \left\{ \underbrace{\cos[(2n+1)\pi]}_{\forall n \cos[(2n+1)\pi]=1} - 1 \right\} = -\frac{2}{(2n+1)\pi} (-1-1) = \frac{4}{(2n+1)\pi} \end{aligned}$$

$$E_n = B_n e^{\frac{\beta_n^2}{2}} = \frac{4}{(2n+1)\pi} \Rightarrow B_n = E_n e^{-\frac{\beta_n^2}{2}} = \frac{4}{(2n+1)\pi} e^{-\frac{\beta_n^2}{2}} \Rightarrow B_n = \frac{4}{(2n+1)\pi} e^{-\frac{\left(\frac{2n+1}{2\sqrt{\text{Re}_r}}\pi\right)^2}{2}} \Rightarrow$$

$$B_n = \frac{4}{(2n+1)\pi} e^{-\left\{\frac{(2n+1)^2 \pi^2}{8 \text{Re}_r}\right\}} \Rightarrow B_n = \frac{4}{(2n+1)\pi} e^{-\left\{\frac{(2n+1)^2 \pi^2}{8 \text{Re}_r}\right\}} \quad (15)$$

where $\beta_n = \frac{2n+1}{2\sqrt{\text{Re}_r}}\pi$ (eq.12),

Substitute the constant B_n back to equation (14) and the tangential velocity v becomes :

$$v = \sum_{n=0}^{\infty} \frac{4}{(2n+1)\pi} e^{-\frac{\beta^2 n}{2}} e^{-\frac{\beta n^2 \eta^2}{2}} \frac{1}{\eta} \sin\left(\frac{2n+1}{2} \pi \zeta\right) = \sum_{n=0}^{\infty} \frac{4}{(2n+1)\pi} e^{-\left\{\frac{(2n+1)^2 \pi^2}{8 \text{Re}_r} (\eta^2 - 1)\right\}} \frac{1}{\eta} \sin\left(\frac{2n+1}{2} \pi \zeta\right)$$

$$v = \sum_{n=0}^{\infty} \frac{4}{(2n+1)\pi} e^{-\left\{\frac{(2n+1)^2 \pi^2}{8 \text{Re}_r} (\eta^2 - 1)\right\}} \frac{1}{\eta} \sin\left(\frac{2n+1}{2} \pi \zeta\right) \quad (16)$$

Since maximum v occurs at the centerline where $\zeta = 1$, eq. (16) becomes :

$$v_{\max} = \sum_{n=0}^{\infty} \frac{4(-1)^n}{(2n+1)\pi} \frac{1}{\eta} e^{-\left\{\frac{(2n+1)^2 \pi^2}{8 \text{Re}_r} (\eta^2 - 1)\right\}} \quad (17)$$

$$\text{At } \zeta = 1 : n = 0 \rightarrow \sin\left(\frac{2 \cdot 0 + 1}{2} \pi\right) = 1$$

$$n = 1 \rightarrow \sin\left(\frac{2 \cdot 1 + 1}{2} \pi\right) = -1$$

$$\text{Therefore, for every } n : \sin\left(\frac{2n+1}{2} \pi\right) = (-1)^n$$

Since v_{\max} was defined $\Delta\Xi(\eta)$ can be calculated.

When the global continuity was considered previously, $\Delta\Xi(\eta)$ was found to be equal to :

$$\Delta\Xi(\eta) = \frac{\lambda \sinh(2\lambda)}{\lambda \sinh(2\lambda) - \cosh(2\lambda) + 1} = \Delta\Pi(\eta) - \frac{2s^2 \eta^2}{(\eta^2 - 1)} \int_1^\eta \frac{v_{\max}^2(\eta)}{\eta} d\eta \Rightarrow$$

$$\Delta\Pi(\eta) = \frac{\lambda \sinh(2\lambda)}{\lambda \sinh(2\lambda) - \cosh(2\lambda) + 1} + \frac{2s^2 \eta^2}{(\eta^2 - 1)} \int_1^\eta \frac{v_{\max}^2(\eta)}{\eta} d\eta \quad (18)$$

$$\text{and } v_{\max} = \sum_{n=0}^{\infty} \frac{4(-1)^n}{(2n+1)\pi} \frac{1}{\eta} e^{-\left\{\frac{(2n+1)^2 \pi^2}{8 \text{Re}_r} (\eta^2 - 1)\right\}} = \sum_{n=0}^{\infty} \frac{4(-1)^n}{(2n+1)\pi} \frac{1}{\eta} e^{-\left\{\frac{\beta^2 n}{2} (\eta^2 - 1)\right\}} = \sum_{n=0}^{\infty} \frac{4(-1)^n}{(2n+1)\pi} \frac{1}{\eta} e^{-\left\{-\frac{\beta^2 n}{2} (1 - \eta^2)\right\}}$$

The integral $\int_1^\eta \frac{v_{\max}^2(\eta)}{\eta} d\eta$ will be solved first.

$$\text{Using the property } \left(\sum_{i=0}^n x_i\right)^2 = \sum_{j=0}^n \sum_{k=0}^m x_j x_k$$

$$v^2_{\max} = \sum_{n=0}^{\infty} \sum_{m=0}^{\infty} \frac{16(-1)^n (-1)^m}{(2n+1)(2m+1)\pi^2} \frac{1}{\eta^2} \exp\left\{-\frac{\beta^2_n}{2}(1-\eta^2) - \frac{\beta^2_m}{2}(1-\eta^2)\right\} \Rightarrow$$

$$v^2_{\max} = \sum_{n=0}^{\infty} \sum_{m=0}^{\infty} \frac{16(-1)^{n+m}}{(2n+1)(2m+1)\pi^2} \frac{1}{\eta^2} \exp\left\{-\frac{(\beta^2_n + \beta^2_m)}{2}(1-\eta^2)\right\}$$

Therefore,

$$\int_1^{\eta} \frac{v^2_{\max}(\eta)}{\eta} d\eta = \sum_{n=0}^{\infty} \sum_{m=0}^{\infty} \frac{16(-1)^{n+m}}{(2n+1)(2m+1)\pi^2} \underbrace{\int_1^{\eta} \frac{1}{\eta^3} \exp\left\{-\frac{(\beta^2_n + \beta^2_m)}{2}(1-\eta^2)\right\} d\eta}_{(19)}$$

$$\text{Let } \alpha = \frac{(\beta^2_n + \beta^2_m)}{2}$$

$$\text{Then the integral becomes: } \int_1^{\eta} \frac{1}{\eta^3} e^{-\alpha(1-\eta^2)} d\eta = e^{-\alpha} \int_1^{\eta} \frac{1}{\eta^3} e^{\alpha\eta^2} d\eta$$

$$\text{Change the variables from } \eta^2 \text{ to } \delta. \text{ If } \eta^2 = \delta \Rightarrow d\delta = 2\eta d\eta \Rightarrow d\eta = \frac{d\delta}{2\eta}$$

$$\text{Then the integral becomes: } \int_1^{\eta} \frac{1}{\eta^3} e^{-\alpha(1-\eta^2)} d\eta = e^{-\alpha} \int_1^{\eta} \frac{1}{\eta^3} e^{\alpha\eta^2} d\eta = \frac{e^{-\alpha}}{2} \int_1^{\eta} \frac{e^{\alpha\delta}}{\eta^3} \frac{d\delta}{\eta} = \frac{e^{-\alpha}}{2} \int_1^{\eta} \frac{e^{\alpha\delta}}{\delta^2} d\delta$$

$$\text{Use the following properties to solve the integral } \frac{e^{-\alpha}}{2} \int_1^{\eta} \frac{e^{\alpha\delta}}{\delta^2} d\delta$$

$$a). \quad \int \frac{e^{ax}}{x} = \ln(x) + \frac{ax}{1 \cdot 1!} + \frac{(ax)^2}{2 \cdot 2!} + \frac{(ax)^3}{3 \cdot 3!} + \dots$$

$$b). \quad \int \frac{e^{ax}}{x^n} = \frac{1}{n-1} \left(-\frac{e^{ax}}{x^{n-1}} + a \int \frac{e^{ax}}{x^{n-1}} dx \right), \quad n \neq 1$$

$$\begin{aligned}
& \frac{e^{-\alpha}}{2} \int_1^\eta \frac{e^{\alpha\delta}}{\delta^2} d\delta = \frac{e^{-\alpha}}{2} \left\{ \frac{1}{2-1} \left[\left[\frac{-e^{\alpha\delta}}{\delta^{2-1}} \right]_1^\eta + \alpha \int_1^\eta \frac{e^{\alpha\delta}}{\delta^{2-1}} d\delta \right] \right\} = \frac{e^{-\alpha}}{2} \left\{ \left[-\frac{e^{\alpha\eta^3}}{\eta^2} \right]_1^\eta + \alpha \int_1^\eta \frac{e^{\alpha\delta}}{\delta} d\delta \right\} = \\
& \stackrel{a)}{=} \frac{e^{-\alpha}}{2} \left\{ \left[-\frac{e^{\alpha\eta^3}}{\eta^2} \right]_1^\eta + \alpha \left[\ln(\delta) + \frac{a\delta}{1 \cdot 1!} + \frac{(a\delta)^2}{2 \cdot 2!} + \frac{(a\delta)^3}{3 \cdot 3!} + \dots \right]_1^\eta \right\} = \\
& = \frac{e^{-\alpha}}{2} \left\{ -\frac{e^{\alpha\eta^3}}{\eta^2} + e^\alpha + \alpha \left[\left(\ln(\eta^2) + \alpha\eta^2 + \frac{1}{2} \frac{(\alpha\eta^2)^2}{2!} + \frac{1}{3} \frac{(\alpha\eta^2)^3}{3!} + \dots + \frac{1}{n} \frac{(\alpha\eta^2)^n}{n!} + \dots \right) - \right. \right. \\
& \quad \left. \left. - \left(0 + \alpha + \frac{1}{2} \frac{\alpha^2}{2!} + \frac{1}{3} \frac{\alpha^3}{3!} + \dots + \frac{1}{n} \frac{\alpha^n}{n!} + \dots \right) \right] \right\} = \\
& = \frac{e^{-\alpha}}{2} \left\{ -\frac{e^{\alpha\eta^3}}{\eta^2} + e^\alpha + \alpha \ln(\eta^2) + \alpha \left[\left(\frac{\alpha\eta^2}{1} + \frac{1}{2} \frac{\alpha^2 (\eta^2)^2}{2!} + \frac{1}{3} \frac{\alpha^3 (\eta^2)^3}{3!} + \dots + \frac{1}{n} \frac{\alpha^n (\eta^2)^n}{n!} + \dots \right) - \right. \right. \\
& \quad \left. \left. - \left(\frac{\alpha}{1} + \frac{1}{2} \frac{\alpha^2}{2!} + \frac{1}{3} \frac{\alpha^3}{3!} + \dots + \frac{1}{n} \frac{\alpha^n}{n!} + \dots \right) \right] \right\} = \\
& = \frac{e^{-\alpha}}{2} \left\{ -\frac{e^{\alpha\eta^3}}{\eta^2} + e^\alpha + \alpha \ln(\eta^2) + \alpha \left[\sum_{k=1}^{\infty} \frac{\alpha^k}{k \cdot k!} (\eta^{2k} - 1) \right] \right\} = \\
& = -\frac{e^{-\alpha(1-\eta^2)}}{2\eta^2} + \frac{e^{-\alpha}e^\alpha}{2} + \frac{\alpha e^{-\alpha}}{2} \left[\ln(\eta^2) + \sum_{k=1}^{\infty} \frac{\alpha^k}{k \cdot k!} (\eta^{2k} - 1) \right] = \\
& = \frac{1}{2} \left\{ 1 - \frac{e^{-\alpha(1-\eta^2)}}{\eta^2} + \alpha e^{-\alpha} \left[\ln(\eta^2) + \sum_{k=1}^{\infty} \frac{\alpha^k}{k \cdot k!} (\eta^{2k} - 1) \right] \right\}
\end{aligned}$$

Substitute the above expression into the integral $\int_1^\eta \frac{v_{\max}^2(\eta)}{\eta} d\eta$:

$$\begin{aligned}
 \text{eq.(19)} \Rightarrow \int_1^\eta \frac{v_{\max}^2(\eta)}{\eta} d\eta &= \sum_{n=0}^{\infty} \sum_{m=0}^{\infty} \frac{16(-1)^{n+m}}{(2n+1)(2m+1)\pi^2} \int_1^\eta \frac{1}{\eta^3} \exp\left\{-\frac{(\beta_n^2 + \beta_m^2)}{2}(1-\eta^2)\right\} d\eta = \\
 &= \sum_{n=0}^{\infty} \sum_{m=0}^{\infty} \frac{16(-1)^{n+m}}{(2n+1)(2m+1)\pi^2} e^{-\alpha} \int_1^\eta \frac{1}{\eta^3} e^{\alpha\eta^2} d\eta = \\
 &= \sum_{n=0}^{\infty} \sum_{m=0}^{\infty} \frac{16(-1)^{n+m}}{(2n+1)(2m+1)\pi^2} \frac{e^{-\alpha}}{2} \int_1^\eta \frac{e^{\alpha\delta}}{\delta^2} d\delta = \\
 &= \sum_{n=0}^{\infty} \sum_{m=0}^{\infty} \frac{16(-1)^{n+m}}{(2n+1)(2m+1)\pi^2} \frac{1}{2} \left\{ 1 - \frac{e^{-\alpha(1-\eta^2)}}{\eta^2} + \alpha e^{-\alpha} \left[\ln(\eta^2) + \sum_{k=1}^{\infty} \frac{\alpha^k}{k \cdot k!} (\eta^{2k} - 1) \right] \right\}
 \end{aligned}$$

Therefore, the pressure $\Delta\Pi(\eta)$ is found by substituting the above expression into eq.(18):

$$\begin{aligned}
 \Delta\Pi(\eta) &= \frac{\lambda \sinh(2\lambda)}{\lambda \sinh(2\lambda) - \cosh(2\lambda) + 1} + \frac{2s^2\eta^2}{(\eta^2 - 1)} \int_1^\eta \frac{v_{\max}^2(\eta)}{\eta} d\eta = \\
 &= \frac{\lambda \sinh(2\lambda)}{\lambda \sinh(2\lambda) - \cosh(2\lambda) + 1} + \frac{2s^2\eta^2}{(\eta^2 - 1)} \sum_{n=0}^{\infty} \sum_{m=0}^{\infty} \frac{16(-1)^{n+m}}{(2n+1)(2m+1)\pi^2} \frac{1}{2} \left\{ 1 - \frac{e^{-\alpha(1-\eta^2)}}{\eta^2} + \right. \\
 &\quad \left. + \alpha e^{-\alpha} \left[\ln(\eta^2) + \sum_{k=1}^{\infty} \frac{\alpha^k}{k \cdot k!} (\eta^{2k} - 1) \right] \right\} \Rightarrow \\
 \Delta\Pi(\eta) &= \frac{\lambda \sinh(2\lambda)}{\lambda \sinh(2\lambda) - \cosh(2\lambda) + 1} + \frac{16s^2\eta^2}{(\eta^2 - 1)\pi^2} \sum_{n=0}^{\infty} \sum_{m=0}^{\infty} \frac{(-1)^{n+m}}{(2n+1)(2m+1)} \left\{ 1 - \frac{e^{-\alpha(1-\eta^2)}}{\eta^2} + \right. \\
 &\quad \left. + \alpha e^{-\alpha} \left[\ln(\eta^2) + \sum_{k=1}^{\infty} \frac{\alpha^k}{k \cdot k!} (\eta^{2k} - 1) \right] \right\}
 \end{aligned}$$

$$\text{where, } \alpha = \frac{(\beta_n^2 + \beta_m^2)}{2} = \frac{1}{2} \left[\frac{(2n+1)\pi}{2\sqrt{\text{Re}_r}} \right]^2 + \frac{1}{2} \left[\frac{(2m+1)\pi}{2\sqrt{\text{Re}_r}} \right]^2 \Rightarrow \alpha = \frac{\pi^2}{8\text{Re}_r} \left[(2n+1)^2 + (2m+1)^2 \right]$$

$$\beta_n = \frac{2n+1}{2\sqrt{\text{Re}_r}} \pi, \quad \lambda = \sqrt{\frac{(\eta^2 - 1)\text{Re}_r}{2\eta^2 \ln(\eta)}}$$

Case 2: Outflow and Swirl

r-momentum:

$$\stackrel{(2)}{\Rightarrow} u \frac{\partial u}{\partial \eta} - s^2 \frac{v^2}{\eta} = -\frac{d(\Delta p)}{d\eta} + \frac{1}{\text{Re}_r} \left\{ \frac{1}{\eta} \frac{\partial^2 (u\eta)}{\partial \zeta^2} \right\} \Rightarrow$$

$$\left(\frac{1}{\eta} \right) \frac{\partial}{\partial \eta} \left(\frac{\Phi(\zeta)}{\eta} \right) - s^2 \frac{v^2}{\eta} = -\frac{d(\Delta p)}{d\eta} + \frac{1}{\eta \text{Re}_r} \left\{ \frac{\partial^2 (\Phi(\zeta))}{\partial \zeta^2} \right\} \Rightarrow$$

$$\left(\frac{1}{\eta} \right) \left(-\frac{1}{\eta^2} \right) \Phi(\zeta) - s^2 \frac{v^2}{\eta} = -\frac{d(\Delta p)}{d\eta} + \frac{1}{\eta \text{Re}_r} \frac{d^2 \Phi(\zeta)}{d\zeta^2} \Rightarrow$$

By substituting v^2 with v_{\max}^2 , we get:

$$\left(\frac{1}{\eta} \right) \left(-\frac{1}{\eta^2} \right) \Phi(\zeta) - s^2 \frac{v_{\max}^2(\eta)}{\eta} = -\frac{d(\Delta p)}{d\eta} + \frac{1}{\eta \text{Re}_r} \frac{d^2 \Phi(\zeta)}{d\zeta^2} \Rightarrow$$

$$\left(-\int_1^\eta \frac{1}{\eta^3} d\eta \right) \Phi(\zeta) - s^2 \int_1^\eta \frac{v_{\max}^2(\eta)}{\eta} d\eta = -\int_1^\eta \frac{d(\Delta p)}{d\eta} d\eta + \frac{1}{\text{Re}_r} \frac{d^2 \Phi(\zeta)}{d\zeta^2} \int_1^\eta \frac{1}{\eta} d\eta \Rightarrow$$

$$-\left[-\frac{1}{2\eta^2} \right]_1^\eta \Phi(\zeta) - s^2 \int_1^\eta \frac{v_{\max}^2(\eta)}{\eta} d\eta = -[\Delta p]_1^\eta + \frac{1}{\text{Re}_r} \frac{d^2 \Phi(\zeta)}{d\zeta^2} [\ln(\eta)]_1^\eta \Rightarrow$$

$$-\left(\frac{\eta^2 - 1}{2\eta^2} \right) \Phi(\zeta) - s^2 \int_1^\eta \frac{v_{\max}^2(\eta)}{\eta} d\eta = -\Delta p(\eta) + \frac{1}{\text{Re}_r} \frac{d^2 \Phi(\zeta)}{d\zeta^2} \ln(\eta) \Rightarrow$$

$$\frac{d^2 \Phi(\zeta)}{d\zeta^2} + \underbrace{\frac{\text{Re}_r}{\ln(\eta)} \frac{(\eta^2 - 1)}{2\eta^2}}_{=\lambda^2} \Phi(\zeta) = \frac{\text{Re}_r}{\ln(\eta)} \Delta p(\eta) - s^2 \frac{\text{Re}_r}{\ln(\eta)} \int_1^\eta \frac{v_{\max}^2(\eta)}{\eta} d\eta \Rightarrow$$

$$\begin{aligned}
\frac{d^2\Phi(\zeta)}{d\zeta^2} + \lambda^2\Phi(\zeta) &= \lambda^2 \left\{ \underbrace{\left(\frac{2\eta^2}{(\eta^2-1)} \right) \Delta p(\eta)}_{=\Delta\Pi(\eta)} - \frac{2s^2\eta^2}{(\eta^2-1)} \int_1^\eta \frac{v_{\max}^2(\eta)}{\eta} d\eta \right\} \Rightarrow \\
\frac{d^2\Phi(\zeta)}{d\zeta^2} + \lambda^2\Phi(\zeta) &= \lambda^2 \left\{ \underbrace{\Delta\Pi(\eta) - \frac{2s^2\eta^2}{(\eta^2-1)} \int_1^\eta \frac{v_{\max}^2(\eta)}{\eta} d\eta}_{=\Delta\Xi(\eta)} \right\} \\
\frac{d^2\Phi(\zeta)}{d\zeta^2} + \lambda^2\Phi(\zeta) &= \lambda^2 \Delta\Xi(\eta) \quad - 2^{nd} \text{ non-homogeneous O.D.E} \quad (20)
\end{aligned}$$

where λ^2 , $\Delta\Pi(\eta)$ and $\Delta\Xi(\eta)$ were defined in the previous case (inflow and swirl)

Following the same procedure, the 2nd O.D.E has a homogeneous and a particular solution. Following the same procedure as in section 2.2.1, the particular solution was found to be equal to: $\Phi(\zeta)_p = \Delta\Xi(\eta)$

The homogeneous differential equation $\frac{\partial^2\Phi(\zeta)}{\partial\zeta^2} + \lambda^2\Phi(\zeta) = 0$ has to be solved.

Its characteristic equation gives : $p^2 + \lambda^2 = 0 \Rightarrow p_{1,2} = \pm i\lambda$, therefore equation (20) has as solutions the following :

$$\begin{aligned}
\Phi(\zeta) &= A \cos(\lambda\zeta) + B \sin(\lambda\zeta) + \Delta\Xi(\eta) = u\eta \\
\text{or} \quad A \cos(\lambda\zeta) + B \sin(\lambda\zeta) + \Delta\Xi(\eta) &= u\eta \quad (21)
\end{aligned}$$

By applying the boundary conditions ($\zeta = 0 \Rightarrow u = 0$ and $\zeta = 2 \Rightarrow u = 0$) from

eq.(21) we have:

$$(i) \zeta = 0 \quad u = 0$$

$$\stackrel{(21)}{\Rightarrow} A \cos(0) + B \sin(0) + \Delta \Xi(\eta) = 0 \Rightarrow A + \Delta \Xi(\eta) = 0 \Rightarrow$$

$$A = -\Delta \Xi(\eta) \quad (22)$$

$$(ii) \zeta = 2 \quad u = 0$$

$$\stackrel{(21)}{\Rightarrow} A \cos(2\lambda) + B \sin(2\lambda) + \Delta \Xi(\eta) = 0 \stackrel{(22)}{\Rightarrow} -\Delta \Xi(\eta) \cos(2\lambda) + B \sin(2\lambda) + \Delta \Xi(\eta) = 0 \Rightarrow$$

$$B \sin(2\lambda) - \Delta \Xi(\eta) [\cos(2\lambda) - 1] = 0 \Rightarrow$$

$$B = \Delta \Xi(\eta) \frac{\cos(2\lambda) - 1}{\sin(2\lambda)} \quad (23)$$

Substitute constants A and B from eq.(22) and eq.(23) back to eq.(21) we get :

$$\stackrel{(21)}{\Rightarrow} \Phi(\zeta) = -\Delta \Xi(\eta) \cos(\lambda \zeta) + \Delta \Xi(\eta) \frac{[\cos(2\lambda) - 1]}{\sin(2\lambda)} \sin(\lambda \zeta) + \Delta \Xi(\eta) \Rightarrow$$

$$= -\Delta \Xi(\eta) \left[\cos(\lambda \zeta) - \frac{[\cos(2\lambda) - 1]}{\sin(2\lambda)} \sin(\lambda \zeta) - 1 \right]$$

$$= -\Delta \Xi(\eta) \left[\frac{\overbrace{\cos(\lambda \zeta) \sin(2\lambda) - \cos(2\lambda) \sin(\lambda \zeta)}^{\sin(2\lambda - \lambda \zeta)} + \sin(\lambda \zeta)}{\sin(2\lambda)} - 1 \right]$$

$$= -\Delta \Xi(\eta) \left[\frac{\sin(2\lambda - \lambda \zeta) + \sin(\lambda \zeta)}{\sin(2\lambda)} - 1 \right]$$

and from the trigonometric property : $\sin \alpha + \sin \beta = 2 \sin \left(\frac{\alpha + \beta}{2} \right) \cos \left(\frac{\alpha - \beta}{2} \right)$ we have :

$$= -\Delta \Xi(\eta) \left[\frac{2 \sin \left(\frac{2\lambda - \lambda \zeta + \lambda \zeta}{2} \right) \cos \left(\frac{2\lambda - \lambda \zeta - \lambda \zeta}{2} \right)}{\sin(2\lambda)} - 1 \right]$$

$$= -\Delta \Xi(\eta) \left[\frac{2 \sin(\lambda) \cos(\lambda - \lambda \zeta)}{\sin(2\lambda)} - 1 \right] = \Delta \Xi(\eta) \left[\frac{2 \sin(\lambda) \cos[\lambda(1 - \zeta)]}{\sin(2\lambda)} + 1 \right]$$

Therefore,

$$\Phi(\zeta) = \Delta\Xi(\eta) \left[\frac{2\sin(\lambda)\cos[\lambda(1-\zeta)]}{\sin(2\lambda)} + 1 \right] \quad (24)$$

From global continuity (as for the inflow case), we have :

$$\begin{aligned} \int_0^2 \Phi(\zeta) d\zeta &= +2 \Rightarrow \\ \int_0^2 \Delta\Xi(\eta) \left\{ \frac{2\sin(\lambda)\cos[\lambda(1-\zeta)]}{\sin(2\lambda)} + 1 \right\} d\zeta &= 2 \Rightarrow \\ \Delta\Xi(\eta) &= \frac{2}{\int_0^2 \left\{ \frac{2\sin(\lambda)\cos[\lambda(1-\zeta)]}{\sin(2\lambda)} + 1 \right\} d\zeta} \end{aligned} \quad (25)$$

First solve the integral $\int_0^2 \cos[\lambda(1-\zeta)] d\zeta$.

$$\text{Let } \psi = \lambda(1-\zeta) \Rightarrow d\psi = -\lambda d\zeta \Rightarrow d\zeta = \frac{-d\psi}{\lambda}$$

$$\begin{aligned} \int_0^2 \cos(\psi) \left(\frac{-d\psi}{\lambda} \right) &= -\frac{1}{\lambda} \int_0^2 \cos(\psi) d\psi = -\frac{1}{\lambda} [\sin(\psi)]_0^2 = -\frac{1}{\lambda} [\sin(\lambda(1-\zeta))]_0^2 = -\frac{1}{\lambda} [\sin(-\lambda) - \sin(\lambda)] \\ &= \frac{-2\sin(\lambda)}{\lambda} \end{aligned}$$

Substituting the solved integral into equation (25), we get :

$$\begin{aligned} \Delta\Xi(\eta) &= \frac{2}{\frac{2\sin(\lambda)}{\sin(2\lambda)} \int_0^2 \cos[\lambda(1-\zeta)] d\zeta + \int_0^2 d\zeta} = \frac{2}{\frac{2\sin(\lambda)}{\sin(2\lambda)} \left[\frac{-2\sin(\lambda)}{\lambda} \right] + 2} = \frac{1}{\frac{-2\sin^2(\lambda) + \lambda \sin(2\lambda)}{\lambda \sin(2\lambda)}} \\ \Delta\Xi(\eta) &= \frac{\lambda \sin(2\lambda)}{\lambda \sin(2\lambda) - 2\sin^2(\lambda)} \end{aligned} \quad (26)$$

Substitute equation (26) into equation (24) in order to get $\Phi(\zeta)$:

$$\Phi(\zeta) = \Delta \Xi(\eta) \left[\frac{2\sin(\lambda)\cos[\lambda(1-\zeta)]}{\sin(2\lambda)} + 1 \right] = \frac{\lambda \sin(2\lambda)}{\lambda \sin(2\lambda) - 2\sin^2(\lambda)} \left[\frac{2\sin(\lambda)\cos[\lambda(1-\zeta)]}{\sin(2\lambda)} + 1 \right]$$

or

$$\Phi(\zeta) = \frac{\lambda \sin(2\lambda)}{\lambda \sin(2\lambda) - 2\sin^2(\lambda)} \left[\frac{2\sin(\lambda)\cos[\lambda(1-\zeta)]}{\sin(2\lambda)} + 1 \right]$$

and since $u = \frac{\Phi(\zeta)}{\eta}$

The radial velocity for Outflow and Swirl is given by :

$$u = \frac{1}{\eta} \frac{\lambda \sin(2\lambda)}{\lambda \sin(2\lambda) - 2\sin^2(\lambda)} \left[\frac{2\sin(\lambda)\cos[\lambda(1-\zeta)]}{\sin(2\lambda)} + 1 \right] \quad (27)$$

The tangential velocity is solved as in the inflow and swirl case, when the θ - momentum was considered (eq.3).

$$\frac{u\partial(v\eta)}{\partial\eta} = \frac{1}{\text{Re}_r} \frac{\partial^2(v\eta)}{\partial\zeta^2} \quad (3)$$

If $v\eta = \varphi(\eta)\psi(\zeta)$ and $u \cong \frac{1}{\eta}$

The θ - momentum becomes :

$$\left(\frac{1}{\eta} \right) \frac{\partial}{\partial\eta} [\varphi(\eta)\psi(\zeta)] = -\frac{1}{\text{Re}_r} \frac{\partial^2 [\varphi(\eta)\psi(\zeta)]}{\partial\zeta^2} \Rightarrow$$

$$\frac{1}{\eta} \psi(\zeta) \frac{d\varphi(\eta)}{d\eta} = \frac{1}{\text{Re}_r} \varphi(\eta) \frac{d^2\psi(\zeta)}{d\zeta^2} \Rightarrow$$

$$\frac{1}{\eta} \frac{1}{\varphi(\eta)} \frac{d\varphi(\eta)}{d\eta} = \frac{1}{\text{Re}_r} \frac{1}{\psi(\zeta)} \frac{d^2\psi(\zeta)}{d\zeta^2} = -\beta^2 = \text{constant}$$

Therefore, two differential equations must be considered :

$$(a) \quad \frac{1}{\eta} \frac{1}{\varphi(\eta)} \frac{d\varphi(\eta)}{d\eta} = -\beta^2 \Rightarrow \int \frac{d\varphi(\eta)}{\varphi(\eta)} = \int -\beta^2 \eta d\eta \Rightarrow \ln[\varphi(\eta)] = e^{-\frac{\beta^2 \eta^2}{2}} + c$$

(c is a constant from integration)

$$\varphi(\eta) = e^{-\frac{\beta^2 \eta^2}{2} + c} = k e^{-\frac{\beta^2 \eta^2}{2}}$$

$$\varphi(\eta) = k e^{-\frac{\beta^2 \eta^2}{2}}, \text{ k is a constant} \quad (28)$$

$$(b) \quad \frac{1}{\text{Re}_r} \frac{1}{\psi(\zeta)} \frac{d^2 \psi(\zeta)}{d\zeta^2} = -\beta^2 \Rightarrow \frac{d^2 \psi(\zeta)}{d\zeta^2} + \beta^2 \text{Re}_r \psi(\zeta) = 0$$

The solution to the differential equation is :

$$\psi(\zeta) = A \cos(\beta \sqrt{\text{Re}_r} \zeta) + B \sin(\beta \sqrt{\text{Re}_r} \zeta) \quad (29)$$

where A, B are constants

$$\text{Since } v\eta = \varphi(\eta)\psi(\zeta) \Rightarrow v\eta = k e^{-\frac{\beta^2 \eta^2}{2}} [A \cos(\beta \sqrt{\text{Re}_r} \zeta) + B \sin(\beta \sqrt{\text{Re}_r} \zeta)]$$

and $A' = kA$ and $B' = kB$

$$[A' \cos(\beta \sqrt{\text{Re}_r} \zeta) + B' \sin(\beta \sqrt{\text{Re}_r} \zeta)] e^{-\frac{\beta^2 \eta^2}{2}} = v\eta \quad (30)$$

Apply the Boundary conditions:

$$(i) \quad \zeta = 0 \rightarrow v = 0$$

$$(ii) \quad \zeta = 1 \rightarrow \frac{dv}{d\zeta} = 0$$

Therefore from equation (30) we have:

$$\stackrel{(i)}{\Rightarrow} A' = 0$$

$$\stackrel{(ii)}{\Rightarrow} B' \beta \sqrt{\text{Re}_r} \cos(\beta \sqrt{\text{Re}_r}) = 0 \Rightarrow \text{Since } B' \text{ and } \beta \sqrt{\text{Re}_r} \text{ cannot be zero it has to be :}$$

$$\Rightarrow \cos(\beta \sqrt{\text{Re}_r}) = 0 = \cos\left(\frac{2n+1}{2} \pi\right) = 0$$

Since $\beta = \beta_n$ (β varies with n)

$$\text{So,} \quad \beta_n = \frac{2n+1}{2\sqrt{\text{Re}_r}} \pi$$

By substituting β_n back to equation (30), $v\eta$ becomes :

$$v\eta = \sum_{n=0}^{\infty} B_n e^{\frac{-\beta_n^2 \eta^2}{2}} \sin\left(\frac{2n+1}{2} \pi \zeta\right) = \phi\psi \Rightarrow$$

and B' is replaced with B_n since B' will vary with n .

$$v = \frac{\phi\psi}{\eta} = \sum_{n=0}^{\infty} B_n \frac{e^{\frac{-\beta_n^2 \eta^2}{2}}}{\eta} \sin\left(\frac{2n+1}{2} \pi \zeta\right) \quad (31)$$

By applying the initial condition ($\eta = 1$ $v = 1.0$) to equation (31) and

by letting $E_n = B_n e^{\frac{-\beta_n^2}{2}}$, we get :

$$\Rightarrow 1 = \sum_{n=0}^{\infty} E_n \sin\left(\frac{2n+1}{2} \pi\right)$$

If E_n is expressed as the Fourier sine series of v , it is found to be equal to :

$$E_n = \frac{4}{(2n+1)\pi}$$

Then, $E_n = B_n e^{\frac{-\beta_n^2}{2}} = \frac{4}{(2n+1)\pi} \Rightarrow$ Since from eq.(12) : $\beta_n = \frac{2n+1}{2\sqrt{\text{Re}_r}}\pi$, B_n becomes :

$$B_n = \frac{4}{(2n+1)\pi} e^{\frac{\left(\frac{2n+1}{2\sqrt{\text{Re}_r}}\pi\right)^2}{2}} = \frac{4}{(2n+1)\pi} e^{\left\{\frac{(2n+1)^2 \pi^2}{8\text{Re}_r}\right\}}$$

$$B_n = \frac{4}{(2n+1)\pi} e^{\left\{\frac{(2n+1)^2 \pi^2}{8\text{Re}_r}\right\}} \quad (32)$$

Substitute the constant B_n back to equation (31), therefore the tangential velocity v becomes :

$$v = \sum_{n=0}^{\infty} \frac{4}{(2n+1)\pi} e^{\frac{\beta_n^2}{2}} e^{-\frac{\beta_n^2 \eta^2}{2}} \frac{1}{\eta} \sin\left(\frac{2n+1}{2} \pi \zeta\right) = \sum_{n=0}^{\infty} \frac{4}{(2n+1)\pi} e^{-\left\{\frac{(2n+1)^2 \pi^2}{8 \text{Re}_r} (\eta^2 - 1)\right\}} \frac{1}{\eta} \sin\left(\frac{2n+1}{2} \pi \zeta\right)$$

$$v = \sum_{n=0}^{\infty} \frac{4}{(2n+1)\pi} e^{-\left\{\frac{(2n+1)^2 \pi^2}{8 \text{Re}_r} (\eta^2 - 1)\right\}} \frac{1}{\eta} \sin\left(\frac{2n+1}{2} \pi \zeta\right) \quad (33)$$

The maximum v occurs at the centerline where $\zeta = 1$. Therefore from equation (33) we have :

$$v_{\max} = \sum_{n=0}^{\infty} \frac{4(-1)^n}{(2n+1)\pi} \frac{1}{\eta} e^{-\left\{\frac{(2n+1)^2 \pi^2}{8 \text{Re}_r} (\eta^2 - 1)\right\}} \quad (34)$$

Since v_{\max} is known from equation (34), $\Delta\Xi(\eta)$ can now be calculated.

Therefore,

$$\Delta\Xi(\eta) = \frac{\lambda \sin(2\lambda)}{\lambda \sin(2\lambda) - 2\sin^2(\lambda)} = \Delta\Pi(\eta) - \frac{2s^2 \eta^2}{(\eta^2 - 1)} \int_1^{\eta} \frac{v^2_{\max}(\eta)}{\eta} d\eta \quad (35)$$

and

$$v_{\max} = \sum_{n=0}^{\infty} \frac{4(-1)^n}{(2n+1)\pi} \frac{1}{\eta} e^{-\left\{\frac{(2n+1)^2 \pi^2}{8 \text{Re}_r} (\eta^2 - 1)\right\}} = \sum_{n=0}^{\infty} \frac{4(-1)^n}{(2n+1)\pi} \frac{1}{\eta} e^{-\left\{\frac{\beta_n^2}{2} (\eta^2 - 1)\right\}}$$

$$v^2_{\max} = \sum_{n=0}^{\infty} \sum_{m=0}^{\infty} \frac{16(-1)^{n+m}}{(2n+1)(2m+1)\pi^2} \frac{1}{\eta^2} \exp\left\{-\frac{(\beta_n^2 + \beta_m^2)}{2} (\eta^2 - 1)\right\}$$

Therefore, the integral becomes:

$$\int_1^{\eta} \frac{v^2_{\max}(\eta)}{\eta} d\eta = \sum_{n=0}^{\infty} \sum_{m=0}^{\infty} \frac{16(-1)^{n+m}}{(2n+1)(2m+1)\pi^2} \underbrace{\int_1^{\eta} \frac{1}{\eta^3} \exp\left\{-\frac{(\beta_n^2 + \beta_m^2)}{2} (\eta^2 - 1)\right\} d\eta}_{\text{integral}}$$

and by using the same methodology as in the case of inflow and swirl to solve the above integral, we have:

$$\int_1^{\eta} \frac{v^2_{\max}(\eta)}{\eta} d\eta = \sum_{n=0}^{\infty} \sum_{m=0}^{\infty} \frac{16(-1)^{n+m}}{(2n+1)(2m+1)\pi^2} \int_1^{\eta} \frac{1}{\eta^3} \exp\left\{-\frac{(\beta_n^2 + \beta_m^2)}{2} (\eta^2 - 1)\right\} d\eta =$$

$$= \sum_{n=0}^{\infty} \sum_{m=0}^{\infty} \frac{16(-1)^{n+m}}{(2n+1)(2m+1)\pi^2} e^{\alpha} \int_1^{\eta} \frac{1}{\eta^3} e^{-\alpha\eta^2} d\eta$$

Then the integral becomes: $\int_1^{\eta} \frac{1}{\eta^3} e^{\alpha(\eta^2-1)} d\eta = e^{\alpha} \int_1^{\eta} \frac{1}{\eta^3} e^{-\alpha\eta^2} d\eta$

If $\eta^2 = \delta \Rightarrow d\delta = 2\eta d\eta \Rightarrow d\eta = \frac{d\delta}{2\eta}$ and $b = -\alpha$

$$\begin{aligned} \text{Then the integral becomes: } \int_1^{\eta} \frac{1}{\eta^3} e^{-\alpha\delta} d\eta &= \int_1^{\eta} \frac{1}{\eta^3} e^{b\eta^2} d\eta = \frac{1}{2} \int_1^{\eta} \frac{e^{b\delta}}{\eta^3} \frac{d\delta}{\eta} = \frac{1}{2} \int_1^{\eta} \frac{e^{\alpha\delta}}{\delta^2} d\delta \\ &= \frac{1}{2} \left[1 - \frac{e^{\alpha(1-\eta^2)}}{\eta^2} + (-\alpha)e^{\alpha} \left[\ln(\eta^2) + \sum_{k=1}^{\infty} \frac{(-\alpha)^k}{k \cdot k!} (\eta^{2k} - 1) \right] \right] \end{aligned}$$

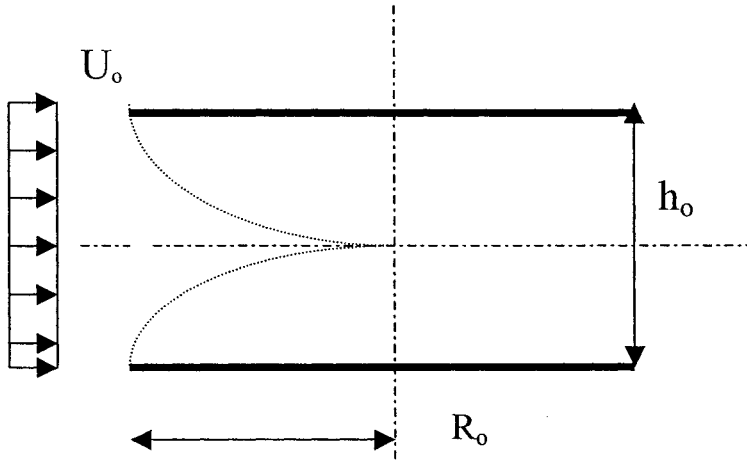
By following the same procedure as before, we get that :

$$\int_1^{\eta} \frac{v_{\max}^2(\eta)}{\eta} d\eta = \sum_{n=0}^{\infty} \sum_{m=0}^{\infty} \frac{16(-1)^{n+m}}{(2n+1)(2m+1)\pi^2} \frac{1}{2} \left[1 - \frac{e^{\alpha(\eta^2-1)}}{\eta^2} + (-\alpha)e^{\alpha} \left[\ln(\eta^2) + \sum_{k=1}^{\infty} \frac{(-\alpha)^k}{k \cdot k!} (\eta^{2k} - 1) \right] \right]$$

$$\Delta\Pi(\eta) = \frac{\lambda \sin(2\lambda)}{\lambda \sin(2\lambda) - 2\sin^2(\lambda)} + \frac{2s^2\eta^2}{(\eta^2-1)} \int_1^{\eta} \frac{v_{\max}^2(\eta)}{\eta} d\eta \Rightarrow$$

$$\Delta\Pi(\eta) = \frac{\lambda \sin(2\lambda)}{\lambda \sin(2\lambda) - 2\sin^2(\lambda)} + \frac{2s^2\eta^2}{(\eta^2-1)} \sum_{n=0}^{\infty} \sum_{m=0}^{\infty} \frac{16(-1)^{n+m}}{(2n+1)(2m+1)\pi^2} \frac{1}{2} \left\{ 1 - \frac{e^{\alpha(\eta^2-1)}}{\eta^2} + (-\alpha)e^{\alpha} \left[\ln(\eta^2) + \sum_{k=1}^{\infty} \frac{(-\alpha)^k}{k \cdot k!} (\eta^{2k} - 1) \right] \right\}$$

APPENDIX B – TWAITES METHOD



$$\frac{u}{U} = \frac{3}{2} \frac{y}{\delta} - \frac{1}{2} \frac{y^3}{\delta^3}$$

$$\begin{aligned} x &= r_o - r \\ \delta &= \delta(x) \\ U &= U(x) \\ h &= h(x) \\ r &= r(x) \end{aligned}$$

Continuity:

$$2\pi r_o U_o h_o = 2\pi r U (h_o - 2\delta^*)$$

$$\frac{r_o}{r} \frac{U_o}{U} h_o = h_o - 2\delta^* \Leftrightarrow h_o - 2\delta^* = \frac{r_o}{r} \frac{U_o}{U} h_o$$

$$2\delta^* = h_o - \frac{r_o}{r} \frac{U_o}{U} h_o$$

$$\delta^* = \frac{1}{2} \left(h_o - \frac{r_o}{r} \frac{U_o}{U} h_o \right) \quad (1)$$

Evaluation of δ^* and θ :

$$\begin{aligned} \delta^* &= \int_0^\delta \left(1 - \frac{u}{U} \right) dy = \int_0^\delta \left(1 - \frac{3}{2} \frac{y}{\delta} + \frac{1}{2} \frac{y^3}{\delta^3} \right) dy = \left[y - \frac{3}{2\delta} \frac{y^2}{2} + \frac{1}{2\delta^3} \frac{y^4}{4} \right]_0^\delta \\ &= \delta - \frac{3}{4\delta} \delta^2 + \frac{1}{8\delta^3} \delta^4 = \delta - \frac{3}{4} \delta + \frac{1}{8} \delta = \frac{8\delta - 6\delta + \delta}{8} = \frac{3}{8} \delta \end{aligned}$$

$$\delta^* = \frac{3}{8} \delta \quad \text{or} \quad \frac{\delta^*}{\delta} = \frac{3}{8}$$

$$\delta^* = \frac{1}{2} \left[h_o - \frac{r_o}{r} \frac{U_o}{U} h_o \right] \quad (2)$$

$$\delta = \frac{4}{3} \left[h_o - \frac{r_o}{r} \frac{U_o}{U} h_o \right] \quad (3)$$

Momentum Thickness θ :

$$\begin{aligned} \theta &= \int_0^\delta \frac{u}{U} \left(1 - \frac{u}{U} \right) dy = \int_0^\delta \left[\frac{u}{U} - \left(\frac{u}{U} \right)^2 \right] dy = \\ &\text{where } \left(\frac{u}{U} \right)^2 = \left[\frac{3}{2} \frac{y}{\delta} - \frac{1}{2} \frac{y^3}{\delta^3} \right]^2 = \frac{9}{4} \frac{y^2}{\delta^2} - \frac{1}{4} \frac{y^6}{\delta^6} + \frac{3}{2} \frac{y^4}{\delta^4} \\ &= \int_0^\delta \left[\frac{3}{2} \frac{y}{\delta} - \frac{1}{2} \frac{y^3}{\delta^3} - \frac{9}{4} \frac{y^2}{\delta^2} + \frac{1}{4} \frac{y^6}{\delta^6} - \frac{3}{2} \frac{y^4}{\delta^4} \right] dy = \\ &= \left[\frac{3}{2\delta} \frac{y^2}{2} - \frac{1}{2\delta^3} \frac{y^4}{4} - \frac{9}{4\delta^2} \frac{y^3}{3} + \frac{1}{4\delta^6} \frac{y^7}{7} - \frac{3}{2\delta^4} \frac{y^5}{5} \right]_0^\delta = -\frac{109}{280} \delta \\ \theta &= \frac{-109}{280} \delta \quad \rightarrow \quad \frac{\theta}{\delta} = \frac{-109}{280} \end{aligned}$$